



Title	Properties of Nucleon Resonances from Dynamical Model of Meson Production Reactions
Author(s)	鈴木, 信彦
Citation	大阪大学, 2009, 博士論文
Version Type	VoR
URL	https://hdl.handle.net/11094/473
rights	
Note	

The University of Osaka Institutional Knowledge Archive : OUKA

<https://ir.library.osaka-u.ac.jp/>

The University of Osaka

Properties of Nucleon Resonances from Dynamical Model of Meson Production Reactions

A dissertation presented

by

Nobuhiko Suzuki

to

Graduate School of Science, Department of Physics

in partial fulfillment of the requirements

for the degree of

Doctor of Philosophy

in the subject of

Physics

Osaka University

Toyonaka, Osaka

February, 2010

Abstract

Non-perturbative behavior of QCD appears as hadrons and their interactions. The mass, decay width and transition form factor of a nucleon resonance provide us basic and fundamental information to understand low energy QCD. Resonance parameters are extracted from amplitudes of πN scattering, meson-photoproduction and electroproduction. The purpose of this work is to extract resonance parameters such as mass, width and electromagnetic transition form factors from the the $\pi N - \pi N$ and $\gamma^* N - \pi N$ amplitudes by analytic continuation. Meson-production reactions are dominated by final states of πN , ηN and $\pi\pi N$ in the energy region above 1.3 GeV. We have developed the dynamical reaction model which includes πN , ηN and also unstable particle channels σN , ρN and $\pi\Delta$ coupled with $\pi\pi N$, but no analytic continuation method has been applied to such a dynamical model with unstable particle channels. In this work we develop an method of analytic continuation for the amplitude including those unstable channel. We apply the method for the scattering amplitude from the dynamical reaction model and extract mass, width and the electromagnetic $N - N^*$ transition form factors.

Contents

I. Introduction	6
II. Resonance and analytic structure of S-matrix	10
A. Scattering and resonance	10
B. Analytic structure of S-matrix	12
C. Analytic continuation method for dynamical models	20
1. Single-channel	20
2. Two-channel coupled system	23
3. Dynamical model with unstable particle channels	26
III. Extraction of resonance parameters	30
A. Pole expansion of scattering amplitudes	30
B. N-N* transition form factor	31
IV. Dynamical model of meson production reactions	33
A. Model Hamiltonian	33
B. Two body MB \rightarrow MB amplitude	36
C. MB \rightarrow $\pi\pi N$ amplitudes	42
D. Partial wave expansion of MB \rightarrow MB amplitudes	44
E. JLMS model of πN scattering	47
F. Pion electroproduction	58
V. Results and discussions	73
A. Analytic continuation and pole positions	73
B. Electromagnetic form factors	78
C. Two pole approximation for P_{11} amplitude	82
VI. Summary	83
Acknowledgments	85
A. Newton's method	86
1. Function of single variable	86

	5
2. Function of multi variables	86
3. Complex function	87
B. Pole expansion with two resonances	87
C. Lagrangians	88
D. Parameters from the fits	89
E. Integral path	95
References	97

I. INTRODUCTION

Spectrum of the excited baryons and their properties provide us important and fundamental information to understand strong interactions. A clear understanding of the spectrum and decay scheme of excited baryons will reveal the role of confinement and chiral symmetry in the non-perturbative QCD.

Most of information about the mass, width and transition form factor of baryon resonances have been extracted from partial wave analyses of πN scattering data[1] and sometimes the transition amplitudes to inelastic channels such as $\pi N \rightarrow \eta N$ [2] or $\pi N \rightarrow \pi\pi N$ [3, 4]. In addition there is information available from photo- and electroproduction of N^* resonances. Recently, such data with high precision have been accumulated at Jefferson Laboratory, MIT-Bates, LEGS of Brookhaven National Laboratory, MAMI of Mainz, ELSA of Bonn, GRAAL of Grenoble, and LEPS of SPring-8. These data on the electromagnetic production of π , η , K , ω , ϕ and 2π final states provide a opportunity to investigate the properties of excited baryons, as reviewed in Ref.[5].

Here, we briefly recall how resonances are defined in relation to S-matrix theory. By analytic continuation, a scattering amplitude can be defined on the complex energy plane. Its analytical structure is well studied[6–10] for the non-relativistic two-body scattering. For the single-channel case, the scattering amplitude is a single-valued function of momentum p on the complex momentum p-plane, but it is a double-valued function of energy E on the complex energy E-plane because of the quadratic relation $p = |2mE|^{1/2}e^{i\phi_E/2}$. Therefore the complex E-plane is composed of two Riemann sheets. The physical (p) sheet is defined by specifying the range of phase $0 \leq \phi_E \leq 2\pi$, and the unphysical (u) sheet by $2\pi \leq \phi_E \leq 4\pi$. As illustrated in Fig. 1, the shaded area with $\text{Im } p > 0$ of the upper part of Fig. 1(a) corresponds to the physical E -sheet shown in Fig. 1(b). Similarly, the unphysical E -sheet shown in Fig. 1(c) corresponds to the $\text{Im } p < 0$ area in the lower part of Fig. 1(a). On the physical sheet, the only possible singularities are on the real E-axis : the bound state poles (solid square in Fig. 1(b)) below the threshold energy E_{th} and the unitary cut from E_{th} to infinity. On the unphysical sheet, a pole (solid circle in Fig. 1(c)) on the lower half plane and $\text{Re } E_{pole} > E_{th}$ corresponds to a resonance. From unitarity and analyticity of S-matrix, each resonance pole has an accompanied pole, called conjugate pole, which exists on the upper half of the unphysical sheet. A resonance pole

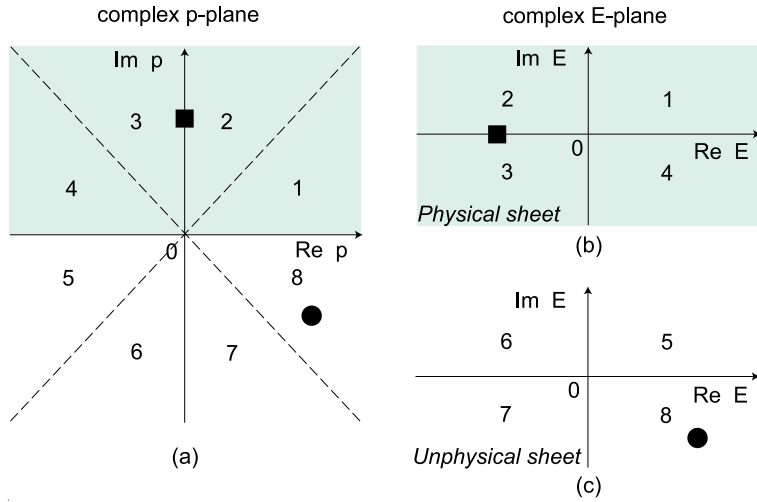


FIG. 1: The complex momentum p -plane ((a)) and its corresponding complex energy E -plane which has a physical sheet ((b)) and unphysical sheet ((c)). Their correspondence is indicated by the same number. Solid squares (circles) represent the bound state (resonance) poles.

is due to the mechanism : an unstable system is formed and decay subsequently during the collision. The mathematical details of this interpretation can be found in textbooks, such as in chapter 8 of Goldberger and Watson[11].

For multi-channel case, the analytic structure of the scattering amplitude becomes more complex [6–10]. In the inelastic region, a resonance is associated with a cluster of poles on different Riemann sheets. If one of these poles is located near the real axis and far enough from thresholds, it will be strongly dominant. We postpone the discussion on this until section II where a two-channel Breit-Wigner form of scattering amplitude will be used to give a pedagogical explanation.

Resonance parameters are extracted from partial wave amplitudes. The often used methods are based on the Breit-Wigner form[12], speed plot method of Hoehler[13, 14], and time delay method of Wigner[15, 16], which extract resonance parameters directly from partial wave amplitudes and need not a reaction model. Another method uses the dispersion relations, which was the basis of many analysis[17] of pion production data in the Δ region and is revived recently to also analyze η production reactions[18]. For investigating the data at higher energy, where the production of two pions and other mesons could occur, the isobar model was developed to extract parameters of higher

mass nucleon resonances [19]. K-matrix method and isobar parameterization is used to perform amplitude analysis of the data and determine resonance parameters by SAID[20] and MAID[21]. Multi-channel K-matrix method[2, 4, 22] and unitary coupled-channel isobar model[3, 23] have been also developed.

From the resonance parameters listed by the Particle Data Group[24], it is clear that only the low-lying N^* states are well established while there are large uncertainties in higher mass nucleon resonances. There are 13 “4-star” and 5 “3-star” N^* and Δ resonances below the mass of 2 GeV and another 6 “1- and 2-star” resonances at the same mass region. The Breit-Wigner parameters are most often quoted and are used in model-based studies of the baryons and associated reaction dynamics. The conventional parameters are the mass m_R , the width $\Gamma(E)$ at $E = m_R$, and the branching ratios. Following is one example of the problems with this conventional parametrization.

The Breit-Wigner mass, width and the pole position of $N^*(1440)P_{11}$, so-called Roper resonance, on Particle Listings by PDG[24] are extracted from several partial wave analyses of πN scattering data. The pole position can be related to the mass and width of the resonance by

$$m_R = \text{Re } E_{\text{pole}}, \quad \Gamma = -2\text{Im } E_{\text{pole}}, \quad (1)$$

which is the origin of the denominator in a Breit-Wigner parametrization of a resonance. By comparing the mass and width parameters to the position of the pole, one can see large discrepancies. The mass as extracted from the pole is estimated from 1350 to 1380 MeV, which lies typically about 80 MeV below m_R . Something similar can be seen by comparing the widths: here a ratio $-\Gamma/\text{Im } E_{\text{pole}} \sim 4$ is found instead of the expected value of 2. For an undistorted resonance, such as the $N^*(1520)D_{13}$, the mass and width from the Breit-Wigner parametrization and the pole position are essentially the same within a few MeV. This observation shows already that the Roper resonance is substantially influenced by strong meson-baryon non-resonant interactions and effects from nearby thresholds. Höhler suggested the use of the pole position as source of information on the mass and width of a resonance, since the pole has a well-defined meaning in S-matrix theory[25]. Around 1440 MeV, the VPI group found two poles in the P_{11} amplitude on different Riemann sheets[26]. Cutkosky et al. pointed out that the branch point for $\pi\Delta$ channel is located near the poles, so the poles belong to the same resonance[27]. Such meson-

baryon non-resonant interactions and effects from nearby threshold described above can be understood by a dynamical coupled channel model of meson production reactions that accounts for the off-shell scattering effects. It can therefore provide a much more direct way to interpret the resonance parameters.

The purpose of this work is to develop an analytic continuation method for meson production reactions and extract resonance parameters such as mass, width, electromagnetic transition form factors from the the $\pi N - \pi N$ and $\gamma^* N - \pi N$ amplitudes. We analyse πN and $\gamma^* N$ reactions up to 2 GeV to study N^* below 2 GeV. Above $\Delta(1232)P_{33}$ resonance, the dominant final states of those reactions are πN , ηN and $\pi\pi N$ states. The reaction model developed in Ref. [28–31] include πN and ηN and also unstable particle channels σN , ρN and $\pi\Delta$ to account for $\pi\pi N$. The model satisfies $\pi\pi N$ three body unitarity. To analytic continue to amplitude obtained form the above model, in addition to the stable particles channel such as πN and ηN the unstable particle channels, σN , ρN and $\pi\Delta$, which decay into $\pi\pi N$ channel. In the previous works on hyper nuclei[32] and $N - \Delta$ [33] system, unstable channels are treated as quasi two-body channel with complex mass and the decay of those states into three-body channel was only approximately included by introducing constant width. No analytic continuation method has been applied for extraction of N^* mass and form factor from the dynamical model in the previous works. In this work we develop an method to analytic continuation of the amplitude including those unstable channel. We then apply the method for the scattering amplitude obtained from the analysis of the πN of VPI and πN cross section and $\gamma^* N$ cross sections obtained from JLab. We extract mass, width and the electromagnetic $N - N^*$ transition form factors.

In section II, we review the analytic structure of S-matrix and resonance phenomena which appears as the pole of S-matrix on unphysical energy sheet and develop an analytic continuation method by using some dynamical models. In section III, we present the method to extract resonance parameters as the residue of poles on amplitudes which are $N-N^*$ transition form factors. In section IV, we present the model Hamiltonian of our formulation. It is derived from a set of Lagrangians by applying the unitary transformation method[34, 35]. The coupled-channel equations are derived from the model Hamiltonian and we explain the procedures for performing numerical calculations

within our formulation. Section V is devoted to showing the results from applying the developed analytic continuation method to extract the nucleon resonances in partial waves within our dynamical coupled channel model. Finally, a summary is given in section VI.

II. RESONANCE AND ANALYTIC STRUCTURE OF S-MATRIX

A. Scattering and resonance

Resonance phenomena are observed in scattering experiments of atomic, nuclear and particle physics. At first, we briefly review the pole structure of S-matrix within the frame work of non-relativistic quantum dynamics. Let us consider the elastic scattering of a spinless particle by a target and assume that the interaction is represented by a potential $V(r)$ which is spherically symmetric. Time-independent Schrödinger equation for S-wave scattering is written as

$$\left[-\frac{\nabla^2}{2m} + V(r) \right] \psi(\vec{r}) = E\psi(\vec{r}), \quad (2)$$

or

$$\left[-\frac{1}{2m} \frac{d^2}{dr^2} + V(r) \right] u_k(r) = \frac{k^2}{2m} u_k(r), \quad (3)$$

where the scattering wave function satisfies $\psi(\vec{r}) = u_k(r)/r$ and a total energy is $E = k^2/2m$. We assume that the potential $V(r)$ vanishes identically at all distances larger than some finite distance R ,

$$V(r) = 0 \quad \text{for} \quad r > R. \quad (4)$$

For $r > R$, the solution of Eq. (3) is given by

$$u_k(r) = A e^{ikr} + B e^{-ikr}, \quad (5)$$

which represents an outgoing and an incoming spherical wave. Here we define the S-matrix as

$$u_k(r) = N [S e^{ikr} - e^{-ikr}], \quad (6)$$

$$\frac{du_k}{dr} = N i k [S e^{ikr} + e^{-ikr}], \quad (7)$$

where N is a normalization factor. At $r = R$, it is clear that

$$\frac{1}{ik} \frac{du_k(R)}{dr} + u_k(R) = 2NSe^{ikR}, \quad (8)$$

$$\frac{1}{ik} \frac{du_k(R)}{dr} - u_k(R) = 2Ne^{-ikR}, \quad (9)$$

and we can easily obtain the expression of S-matrix,

$$S = e^{-2ikR} \frac{\frac{du_k(R)}{dr} + iku_k(R)}{\frac{du_k(R)}{dr} - iku_k(R)}. \quad (10)$$

Assuming there is a bound state at $E = -B < 0$ and no incoming wave, Eq. (3) can be solved as

$$u_B(r) = Ae^{ik_B r} \quad (11)$$

$$= Ae^{-\kappa_B r}, \quad (12)$$

with $k_B = i\kappa_B$ and $\kappa_B > 0$. Then the S-matrix for a bound state is given by

$$S = e^{-2ikR} \frac{-\kappa_B + ik}{-\kappa_B - ik}, \quad (13)$$

which has a pole at $k = i\kappa_B$ on the complex momentum plane. The pole that corresponds to a bound state exists on the imaginary axis of the complex momentum plane and the imaginary part of the pole position is positive.

Next, we assume some complex energy E_n and corresponding complex momentum k_n , which satisfies $E_n = k_n^2/2m$ and $\text{Re } k_n > 0$. The above Schrödinger equation for $r > R$ can be solved as

$$u_{k_n}(r) = Ae^{ik_n r} + Be^{-ik_n r}, \quad (14)$$

and

$$\frac{du_{k_n}}{dr} = ik[Ae^{ik_n r} - Be^{-ik_n r}]. \quad (15)$$

It is easily to derive the boundary condition at $r = R$,

$$u_{k_n}(R) - \frac{1}{ik_n} \frac{du_{k_n}(R)}{dr} = 2Be^{-ik_n R}. \quad (16)$$

If we assume that there is no incoming wave, that is $B = 0$, the resulting boundary condition is

$$u_{k_n}(R) - \frac{1}{ik_n} \frac{du_{k_n}(R)}{dr} = 0, \quad (17)$$

which means the S-matrix represented by Eq. (10) diverges at the pole on complex momentum plane, $k = k_n$. At this condition, the scattering wave function is

$$u_k(r) = Ae^{ik_R r - k_I r}, \quad (18)$$

where $k = k_R + ik_I$.

As a function of energy E , S is not single-valued, because it has different values for k and $-k$, which belong to the same energy. We must therefore replace the complex E plane by a Riemann surface of two sheets, linked by a branch point at the origin. It is convenient to think of each sheet as covering the E plane once, with a cut along the positive real axis. Then the first sheet corresponds to the half plane in k above the real axis. This is usually called physical sheet, which contains no poles except those belonging to real bound states[36]. On the other hand, the second sheet corresponds to the half plane in k below the real axis, which is called unphysical sheet and can contain resonance poles.

B. Analytic structure of S-matrix

To examine analytic properties of S-matrix, we consider a commonly used two-channel Breit-Wigner (BW) amplitude [6, 8, 37, 38] which can be naturally derived from the coupled channel equation. To make the contact with what we will discuss in this thesis, we will indicate here how this amplitude can be derived from a Hamiltonian formulation of meson-baryon reactions, such as that developed in Ref.[28].

It is sufficient to consider the simplest two-channel case with a non-relativistic two-particle Hamiltonian defined by

$$H = H_0 + V. \quad (19)$$

In the center of mass frame H_0 can be written as

$$H_0 = \sum_i |i\rangle [m_{i1} + m_{i2} + \frac{p^2}{2\mu_i}] \langle i|, \quad (20)$$

where m_{ik} is the mass of k -th particle in channel i , and $\mu_i = m_{i1}m_{i2}/(m_{i1} + m_{i2})$ is the reduced mass. In each partial-wave, the S-matrix is a 2×2 matrix and can be written

$$S = \frac{1 - i\pi\rho K}{1 + i\pi\rho K}, \quad (21)$$

where ρ is the density of state, and the K-matrix, which is also a 2×2 matrix, is defined by the following Lippmann-Schwinger equation

$$K(E) = V + V \frac{P}{E - H_0} K(E). \quad (22)$$

Here P means taking the principal-value of the integration over the propagator.

We now consider the on-shell matrix element of the S-matrix Eq. (21). If the on-shell momentum is denoted as p_i for channel i , we then have

$$\langle i | 1 \pm i\pi\rho K | j \rangle = \delta_{i,j} \pm i\pi\rho_i K_{i,j}, \quad (23)$$

where $\rho_i = p_i\mu_i$. The S-matrix element of the $1 \rightarrow 1$ elastic scattering is then of the following explicit form

$$S_{11} = \frac{(1 - i\pi\rho_1 K_{11})(1 + i\pi\rho_2 K_{22}) - \pi^2\rho_1\rho_2 K_{12}K_{21}}{(1 + i\pi\rho_1 K_{11})(1 + i\pi\rho_2 K_{22}) - \pi^2\rho_1\rho_2 K_{11}K_{22}}. \quad (24)$$

If we assume that at energies near the resonance energy the K-matrix can be approximated as

$$K_{ij} \sim \frac{g_i g_j}{E - M}, \quad (25)$$

where M is a mass parameter which is a real number, Eq. (24) can then be written as

$$S_{11} = \frac{E - M - ip_1\gamma_1 + ip_2\gamma_2}{E - M + ip_1\gamma_1 + ip_2\gamma_2}. \quad (26)$$

Here we have defined $\gamma_i = \pi g_i^2 \mu_i > 0$. If we further assume that γ_i is independent of scattering energy, Eq. (26) is the commonly used two-channel Breit-Wigner formula[37, 38, 40]. Here, we will follow these earlier works and treat γ_1 and γ_2 as energy independent parameters of the model.

Since the scattering T-matrix is related to the S-matrix by

$$S_{11}(E) = 1 + 2iT_{11}(E), \quad (27)$$

Eq.(26) leads to

$$\begin{aligned} T(E) &= T_{11}(E) \\ &= \frac{-\gamma_1 p_1}{E - M + i\gamma_1 p_1 + i\gamma_2 p_2}. \end{aligned} \quad (28)$$

From now we use the notation $T(E)$ for the $1 \rightarrow 1$ amplitude $T_{11}(E)$.

Within the two-channels Breit-Wigner model specified above, we will examine the analytic properties of the S-matrix on the complex energy E-plane. This will also allow us to explain clearly some terminologies which are commonly seen but often not explicitly explained in the literatures on resonance extractions.

The on-shell momenta p_i for channel i is defined by

$$E_i = \frac{p_i^2}{2\mu_i}, \quad (29)$$

where

$$E_i = E - (m_{i1} + m_{i2}). \quad (30)$$

We can define the threshold variable Δ between two channels by

$$E_1 = \frac{p_2^2}{2\mu_2} + \frac{\Delta^2}{2\mu_1}, \quad (31)$$

where

$$\frac{\Delta^2}{2\mu_1} = m_{21} + m_{22} - m_{11} - m_{12} \quad (32)$$

is the threshold energy of the second channel.

The momenta at poles of the S-matrix Eq. (26) can be determined by solving

$$E - M + ip_1\gamma_1 + ip_2\gamma_2 = 0. \quad (33)$$

By using Eqs. (29)-(32), the above equation can be written as

$$p_1^4 + ap_1^3 + bp_1^2 + cp_1 + d = 0, \quad (34)$$

where

$$a = i4\mu_1\gamma_1, \quad (35)$$

$$b = 4\mu_1(\mu_2\gamma_2^2 - M - \mu_1\gamma_1^2), \quad (36)$$

$$c = -8i\mu_1^2M\gamma_1, \quad (37)$$

$$d = 4(\mu_1^2M^2 - \mu_1\mu_2\gamma_2^2\Delta^2). \quad (38)$$

Eq. (34) means that the Breit-Wigner amplitude Eq. (26) has four poles. Each pole is specified by two on-shell momenta $P_\alpha = (p_{1\alpha}, p_{2\alpha})$ with $\alpha = 1, 2, 3, 4$. The analytic

properties of the S -matrix Eq. (26) depends on how these poles are located on the complex energy E -plane. The energy plane for each channel has two Riemann sheets because of the quadratic relation Eq. (29) between the momentum p_i and energy E_i ; namely $p_i = \sqrt{2\mu_i|E_i|}e^{i\phi_i/2}$ for $i = 1, 2$. For each channel, the physical (p) sheet is defined by specifying the range of phase $0 \leq \phi_i \leq 2\pi$, and the un-physical (u) sheet by $2\pi \leq \phi_i \leq 4\pi$. The correspondence between the momentum p_i -plane and the energy E_i -plane is similar to that illustrated in Fig. 1. For the considered two-channel case, we thus have four energy sheets specified by the signs of $\text{Im } p_1$ and $\text{Im } p_2$: pp , up , uu , and pu , as shown in Fig. 2. Thus each of four poles $P_\alpha = (p_{1\alpha}, p_{2\alpha})$ can be on one of these E -sheets.

To be more specific, we now consider the case which is most relevant to our study of nucleon resonances. That is the $\text{Re } E_1 > 0$ and $\text{Re } E_2 > 0$ case that the poles are all above the thresholds of both channels. From Eq. (33), we immediately notice that if (p_{1a}, p_{2a}) with $E = E_a$ is one of the solutions, $(-p_{1a}^*, -p_{2a}^*)$ with $E = E_a^*$ is also a solution. Therefore the four poles determined by Eq. (34) can be grouped into two pairs. In the following discussions, they are denoted as (E_a, E_a^*) and (E_b, E_b^*) . Without losing generality, one can assume that one of the poles is in the range of $(\text{Re } p_1 > 0, \text{Re } p_2 > 0)$ and the other in the range of $(\text{Re } p_1 < 0, \text{Re } p_2 < 0)$. If the first pole (p_{1a}, p_{2a}) is in the region where $(\text{Re } p_{1a} > 0, \text{Re } p_{2a} > 0)$ and $(\text{Im } p_{1a} < 0, \text{Im } p_{2a} < 0)$, it is a pole, denoted as E_R , on the uu -sheet of Fig. 2. This pole is usually called the resonance pole and is closer than other poles on up or pu -sheets to the physical pp -sheet, as will be explained later. In the Hamiltonian formulation considered in this work and the well developed collision theory, a resonance pole can be mathematically derived[11] from the mechanism that an unstable system is formed and decay subsequently during the collision. The resonance pole E_R has an accompanied pole E_R^* at $(-p_{1a}^*, -p_{2a}^*)$ which is also on the uu -sheet as shown in Fig. 2. E_R^* is called the 'conjugate pole' of E_R .

The second pole at (p_{1b}, p_{2b}) with $\text{Im } p_{1b} < 0$ and $\text{Im } p_{2b} > 0$ ($\text{Im } p_{1b} > 0$ and $\text{Im } p_{2b} < 0$) may be on the up -sheet (pu -sheet), depending on the parameters γ_1 and γ_2 . This pole is called the shadow pole[39]. A shadow pole on up -sheet and its conjugate pole are E_S and E_S^* in Fig. 2.

We now note that in this simple BW model, the zeros of the S -matrix Eq. (26), where

$S_{11}(E) = 0$, is defined by its numerator

$$E - M - ip_1\gamma_1 + ip_2\gamma_2 = 0. \quad (39)$$

The above equation can be cast into the form of Eq. (33) by simply replacing p_1 by $-p_1$. Thus solutions of Eq. (39), called the zeros of S-matrix, can be readily obtained from the solutions (p_{1a}, p_{2a}) and (p_{1b}, p_{2b}) of Eq. (33). They are $(-p_{1\alpha}, p_{2\alpha})$ with E_α and $(p_{1\alpha}^*, -p_{2\alpha}^*)$ with E_α^* for $\alpha = a, b$. The zero at $(-p_{1b}, p_{2b})$ is on the *pp*-sheet, denoted as E_{ZS} and E_{ZS}^* in Fig. 2. Similarly, the zero at $(-p_{1a}, p_{2a})$ is on the *pu*-sheet, shown as E_{ZR} together with its conjugate E_{ZR}^* in Fig. 2. Note that Fig. 2 is for the case that the parameters γ_1 and γ_2 are chosen such that the shadow poles E_S and its conjugate E_S^* are on the *up*-sheet. For other possible γ_1 and γ_2 , the pole positions could be different from what are shown in Fig. 2, but their close relations, as discussed above, are the same.

From the above analysis, it is clear that the poles and zeros of the S-matrix are closely related. Their locations on the 4 Riemann sheets can be conveniently displayed on one complex plane by introducing a variable t [36]

$$p_1 = \Delta \frac{1+t^2}{1-t^2}, \quad (40)$$

$$p_2 = 2\Delta \sqrt{\frac{\mu_2}{\mu_1}} \frac{t}{1-t^2}. \quad (41)$$

Hence each point in the t -plane corresponds to a set of (p_1, p_2) . In Fig. 3, the resonance position E_R and shadow E_S poles and their conjugate poles and zeros of S-matrix $E_{ZS}, E_{ZR}, E_{ZS}^*, E_{ZR}^*$ are shown on t -plane. The physical S-matrix at real energies, which determine the observables, are on the bold lines. The zero energy and the threshold of the second channel correspond to $t = i$ and $t = 0$, respectively. One can see that the resonance pole E_R is closer than the shadow pole E_S to the bold lines (S-matrix) and hence can have the largest effect on the observables. Consequently, most of the rapid energy dependence of observables are attributed to the resonance poles, not the shadow poles or the other poles shown in Fig.3. On the other hand, the zero E_{ZS}^* of the S-matrix is also close to the bold lines. As seen in the derivations given above, this zero E_{ZS}^* is closely related to shadow pole E_S . Thus the shadow poles can also be related to the observables. Of course, which pole is most important in determining the rapid energy dependence of observables also depends on the residues of the T-matrix at the pole positions.

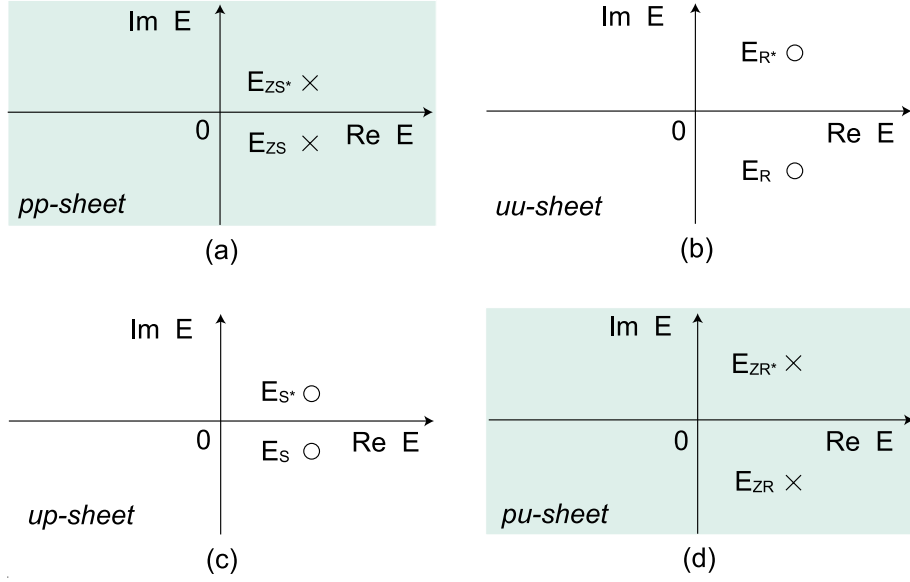


FIG. 2: Poles and zeros of the simplified two-channel Breit-Wigner form ($\mu_1 = \mu_2$ and $\Delta = 0$) of S -matrix on the complex E -plane which has pp , uu , up and pu sheets. The open circles on the uu -sheet ((b)) are the resonance pole E_R and its conjugate pole E_R^* . The open circles on the up -sheet ((c)) are the shadow pole E_S and its conjugate pole E_S^* . The crossed on the pp -sheet ((a)) are the zero E_{zs} and its conjugate E_{zs}^* which are at the same energies of the shadow poles E_S and E_S^* . The crossed on the pu -sheet ((d)) are the zero E_{zr} and its conjugate E_{zr}^* which are at the same energies of the resonance poles E_R and E_R^* .

Next, we will use a further simplified BW form to explain more clearly the close relations between the poles and zeros of the S -matrix. In particular we will see explicitly that the shadow pole E_S in Fig. 2, which is not on the same Riemann sheet as E_R , can be located by the zeros of the S -matrix.

For simplicity, we assume that the threshold energies of the two channels are the same and hence $\mu \equiv \mu_1 = \mu_2$ and $\Delta = 0$. Therefore we have simple relations between energy and momenta : $E = p_1^2/2\mu = p_2^2/2\mu$ and $p \equiv p_1 = \pm p_2$. The four Riemann sheets are classified by the sign of the imaginary part of the momentum; namely, physical (unphysical) sheet is assigned by $\text{Im } p > 0$ ($\text{Im } p < 0$). With the simplification $p \equiv p_1 = \pm p_2$, we obviously have $p_1 = p_2 = p$ on the pp and uu -sheets, and $p_1 = -p_2 = p$ on up and pu -sheets.

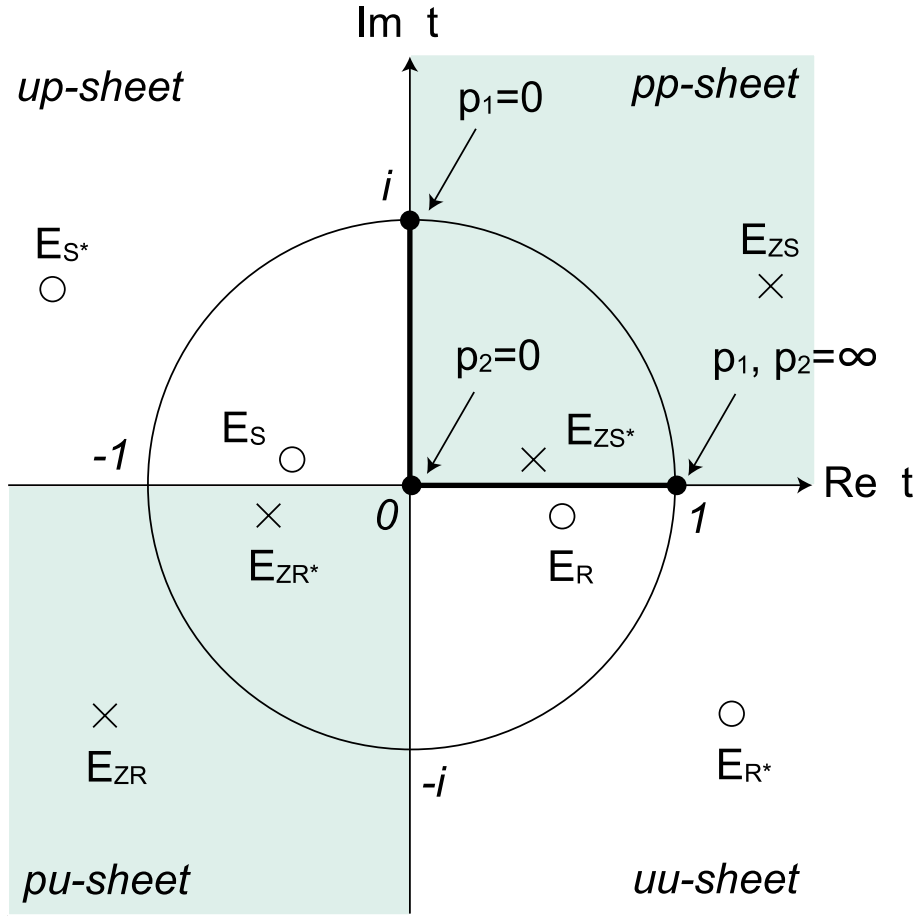


FIG. 3: The poles and zeros of S-matrix shown in Fig.2 are displayed on the complex t -plane defined by Eqs. (40) and (41).

Let us start with the case of $p_1 = p_2 = p$ for the pp -sheet or uu -sheet. The S-matrix element Eq. (26) of the first channel can be written as

$$S_{11}(E) = \frac{E - M - i(\gamma_1 - \gamma_2)p}{E - M + i(\gamma_1 + \gamma_2)p}. \quad (42)$$

It can be cast into the following more transparent form

$$S_{11}(E) = \frac{(p + p_S)(p - p_S^*)}{(p - p_R)(p + p_R^*)}, \quad (43)$$

with

$$p_R = \sqrt{2\mu M - (\mu\gamma_+)^2} - i\mu\gamma_+, \quad (44)$$

$$p_S = \sqrt{2\mu M - (\mu\gamma_-)^2} - i\mu\gamma_-, \quad (45)$$

where

$$\gamma_{\pm} = \gamma_1 \pm \gamma_2. \quad (46)$$

Remembering that we consider $\gamma_1 > 0$ and $\gamma_2 > 0$. To make use of Fig.2 in the following discussion, we consider the case that $\gamma_1 > \gamma_2$ and hence $\gamma_{\pm} > 0$ and both p_R and p_S defined in Eqs. (44)-(45) are associated with the unphysical u -sheet. For the case of $\gamma_- < 0$, p_S is associated with the physical p -sheet and the following presentation can be easily modified to account for this case.

Clearly, Eq. (43) means that the S -matrix has a pole at $p_1 = p_2 = p = p_R$ on the uu -sheet with a resonance energy

$$E_R = \frac{p_R^2}{2\mu} = M - \mu\gamma_+^2 - i\gamma_+ \sqrt{\mu(2M - \mu\gamma_+^2)}. \quad (47)$$

Its conjugate pole E_R^* is at $p_1 = p_2 = p = -p_R^*$. The positions of E_R and E_R^* are shown in the upper right side of Fig.2. Eq. (43) also indicates that the zero of S -matrix is at $p_1 = p_2 = -p_S$ which is on the pp -sheet because of $\text{Im}(-p_S) > 0$. The energy of this zero of S -matrix is

$$E_{ZS} = \frac{p_S^2}{2\mu} = M - \mu\gamma_-^2 - i\gamma_- \sqrt{\mu(2M - \mu\gamma_-^2)}. \quad (48)$$

Its conjugate E_{ZS}^* is at $p_1 = p_2 = p_S^*$. The positions of E_{ZS} and E_{ZS}^* are on the pp -sheet, as shown in the upper left side of Fig.2.

We next consider the $p_1 = -p_2 = p$ case that the poles and zeros of the S -matrix are on the up or pu -sheets. The S -matrix Eq. (26) for this case then takes the following form

$$S_{11}(E) = \frac{E - M - i(\gamma_1 + \gamma_2)p}{E - M + i(\gamma_1 - \gamma_2)p}. \quad (49)$$

By comparing Eq. (42) and Eq. (49) and using the variables p_R and p_S defined by Eqs. (44) and (45), Eq. (49) can be written as

$$S_{11}(E) = \frac{(p + p_R)(p - p_R^*)}{(p - p_S)(p + p_S^*)}. \quad (50)$$

The above equation indicates that for the considered $\gamma_- > 0$, the S -matrix has a shadow pole at $p_1 = -p_2 = p = p_S$ on the up -sheet. Thus its position $E_S = p_S^2/(2\mu)$ is identical to E_{ZS} of the zero of the S -matrix on the pp -sheet; namely

$$\begin{aligned} E_S &= E_{ZS} \\ &= \frac{p_S^2}{2\mu} = M - \mu\gamma_-^2 - i\gamma_- \sqrt{\mu(2M - \mu\gamma_-^2)}. \end{aligned} \quad (51)$$

This means that the shadow pole E_S on the *up*-sheet can be found from searching for the zero E_{ZS} of S-matrix on the *pp*-sheet.

Eq. (50) also gives a zero of S-matrix at $p_1 = -p_2 = p = -p_R$ on *pu*-plane because $\text{Im}(-p_R) > 0$. Its energy E_{ZR} is also identical to E_R defined above

$$\begin{aligned} E_{ZR} &= E_R \\ &= \frac{p_R^2}{2\mu} = M - \mu\gamma_+^2 - i\gamma_+ \sqrt{\mu(2M - \mu\gamma_+^2)}. \end{aligned} \quad (52)$$

The positions of E_S and E_{ZR} and their conjugates E_S^* and E_{ZR}^* are also in the lower parts of Fig.2.

From the above analysis for the $\gamma_- > 0$ case, we see that the energies of the resonance poles may be obtained by studying the poles of the S-matrix on the *uu*-sheet and those of the shadow poles may be obtained from the zeros of the S-matrix on the *pp*-sheet. The analysis for the $\gamma_- < 0$ case is similar. Here we only mention that when $\gamma_- > 0$ is changed to $\gamma_- < 0$, the shadow poles E_S and E_S^* on the *up*-sheet move to the *pu*-sheet and zeros E_{ZS} and E_{ZS}^* will be on the *uu*-sheet.

C. Analytic continuation method for dynamical models

With the analysis presented in the previous subsection, it is clear that the empirical partial-wave amplitudes determined from experimental data can not be blindly used to extract resonance parameters. To make progress, one needs to construct a reaction model to fit the data and then extract the resonance parameters by analytic continuation within the model. Our task in this subsection is to develop numerical methods for finding the resonance poles from dynamical coupled-channel models which do not have analytical forms of their solutions. We will first consider the simplest single-channel case, then two-channel coupled case and finally unstable channels coupled case.

1. Single-channel

To be specific, we consider the two-particle reactions defined by the following well known isobar Hamiltonian in the center of mass frame

$$H = H_0 + H', \quad (53)$$

with

$$H_0 = [E_1(\vec{p}) + E_2(-\vec{p})] + |N_0\rangle M_0 \langle N_0| , \quad (54)$$

$$H' = |g\rangle \langle g| , \quad (55)$$

where M_0 is the mass parameter of a bare particle N_0 which can decay into two particle states through the vertex interaction g in H' , and $E_i(p) = [m_i^2 + p^2]^{1/2}$ is the energy of the i -th particle. The scattering operator is defined by

$$t(E) = H' + H' \frac{1}{E - H_0 - H'} H' , \quad (56)$$

which leads to the following Lippmann-Schwinger equation for the scattering amplitudes in each partial-wave

$$t(p', p; E) = v(p', p; E) + \int_{C_0} dq q^2 \frac{v(p', q; E) t(q, p; E)}{E - E_1(q) - E_2(q)} , \quad (57)$$

where the integration path C_0 will be specified later. The interaction in Eq. (57) is

$$v(p', p; E) = \frac{g(p')g(p)}{E - M_0} . \quad (58)$$

Eqs. (57)-(58) leads to the following well known solution

$$t(p', p; E) = \frac{g(p')g(p)}{E - M_0 - \Sigma(E)} , \quad (59)$$

with

$$\Sigma(E) = \int_{C_0} dp p^2 \frac{g^2(p)}{E - E_1(p) - E_2(p)} . \quad (60)$$

The resonance poles can be found from $t(E) = t(p_0, p_0; E)$ on the unphysical Riemann sheet defined by $\text{Im } p_0 < 0$ with p_0 denoting the on-shell momentum

$$E = \sqrt{m_1^2 + p_0^2} + \sqrt{m_2^2 + p_0^2} . \quad (61)$$

Obviously p_0 is also the pole position of the propagator in Eq. (57) or Eq. (60).

The physical scattering amplitude at a positive energy E can be obtained from Eq. (57) or Eq. (59) by setting $E \rightarrow E + i\epsilon$ with a positive $\epsilon \rightarrow 0$ and choosing the integration contour C_0 to be along the real-axis of p with $0 \leq p \leq \infty$. From Eq. (57) it is clear that $t(E)$ has a discontinuity on the positive real E

$$\begin{aligned} \text{Dis}(t(E)) &= t(E + i\epsilon) - t(E - i\epsilon) \\ &= 2\pi i \rho(p_0) v(p_0, p_0) t(E) , \end{aligned} \quad (62)$$

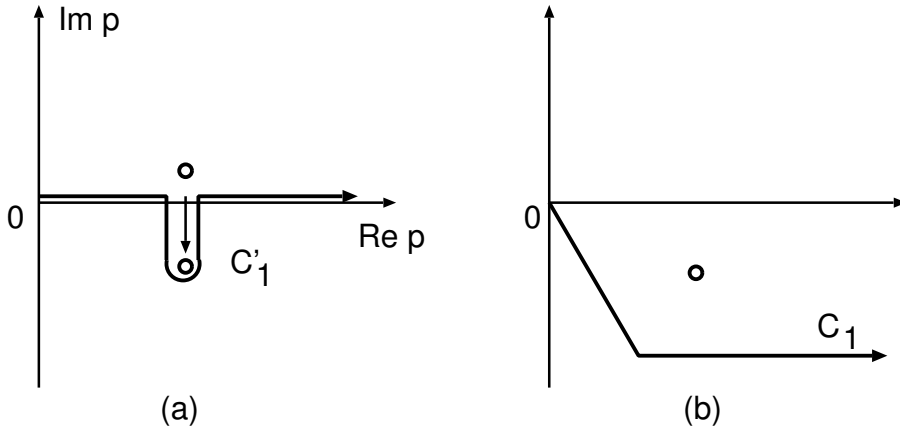


FIG. 4: The shift of the singularity (open circle) of the propagator of the two-particle scattering equation Eq. (57) as energy E moves from physical sheet to unphysical sheet. C'_1 in (a) or C_1 in (b) is the integration path for calculating the scattering amplitude with E on the unphysical plane.

where $\rho(p_0) = p_0 E_1(p_0) E_2(p_0)/E$. Thus the t -matrix has a cut running along the real positive E . To find resonance poles, we need to find the solution of Eq. (57) on the un-physical sheet with $\text{Im } p \leq 0$ on which the pole p_0 of the propagator moves into the lower p -plane, as shown in (a) of Fig.4. From Eq. (62), it is clear that the solution of Eq. (57), with the contour C_0 chosen to be on the real-axis $0 \leq p \leq \infty$, will encounter the discontinuity and is not the solution on the unphysical sheet where we want to search for the resonance poles. It is well-known[40–43] that this difficulty can be overcame by deforming the integration path to the contour C'_1 shown in (a) of Fig.4. By this the pole will not cross the cut and the integral is analytically continued from real positive E to the lower half of the unphysical E -sheet with $\text{Im } p_0 \leq 0$. Obviously, the same solution can be obtained by choosing any contour which is below the pole position p_0 , such as the contour C_1 of (b) of Fig.4.

With the solution of the form of Eq. (59), the numerical procedure of finding resonance poles is to solve

$$E - M_0 - \Sigma(E) = 0. \quad (63)$$

with

$$\Sigma(E) = \int_{C_{1'}} dp p^2 \frac{g^2(p)}{E - E_1(p) - E_2(p)} \quad (64)$$

$$= \int_{C_1} dp p^2 \frac{g^2(p)}{E - E_1(p) - E_2(p)}, \quad (65)$$

for E on the unphysical Riemann sheet defined by $\text{Im } p_0 \leq 0$. To test this numerical procedure, let us consider the case that $\Sigma(E)$ defined by Eq. (60) can be calculated analytically. Such an analytic form can be obtained by taking the non-relativistic kinematics $E_1(p) + E_2(p) = m_1 + m_2 + p^2/(2\mu)$ with $\mu = m_1 m_2 / (m_1 + m_2)$ and a monopole form for the vertex function

$$g(p) = \frac{\lambda}{1 + p^2/\beta^2}, \quad (66)$$

where β is a cut-off parameter. The integration in $\Sigma(E)$ of Eq. (60) can then be done exactly to give the following simple form

$$\Sigma(E) = \frac{\pi \mu \beta^3 \lambda^2}{2(p_0 + i\beta)^2}, \quad (67)$$

where p_0 is defined by $E = m_1 + m_2 + p_0^2/(2\mu)$. If the imaginary part of p_0 is positive (negative), it means that we choose the poles on physical (unphysical) sheet. Only the pole with $\text{Im } p_0 \leq 0$ on the unphysical sheet is called resonance.

2. Two-channel coupled system

The formula for two-channels, one-resonance case can be easily obtained by extending the equations in the case of one-channel. We introduce channel label $i = 1, 2$ and thus have

$$t_{ij}(p', p; E) = v_{ij}(p', p; E) + \sum_k \int_{C_0} dq q^2 \frac{v_{ik}(p', q) t_{kj}(q, p; E)}{E - E_{k1}(q) - E_{k2}(q)}, \quad (68)$$

where $E_{kn}(p) = [m_{kn}^2 + p^2]^{1/2}$ with m_{kn} denoting the mass of n -th particle in channel k , and

$$v_{ij}(p', p; E) = g_i(p') \frac{1}{E - M_0} g_j(p). \quad (69)$$

Eqs. (68)-(69) leads to

$$t_{ij}(p', p; E) = \frac{g_i(p') g_j(p)}{E - M_0 - \Sigma_1(E) - \Sigma_2(E)}, \quad (70)$$

with

$$\Sigma_k(E) = \int_{C_0} dp p^2 \frac{g_k^2(p)}{E - E_{k1}(p) - E_{k2}(p)}. \quad (71)$$

For the physical scattering amplitude at a positive energy E , Eq. (68) is solved by setting $E \rightarrow E + i\epsilon$ with a positive $\epsilon \rightarrow 0$ and choosing C_0 along the real axis $0 \leq p \leq \infty$.

With Eq. (70), the poles of the scattering amplitudes are defined by

$$E - M_0 - \Sigma_1(E) - \Sigma_2(E) = 0. \quad (72)$$

The poles from solving the above equation can be on one of the four Riemann sheets, pp , up , uu , and pu . The numerical procedure for finding the resonance poles on uu -sheet is to solve Eq. (72) for $E = E_{11}(p_{01}) + E_{12}(p_{01}) = E_{21}(p_{02}) + E_{22}(p_{02})$ with $\text{Im } p_{01} \leq 0$ and $\text{Im } p_{02} \leq 0$. The integration path C_0 is changed to C_1 shown in (b) of Fig.4 to calculate both self-energies $\Sigma_1(E)$ and $\Sigma_2(E)$ of Eq. (71). Of course the contour C_1 for the integration over the momentum for i -th channel must be below the pole p_{0i} defined by $E - E_{i1}(p_{0i}) - E_{i2}(p_{0i}) = 0$. Here we note that for finding the poles on pu -sheet (up -sheet), the contour C_0 is replaced by C_1 only for $\Sigma_2(E)$ ($\Sigma_1(E)$).

To test the pole trajectory, let us consider again the non-relativistic kinematics $E_{i1}(p) + E_{i2}(p) = m_{i1} + m_{i2} + p^2/(2\mu_i)$ with $\mu_i = m_{i1}m_{i2}/(m_{i1} + m_{i2})$. This will allow us to find the exact solutions by choosing the monopole form factor

$$g_i(p) = \frac{\lambda_i}{1 + p^2/\beta_i^2}. \quad (73)$$

We then have

$$\Sigma_i(E) = \frac{\pi\mu_i\beta_i^3\lambda_i^2}{2(p_i + i\beta_i)^2}. \quad (74)$$

With Eq. (74), the poles defined by Eq. (72) can be found by solving algebraic equations. For numerical calculations, we consider a case similar to πN scattering in S_{11} partial wave: (1)channel-1 is πN with $m_{11} = m_\pi = 139.6$ MeV, $m_{12} = m_N = 938.5$ MeV, and $\beta_1 = 800$ MeV, (2)channel-2 is ηN with $m_{21} = m_\eta = 547.45$ MeV, $m_{22} = m_N = 938.5$ MeV, and $\beta_2 = 800$ MeV, (3) bare mass $M_0 = m_\pi + m_N + 600$ MeV. The results are shown in Fig.5. The dash-dotted (solid) curves are the calculated poles on uu -sheet (up -sheet) with the coupling constants $\lambda_1 = 0.02$ for $N_0 \rightarrow \pi N$ and a range of $\lambda_2 = 0 - 0.02$

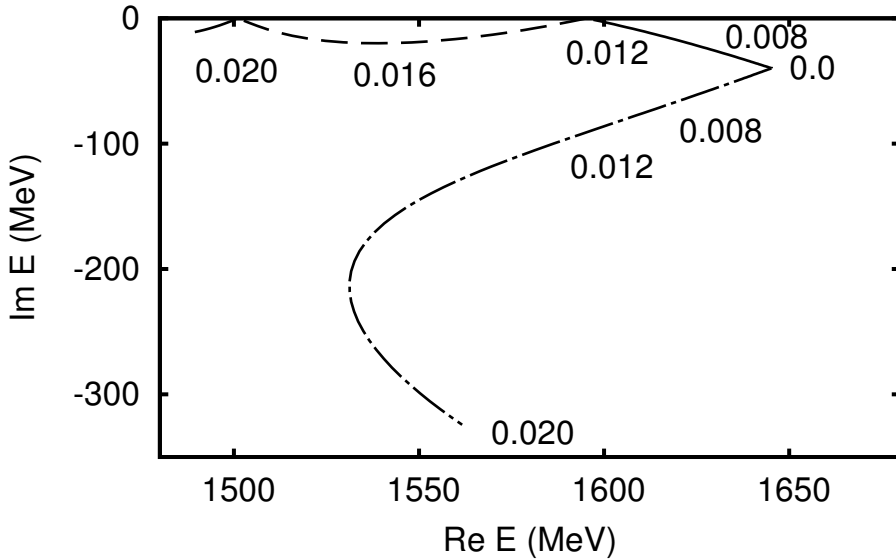


FIG. 5: λ_2 dependence of the pole positions on the *uu*-sheet (dash-dotted curve), *up*-sheet (solid curve) and *pu*-sheet (dashed curve) of the two-channels, one-resonance model.

for $N_0 \rightarrow \eta N$. We see that when λ_2 is 0, which is the single-channel case, the *uu*-pole and the *up*-pole are on the same position. They then split as λ_2 increases.

We next evaluate Eq. (71) for E on the *uu*-sheet, *up*-sheet or *pu*-sheet by appropriately choosing the path C_0 , as described above. The poles are found when the calculated $\Sigma_1(E)$ and $\Sigma_2(E)$ satisfy Eq. (72). We find that the poles obtained by this numerical procedure reproduce accurately the dash-dotted(*uu*-sheet), solid(*up*-sheet) and dashed(*pu*-sheet) curve in Fig.5 and hence are omitted there. Thus this analytic continuation method can be used in practice to find the resonance poles.

In Fig.5, the poles on the *uu*-sheet are represented by dash-dotted curve. The poles on the *up*-sheet and *pu*-sheet are represented by the solid curve and the dashed curve respectively. One can show[11] that the poles on *uu*-sheet are due to the process that an unstable system is created and then decays during the collision and are called the resonance poles. The physical interpretations of the poles on *pu* and *up*-sheets remain to be developed.

It is interesting to point out here that the two-channel Breit-Wigner form analyzed

in detail in the previous subsection can be derived from the two-channels, one-resonance model if the non-relativistic kinematics is used. To see this, we first write the non-relativistic relation between the S-matrix and the T-matrix

$$S_{ij}(E) = \delta_{ij} + 2iT_{ij}(E), \quad (75)$$

$$T_{ij}(E) = -\pi\sqrt{\mu_i p_i \mu_j p_j} t_{ij}(p_i, p_j; E), \quad (76)$$

where p_i is the on-shell momentum in channel i

$$p_i = \sqrt{2\mu_i(E - m_{i1} - m_{i2})}. \quad (77)$$

With the above and the analytic form Eq. (74) for $\Sigma_i(E)$, we can write the $1 \rightarrow 1$ elastic scattering amplitude of Eq. (76) as

$$T_{11}(p_1, p_1, E) = \frac{-p_1\gamma_1(p_1)}{E - M(E) + ip_1\gamma_1(p_1) + ip_2\gamma_2(p_2)}, \quad (78)$$

where $\gamma_i(p_i) = \pi\mu_i g_i^2(p_i) > 0$ and

$$M(E) = M^0 + \sum_k P \int p^2 dp \frac{g_k^2(p)}{E - m_{k1} - m_{k2} - \frac{p^2}{2\mu_k}} \quad (79)$$

where P means taking the principal-value integration. By using Eq. (75), we then have the $1 \rightarrow 1$ elastic part of the S-matrix

$$S_{11} = \frac{E - M(E) - ip_1\gamma_1(p_1) + ip_2\gamma_2(p_2)}{E - M(E) + ip_1\gamma_1(p_1) + ip_2\gamma_2(p_2)}. \quad (80)$$

If the E-dependence of $M(E)$ and $\gamma_i(p_i)$ are further neglected, Eqs. (78) and (80) are identical to what are usually called the two-channel Breit-Wigner resonant amplitude discussed in the previous subsection.

3. Dynamical model with unstable particle channels

For meson-baryon reactions, the nucleon resonances can decay into some unstable particle channels such as the $\pi\Delta$, ρN , σN considered in the model of Ref.[28]. Here we discuss the analytic continuation method to find resonance poles within such a reaction model.

It is sufficient to consider the one-channel and one resonance case. The scattering formula is then identical to that presented above. The only difference is that one of the

particles in the open channel can further decay into a two particle state. To be specific, let us consider the $\pi\Delta$ channel. Within the same Hamiltonian formulation[28], the scattering amplitude can then be written as

$$t(p', p, E) = \frac{g_{N^*, \pi\Delta}(p') g_{N^*, \pi\Delta}(p)}{E - M_0 - \Sigma_{\pi\Delta}(E)} \quad (81)$$

with

$$\Sigma_{\pi\Delta}(E) = \int_{C_2} p^2 dp \frac{g_{N^*, \pi\Delta}^2(p)}{E - E_\pi(p) - E_\Delta(p) - \Sigma_\Delta(p, E)} \quad (82)$$

where

$$\Sigma_\Delta(p, E) = \int_{C_3} q^2 dq \frac{g_{\Delta, \pi N}^2(q)}{E - E_\pi(p) - [(E_\pi(q) + E_N(q))^2 + p^2]^{1/2}}. \quad (83)$$

To obtain the $\pi\Delta$ self energy for complex E , the analytic structure of the integrand of Eq. (82) should be examined first. The discontinuity of the $\pi\Delta$ propagator in the integrand of Eq. (82) is the $\pi\pi N$ cut along the real axis between $\pm p_0$ ($-p_0 \leq p \leq p_0$) which is obtained by solving

$$E = E_\pi(p_0) + [(m_\pi + m_N)^2 + p_0^2]^{1/2}. \quad (84)$$

For finding the resonance poles on uu -sheet with $\text{Im } p_0 \leq 0$, the integration contour C_2 of Eq. (82) must be chosen below this cut which is the dashed line in Fig.6. There is also a singularity in the integrand of Eq. (82) at momentum $p = p_x$, which satisfies

$$E - E_\pi(p_x) - E_\Delta(p_x) - \Sigma_\Delta(p_x, E) = 0. \quad (85)$$

Physically, this singularity corresponds to the $\pi\Delta$ two-body scattering state. For E with large imaginary part, p_x can be below the $\pi\pi N$ cut as also indicated in Fig.6. Therefore the integration contour of momentum p must be chosen to be below the $\pi\pi N$ cut (dashed line) and the singularity p_x , such as the contour C_2 shown in Fig.6.

The singularity position q_0 of the propagator in Eq. (83) depends on spectator momentum p

$$E - E_\pi(p) = [(E_\pi(q_0) + E_N(q_0))^2 + p^2]^{1/2}. \quad (86)$$

Therefore the singularity q_0 moves along the dashed curve in Fig.7 when the momentum p varies along the path C_2 of Fig.6. To analytically continue $\Sigma_\Delta(p, E)$ from positive energy

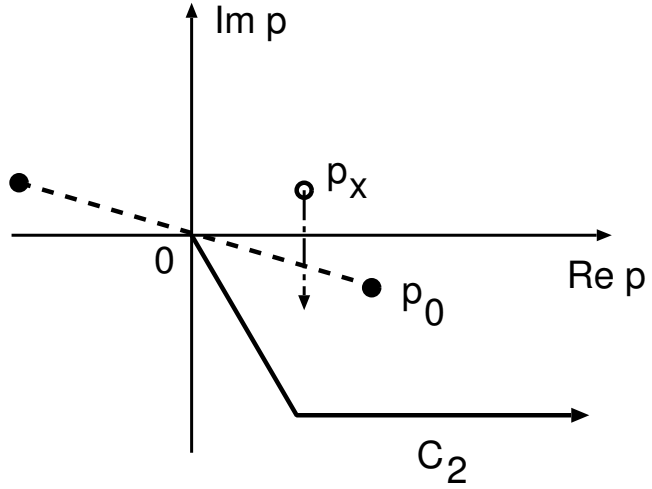


FIG. 6: Contour C_2 for calculating the $\pi\Delta$ self energy on unphysical sheet. See the text for the explanations of the dashed line and the singularity p_x .

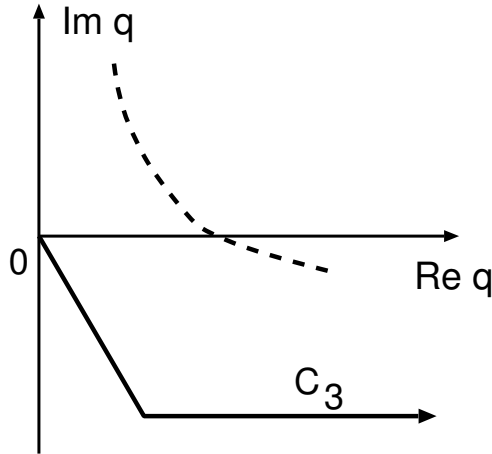


FIG. 7: Contour C_3 for calculating the πN self energy on the unphysical sheet. Dashed curve is the singularity q_0 of the propagator in Eq. (83), which depends on the spectator momentum p on the contour C_2 of Fig.6.

E to the un-physical plane with $\text{Im } p \leq 0$, we need to choose the contour C_3 of Eq. (83) which must be below q_0 . A possible contour C_3 is the solid curve in Fig.7.

To verify the numerical procedures described above, we again consider non-relativistic

kinematics and monopole form factor. With the similar analytic form Eq. (67), we have

$$\Sigma_\Delta(p, E) = \frac{\pi\mu_{\pi N}g_{\Delta,\pi N}^2\beta_{\Delta,\pi N}^3}{2(\bar{k} + i\beta_{\Delta,\pi N})^2} \quad (87)$$

where

$$\bar{k} = \left[2\mu_{\pi N} \left(E - 2m_\pi - m_N - \frac{p^2}{2\mu_{\pi N}} \right) \right]^{1/2}, \quad (88)$$

with $\mu_{\pi\pi N} = m_\pi(m_\pi + m_N)/(2m_\pi + m_N)$. With Eq. (87), we can solve Eq. (85) and verify its relation with $\pi\pi N$ cut as discussed above and illustrated in Fig.6. Eq. (87) and the chosen monopole form factor also allow us to get

$$\Sigma_{\pi\Delta} = \int_{c_2} p^2 dp \frac{g_{N^*,\pi\Delta}^2}{(1 + p^2/\beta_{N^*,\pi\Delta}^2)^2} \frac{1}{D_{\pi\Delta}(p, E)} \quad (89)$$

with

$$D_{\pi\Delta}(p, E) = E - m_\pi - m_\Delta - \frac{p^2}{2\mu_{\pi\Delta}} - \frac{\pi\mu_{\pi N}g_{\Delta,\pi N}^2\beta_{\Delta,\pi N}^3}{2(\bar{k} + i\beta_{\Delta,\pi N})^2}. \quad (90)$$

Unfortunately, Eq. (89) can not be integrated out analytically for directly checking our numerical procedure for searching resonance poles.

We test our analytic continuation method by the following procedure. We calculate Eq. (89) numerically to find the pole position E_R by solving $E_R - M_0 - \Sigma_{\pi\Delta}(E_R) = 0$ of the denominator of Eq. (81). With the parameters:

$$\begin{aligned} \beta_{N^*,\pi\Delta} &= 800 \text{MeV}, \quad g_{N^*,\pi\Delta} = 0.02 \text{MeV}^{-1/2}, \\ \beta_{\Delta,\pi N} &= 200 \text{MeV}, \quad g_{\Delta,\pi N} = 0.05 \text{MeV}^{-1/2}, \\ M_0 &= 650 \text{MeV} + m_\pi + m_N, \end{aligned}$$

we find $E_R = (1679.1, -33.6i)$ MeV. The pole position is obtained numerically by Newton's method in Appendix A. We then construct an approximate propagator

$$G_{N^*}^{approx}(E) = \frac{1}{E - E_R}. \quad (91)$$

For the positive E , we find that $G_{N^*}^{approx}(E)$ is in good agreement with the direct calculation of $G_{N^*}(E) = 1/(E - M_0 - \Sigma_{\pi\Delta}(E))$ by using Eq. (89). The results are shown in Fig.8. It is clear that the resonance pole found by our analytic continuation method can reproduce what is expected for a resonance propagator for real positive E . In this way our numerical procedure is justified and can be applied to solve Eqs. (81) - (83).

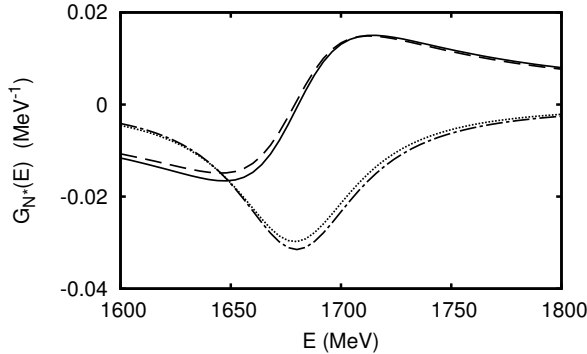


FIG. 8: N^* Green function. The solid (dash-dotted) curve is the real (imaginary) part of exact Green function $G_{N^*}(E) = 1/(E - M_0 - \Sigma_{\pi\Delta}(E))$. They are compared with the dashed (dotted) curve of the real (imaginary) part of the approximate Green function $G_{N^*}^{approx}$.

III. EXTRACTION OF RESONANCE PARAMETERS

The complex resonance energy is the position of the pole of the scattering amplitude which is on the Riemann sheet nearest to the physical sheet. In this section, we explain how the residues of resonance poles are extracted from a dynamical model and how the transition form factor of the resonance are defined by the residue.

A. Pole expansion of scattering amplitudes

We assume that scattering amplitude T is written as the sum of meson-exchange non-resonant amplitude $t^{non-res}$ and resonant amplitude, which is expressed by N^* propagator $1/D(E)$ and the vertex between N^* and a final meson-baryon state $\bar{\Gamma}_f$ or an initial meson-baryon state $\bar{\Gamma}_i$,

$$T = t^{non-res} + \frac{\bar{\Gamma}_f \bar{\Gamma}_i}{D(E)}, \quad (92)$$

$$D(E) = E - M_0 - \Sigma(E), \quad (93)$$

where M_0 is the mass of the bare resonance which is not coupled with meson-baryon continuum state and $\Sigma(E)$ is the selfenergy of N^* . The resonance energy M is given as

the pole position of the propagator on complex energy plane,

$$D(M) = 0. \quad (94)$$

We can write the amplitude near resonance pole by Laurent expansion as

$$T(E) = \frac{R}{E - M} + C_0 + C_1(E - M) + \dots, \quad (95)$$

where

$$R = \frac{\bar{\Gamma}_f(M)\bar{\Gamma}_i(M)}{D'(M)}, \quad (96)$$

$$C_0 = t^{non-res}(M) + \frac{\bar{\Gamma}'_f(M)\bar{\Gamma}_i(M) + \bar{\Gamma}_f(M)\bar{\Gamma}'_i(M)}{D'(M)} - \frac{D''(M)}{2(D'(M))^2}\bar{\Gamma}_f(M)\bar{\Gamma}_i(M). \quad (97)$$

Then the resonance form factor which describes the transition into channel c can be written as

$$F_c(W) = \Gamma_c(M)/\sqrt{D'(M)}. \quad (98)$$

The above expressions are valid in the case of the meson-baryon system coupled with one N^* . Expressions for two N^* 's are given in Appendix B.

B. N-N* transition form factor

The residue of the πN elastic scattering amplitude characterizes the strength of the coupling of the resonance with πN channel and the transition form factor of N^* can be obtained in terms of the residue of the pole on complex energy plane. We apply the procedure of the pole expansion to a dynamical coupled channel model which describes MB or $\gamma N \rightarrow \pi N$ reactions. The details of our dynamical model will be given in Section IV, so here we present essential points of the model for extracting resonance parameters.

In our dynamical model the scattering amplitude of meson-baryon states from MB to $M'B'$ is written as the sum of a non-resonant and a resonant amplitude,

$$T_{M'B',MB}(p', p, E) = t_{M'B',MB}^{non-res}(p', p, E) + t_{M'B',MB}^{res}(p', p, E). \quad (99)$$

The resonant amplitude is given as

$$t_{M'B',MB}^{res}(p', p, E) = \sum_{i,j} \bar{\Gamma}_{M'B',j} [D(E)]_{i,j} \bar{\Gamma}_{MB,i} \quad (100)$$

where we sum bare nucleon resonance states i, j . The propagator of the resonant state N^* is

$$[D(E)^{-1}]_{i,j}(E) = (E - M_{N_i^*}^0) \delta_{i,j} - \Sigma_{i,j}(E), \quad (101)$$

where $M_{N^*}^0$ is the bare mass of N^* and $\Sigma_{i,j}(E)$ is the selfenergy. So far we found resonance from the resonant amplitude and the resonance energy M is determined from

$$\det[D(M)^{-1}] = 0. \quad (102)$$

The scattering amplitude πN and $\gamma N \rightarrow \pi N$ amplitudes can be written near the resonance energy M by using the Laurent expansion as

$$T_{M'B',MB}(p_{M'B'}^0, p_{MB}^0, M) = \frac{C_{M'B',MN}^{-1}}{E - M} + C_{M'B',MB}^0 + C_{M'B',MB}^1(E - M) + \dots, \quad (103)$$

where p^0 is the on-shell momentum for the total energy M ,

$$E_M(p_{MB}^0) + E_B(p_{MB}^0) = M. \quad (104)$$

The first term in Eq. (103) represents the resonance pole and the next order correction term is the constant C^0 . The above expression will be useful in the E region where we have no other singularity of $T(E)$. For example, the applicability of the above formula can be limited by the opening of a new channel. C^{-1} is the residue of the amplitude and given as

$$C_{M'B',MB}^{-1} = \bar{\Gamma}_{M'B'}^R \bar{\Gamma}_{MB}^R, \quad (105)$$

$$\bar{\Gamma}_{MB}^R = \sum_i \chi_i \bar{\Gamma}_{MB,i}, \quad (106)$$

where χ_i is the eigenfunction of the inverse of N^* propagator and satisfies

$$\sum_j (M_{N_i^*}^0 \delta_{ij} + \Sigma_{ij}(M)) \chi_j = M \chi_i. \quad (107)$$

We can approximate the propagator of N^* around the pole with this χ_i as

$$[D(E)]_{ij} \sim \frac{\chi_i \chi_j}{E - M}. \quad (108)$$

If there is only one bare N^* state, it is easy to see that

$$\chi = \frac{1}{\sqrt{1 - \Sigma'(M)}}, \quad (109)$$

where $\Sigma'(M) = [d\Sigma/dE]_{E=M}$. The constant term C^0 in Eq. (103) has contributions from non-resonant and resonant amplitudes, that is

$$C_0 = t^{non-res}(p_{M'B'}^0, p_{MB}^0, M) + \frac{\partial}{\partial W} \left[\sum_{i,j} \bar{\Gamma}_{M'B',i}(p_{M'B'}^0, W) G_{N*}^{ij}(W) \bar{\Gamma}_{MB,i}(p_{MB}^0, W) (W - M) \right] |_{W=M}. \quad (110)$$

The relation between πN elastic scattering amplitude $F_{\pi N, \pi N}$ with on-shell momentum and S-matrix is given by

$$F_{\pi N, \pi N}(E) = -\pi \frac{p^0 E_N(p^0) E_\pi(p^0)}{E} T_{\pi N, \pi N}(p^0, p^0, E) \quad (111)$$

$$= \frac{S_{\pi N, \pi N}(E) - 1}{2i}. \quad (112)$$

The residue of the resonance pole on scattering amplitude satisfies

$$\lim_{E \rightarrow M} F_{\pi N, \pi N}(E) \simeq \frac{Re^{i\phi}}{M - E}, \quad (113)$$

and

$$Re^{i\phi} = \pi \frac{p^0 E_N(p^0) E_\pi(p^0)}{M} \bar{\Gamma}_{\pi N}^R \bar{\Gamma}_{\pi N}^R. \quad (114)$$

Thus we can obtain the residue $Re^{i\phi}$ of the resonance pole on complex energy plane. The relation between the residue and the transition form factor $\bar{\Gamma}_{\pi N}^R$ is also given.

IV. DYNAMICAL MODEL OF MESON PRODUCTION REACTIONS

A. Model Hamiltonian

In this subsection we present a model Hamiltonian for constructing a coupled-channel reaction model with γN , πN , ηN and $\pi\pi N$ channels. Since significant parts of the $\pi\pi N$ production are known experimentally to be through the unstable states $\pi\Delta$, ρN and σN , we will also include bare Δ , ρ and σ degrees of freedom in our formulation. Furthermore, we introduce bare N^* states to represent the quark-core components of the nucleon resonances. The model is expected to be valid up to $E = 2$ GeV below which $\pi\pi N$ production is dominant and we neglect KY , ωN and three pion production processes.

Similar to the model of Refs. [34, 45] (commonly called the SL model), our starting point is a set of Lagrangians describing the interactions between mesons ($M = \gamma, \pi, \eta, \rho, \sigma \dots$) and baryons ($B = N, \Delta, N^* \dots$). These Lagrangian are constrained by various well-established symmetry properties, such as the invariance under isospin, parity, and gauge transformation. The chiral symmetry is also implemented as much as we can. The considered Lagrangians are given in Appendix C. By applying the standard canonical quantization, we obtain a Hamiltonian of the following form

$$\begin{aligned} H &= \int h(\vec{x}, t = 0) d\vec{x} \\ &= H_0 + H_I, \end{aligned} \quad (115)$$

where $h(\vec{x}, t)$ is the Hamiltonian density constructed from the starting Lagrangians and the conjugate momentum field operators. In Eq.(115), H_0 is the free Hamiltonian and

$$H_I = \sum_{M, B, B'} \Gamma_{MB \leftrightarrow B'} + \sum_{M, M', M''} h_{M'M'' \leftrightarrow M}, \quad (116)$$

where $\Gamma_{MB \leftrightarrow B'}$ describes the absorption and emission of a meson(M) by a baryon(B) such as $\pi N \leftrightarrow N$ and $\pi N \leftrightarrow \Delta$, and $h_{M'M'' \leftrightarrow M}$ describes the vertex interactions between mesons such as $\pi\pi \leftrightarrow \rho$ and $\gamma\pi \leftrightarrow \pi$. Clearly, it is a non-trivial many body problem to calculate meson-baryon scattering and meson production reaction amplitudes from the Hamiltonian defined by Eqs.(115)-(116). To obtain a manageable reaction model, we apply a unitary transformation method[34, 35] to derive an effective Hamiltonian from Eqs.(115)-(116). The essential idea of the employed unitary transformation method is to eliminate the unphysical vertex interactions $MB \rightarrow B'$ with masses $m_M + m_B < m_{B'}$ from the Hamiltonian and absorb their effects into $MB \rightarrow M'B'$ two-body interactions. The resulting effective Hamiltonian is energy independent and hence is easy to be used in developing reaction models and performing many-particle calculations. The details of this method is explained in the Appendix of Ref.[34].

Our main step is to derive from Eqs.(115)-(116) an effective Hamiltonian which contains interactions involving $\pi\pi N$ three-particle states. This is accomplished by applying the unitary transformation method up to the third order in interaction H_I of Eq.(116). The resulting effective Hamiltonian is of the following form

$$H_{eff} = H_0 + V, \quad (117)$$

with

$$H_0 = \sum_{\alpha} K_{\alpha}, \quad (118)$$

where $K_{\alpha} = \sqrt{m_{\alpha}^2 + \vec{p}_{\alpha}^2}$ is the free energy operator of particle α with a mass m_{α} , and the interaction Hamiltonian is

$$V = \Gamma_V + v_{22} + v', \quad (119)$$

where

$$\Gamma_V = \left\{ \sum_{N^*} \left(\sum_{MB} \Gamma_{N^* \rightarrow MB} + \Gamma_{N^* \rightarrow \pi\pi N} \right) + \sum_{M^*} h_{M^* \rightarrow \pi\pi} \right\} + \{c.c.\}, \quad (120)$$

$$v_{22} = \sum_{MB, M'B'} v_{MB, M'B'} + v_{\pi\pi}. \quad (121)$$

Here *c.c.* denotes the complex conjugate of the terms on its left-hand-side. In the above equations, $MB = \gamma N, \pi N, \eta N, \pi\Delta, \rho N, \sigma N$ represent the considered meson-baryon states. The resonance associated with the *bare* baryon state N^* is induced by the vertex interactions $\Gamma_{N^* \rightarrow MB}$ and $\Gamma_{N^* \rightarrow \pi\pi N}$. Similarly, the *bare* meson states $M^* = \rho, \sigma$ can develop into resonances through the vertex interaction $h_{M^* \rightarrow \pi\pi}$. These vertex interactions are illustrated in Fig.9(a). Note that the masses $M_{N^*}^0$ and $m_{M^*}^0$ of the bare states N^* and M^* are the parameters of the model which will be determined by fitting the πN and $\pi\pi$ scattering data. They differ from the empirically determined resonance positions by mass shifts which are due to the coupling of the bare states with the meson-baryon scattering states. It is thus reasonable to speculate that these bare masses can be identified with the mass spectrum predicted by the hadron structure calculations which do not account for the meson-baryon continuum scattering states, such as the calculations based on the constituent quark models which do not have meson-exchange quark-quark interactions.

In Eq. (121), $v_{MB, M'B'}$ is the non-resonant meson-baryon interaction and $v_{\pi\pi}$ is the non-resonant $\pi\pi$ interaction. They are illustrated in Fig. 9(b). The third term in Eq. (119) describes the non-resonant interactions involving $\pi\pi N$ states

$$v' = v_{23} + v_{33} \quad (122)$$

with

$$v_{23} = \sum_{MB} [(v_{MB, \pi\pi N}) + (c.c.)]$$

$$v_{33} = v_{\pi\pi N, \pi\pi N}.$$

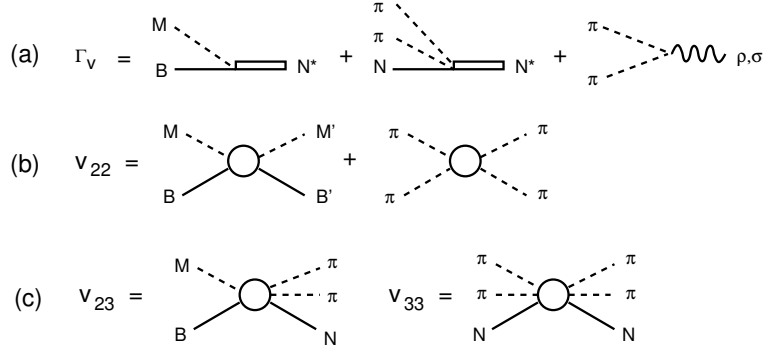
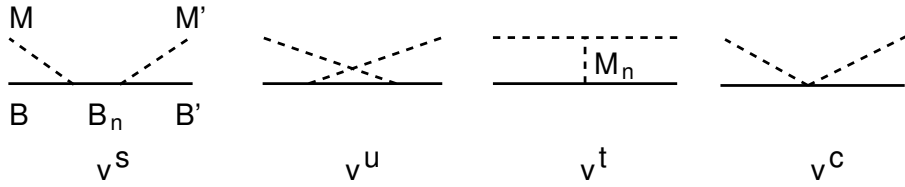


FIG. 9: Basic mechanisms of the Model Hamiltonian defined in Eqs. (120)-(122).

FIG. 10: Mechanisms for $v_{MB,M'B'}$ of Eq. (121): (a) direct s-channel, (b) crossed u-channel, (c) one-particle-exchange t-channel, (d) contact interactions.

They are illustrated in Fig. 9(c). All of these interactions are defined by the tree-diagrams generated from the considered Lagrangians. They are illustrated in Fig. 10 for two-body interactions $v_{MB,M'B'}$ and in Fig. 11 for $v_{MB,\pi\pi N}$. Some leading mechanisms of $v_{\pi\pi}$ and $v_{\pi\pi N, \pi\pi N}$ are illustrated in Fig. 12. The matrix elements of these interactions are calculated from the usual Feynman amplitudes with their time components in the propagators of intermediate states defined by the three momenta of the initial and final states, as specified by the unitary transformation methods. Thus they are independent of the collision energy E .

B. Two body $MB \rightarrow MB$ amplitude

With the Hamiltonian defined by Eqs. (117)-(122), we follow the formulation of Ref. [11] to define the scattering S-matrix as

$$S_{ab}(E) = \delta_{ab} - (2\pi)iT_{ab}(E), \quad (123)$$

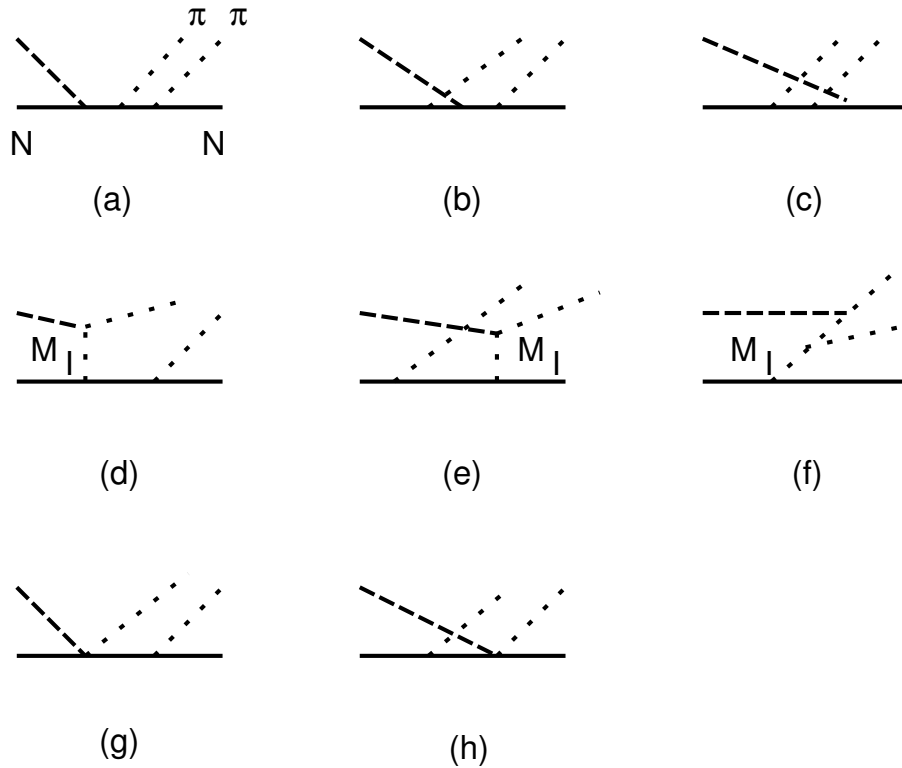


FIG. 11: Examples of non-resonant mechanisms of $v_{MN, \pi\pi N}$ with $M = \pi$ or γ (denoted by long-dashed lines). M_I denotes the intermediate mesons (π, ρ, ω).

FIG. 12: Examples of non-resonant mechanisms of $v_{\pi\pi}$ and $v_{\pi\pi N, \pi\pi N}$

where the scattering T-matrix is defined by

$$T_{ab}(E) = \langle a | T(E) | b \rangle$$

with

$$T(E) = V + V \frac{1}{E - H_0 + i\epsilon} T(E). \quad (124)$$

Since the interaction V , defined by Eqs. (119)-(122), is energy independent, it is rather straightforward to follow the formal scattering theory given in Ref. [11] to show that

Eq. (124) leads to the following unitarity condition

$$(T(E) - T^\dagger(E))_{ab} = -2\pi i \sum_c T_{ac}^\dagger(E) \delta(E_c - E) T_{cb}(E), \quad (125)$$

where a, b, c are the reaction channels in the considered energy region.

Our task is to derive from Eq. (124) a set of dynamical coupled-channel equations for practical calculations within the model space $N^* \oplus MB \oplus \pi\pi N$. In the derivations, the unitarity condition Eq. (125) must be maintained exactly. We achieve this rather complex task by applying the standard projection operator techniques[12], similar to that employed in a study[46] of πNN scattering. The details of our derivations are given in Appendix B of Ref. [28]. To explain the coupled-channel equations, it is sufficient to present the formula obtained from setting $\Gamma_{N^* \rightarrow \pi\pi N} = 0$ in the derivations. The resulting model is defined by Eqs. (B74)-(B96) in Appendix B of Ref. [28]. Here we explain these equations and discuss their dynamical content.

The resulting $MB \rightarrow M'B'$ amplitude $T_{MB \rightarrow M'B'}$ in each partial wave is illustrated in Fig. 13. It can be written as

$$T_{MB, M'B'}(E) = t_{MB, M'B'}(E) + t_{MB, M'B'}^R(E), \quad (126)$$

The second term in the right-hand-side of Eq.(126) is the resonant term defined by

$$t_{MB, M'B'}^R(E) = \sum_{N_i^*, N_j^*} \bar{\Gamma}_{MB \rightarrow N_i^*}(E) [D(E)]_{i,j} \bar{\Gamma}_{N_j^* \rightarrow M'B'}(E), \quad (127)$$

with

$$[D(E)^{-1}]_{i,j}(E) = (E - M_{N_i^*}^0) \delta_{i,j} - \bar{\Sigma}_{i,j}(E), \quad (128)$$

where $M_{N^*}^0$ is the bare mass of the resonant state N^* , and the self-energies are

$$\bar{\Sigma}_{i,j}(E) = \sum_{MB} \Gamma_{N_i^* \rightarrow MB} G_{MB}(E) \bar{\Gamma}_{MB \rightarrow N_j^*}(E). \quad (129)$$

The dressed vertex interactions in Eq.(127) and Eq.(129) are (defining $\Gamma_{MB \rightarrow N^*} = \Gamma_{N^* \rightarrow MB}^\dagger$)

$$\bar{\Gamma}_{MB \rightarrow N^*}(E) = \Gamma_{MB \rightarrow N^*} + \sum_{M'B'} t_{MB, M'B'}(E) G_{M'B'}(E) \Gamma_{M'B' \rightarrow N^*}, \quad (130)$$

$$\bar{\Gamma}_{N^* \rightarrow MB}(E) = \Gamma_{N^* \rightarrow MB} + \sum_{M'B'} \Gamma_{N^* \rightarrow M'B'} G_{M'B'}(E) t_{M'B', MB}(E). \quad (131)$$

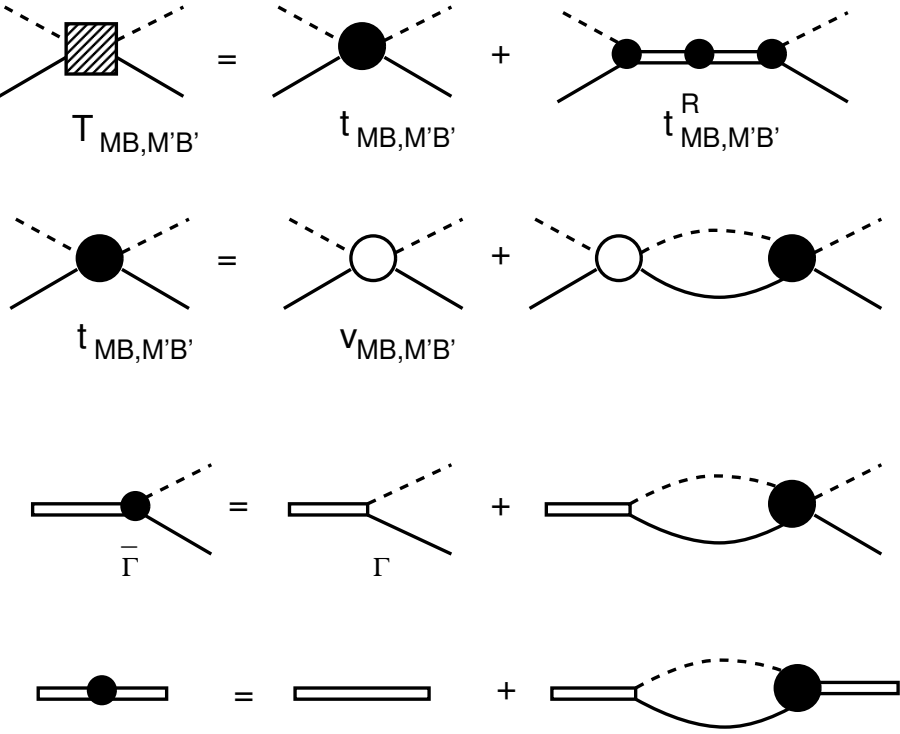


FIG. 13: Graphical representations of Eqs. (126)-(129).

The meson-baryon propagator G_{MB} in the above equations takes the following form

$$G_{MB}(E) = \frac{1}{E - K_B - K_M - \Sigma_{MB}(E) + i\epsilon}, \quad (132)$$

where the mass shift $\Sigma_{MB}(E)$ depends on the considered MB channel. It is $\Sigma_{MB}(E) = 0$ for the stable particle channels $MB = \pi N, \eta N$. For channels containing an unstable particle, such as $MB = \pi\Delta, \rho N, \sigma N$, we have

$$\Sigma_{MB}(E) = [< MB | g_V \frac{P_{\pi\pi N}}{E - K_\pi - K_\pi - K_N + i\epsilon} g_V^\dagger | MB >]_{un-connected} \quad (133)$$

with

$$g_V = \Gamma_{\Delta \rightarrow \pi N} + h_{\rho \rightarrow \pi\pi} + h_{\sigma \rightarrow \pi\pi}. \quad (134)$$

In Eq. (133) "un-connected" means that the stable particle, π or N , of the MB state is a spectator in the $\pi\pi N$ propagation. Thus $\Sigma_{MB}(E)$ is just the mass renormalization of the unstable particle in the MB state.

It is important to note that the resonant amplitude $t_{M'B',MB}^R(E)$ is influenced by the non-resonant amplitude $t_{M'B',MB}(E)$, as seen in Eqs. (127)-(131). In particular,

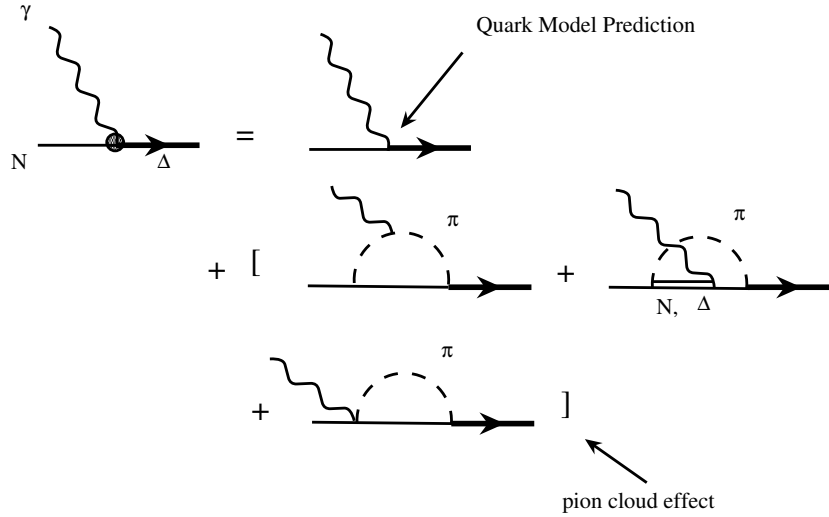


FIG. 14: Graphical representation of the dressed $\bar{\Gamma}_{\Delta,\gamma N}$ interpreted in Refs.[34, 45].

Eqs. (130)-(131) describe the meson cloud effects on N^* decays, as illustrated in Fig. 14 for the $\Delta \rightarrow \gamma N$ decay interpreted in Refs. [34, 45]. This feature of our formulation is essential in interpreting the extracted resonance parameters.

The non-resonant amplitudes $t_{MB,M'B'}$ in Eq. (126) and Eqs. (130)-(131) are defined by the following coupled-channel equations

$$t_{MB,M',B'}(E) = V_{MB,M'B'}(E) + \sum_{M''B''} V_{MB,M''B''}(E) G_{M''B''}(E) t_{M''B'',M'B'}(E) \quad (135)$$

with

$$V_{MB,M'B'}(E) = v_{MB,M'B'} + Z_{MB,M'B'}(E). \quad (136)$$

Here $Z_{MB,M'B'}(E)$ contains the effects due to the coupling with $\pi\pi N$ states. It has the following form

$$Z_{MB,M'B'}(E) = \langle MB | F \frac{P_{\pi\pi N}}{E - H_0 - \hat{v}_{\pi\pi N} + i\epsilon} F^\dagger | M'B' \rangle$$

$$-[\delta_{MB,M'B'} \Sigma_{MB}(E)] \quad (137)$$

with

$$\hat{v}_{\pi\pi N} = v_{\pi N, \pi N} + v_{\pi\pi} + v_{\pi\pi N, \pi\pi N}, \quad (138)$$

$$F = g_V + v_{MB, \pi\pi N}, \quad (139)$$

where g_V has been defined in Eq. (134). Note that the second term in Eq. (137) is the effect which is already included in the mass shifts Σ_{MB} of the propagator Eq. (132) and must be removed to avoid double counting.

The appearance of the projection operator $P_{\pi\pi N}$ in Eqs. (133) and (137) is the consequence of the unitarity condition Eq. (125). To isolate the effects entirely due to the vertex interaction $g_V = \Gamma_{\Delta \rightarrow \pi N} + h_{\rho \rightarrow \pi\pi} + h_{\sigma \rightarrow \pi\pi}$, we use the operator relation Eq. (B33) of Appendix B in Ref. [28] to decompose the $\pi\pi N$ propagator of Eq. (137) to write

$$Z_{MB, M'B'}(E) = Z_{MB, M'B'}^{(E)}(E) + Z_{MB, M'B'}^{(I)}(E). \quad (140)$$

The first term is

$$Z_{MB, M'B'}^{(E)}(E) = \langle MB | g_V \frac{P_{\pi\pi N}}{E - H_0 + i\epsilon} g_V^\dagger | M'B' \rangle - [\delta_{MB, M'B'} \Sigma_{MB}(E)]. \quad (141)$$

Obviously, $Z_{MB, M'B'}^{(E)}(E)$ is the one-particle-exchange interaction between unstable particle channels $\pi\Delta$, ρN , and σN , as illustrated in Fig. 15. The second term of Eq. (140) is

$$\begin{aligned} Z_{MB, M'B'}^{(I)}(E) &= \langle MB | F \frac{P_{\pi\pi N}}{E - H_0 + i\epsilon} t_{\pi\pi N, \pi\pi N}(E) \frac{P_{\pi\pi N}}{E - H_0 + i\epsilon} F^\dagger | M'B' \rangle \\ &+ \langle MB | g_V \frac{P_{\pi\pi N}}{E - H_0 + i\epsilon} v_{MB, \pi\pi N}^\dagger | B'M' \rangle \\ &+ \langle MB | v_{MB, \pi\pi N} \frac{P_{\pi\pi N}}{E - H_0 + i\epsilon} g_V^\dagger | M'B' \rangle \\ &+ \langle MB | v_{MB, \pi\pi N} \frac{P_{\pi\pi N}}{E - H_0 + i\epsilon} v_{MB, \pi\pi N}^\dagger | M'B' \rangle. \end{aligned} \quad (142)$$

Some of the leading terms of $Z_{MB, M'B'}^{(I)}(E)$ are illustrated in Fig. 16. Here $t_{\pi\pi N, \pi\pi N}(E)$ is a three-body scattering amplitude defined by

$$t_{\pi\pi N, \pi\pi N}(E) = \hat{v}_{\pi\pi N} + \hat{v}_{\pi\pi N} \frac{1}{E - K_\pi - K_\pi - K_N - \hat{v}_{\pi\pi N} + i\epsilon} \hat{v}_{\pi\pi N} \quad (143)$$

where $\hat{v}_{\pi\pi N}$ has been defined in Eq. (138). Few leading terms of Eq. (143) due to the direct s-channel interaction v^s of $v_{\pi N, \pi N}$ are shown in Fig. 17. These terms involve the

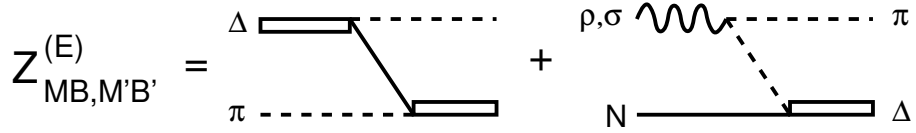


FIG. 15: One-particle-exchange interactions $Z_{\pi\Delta,\pi\Delta}^{(E)}(E)$, $Z_{\rho N,\pi\Delta}^{(E)}$ and $Z_{\sigma N,\pi\Delta}^{(E)}$ of Eq. (141).

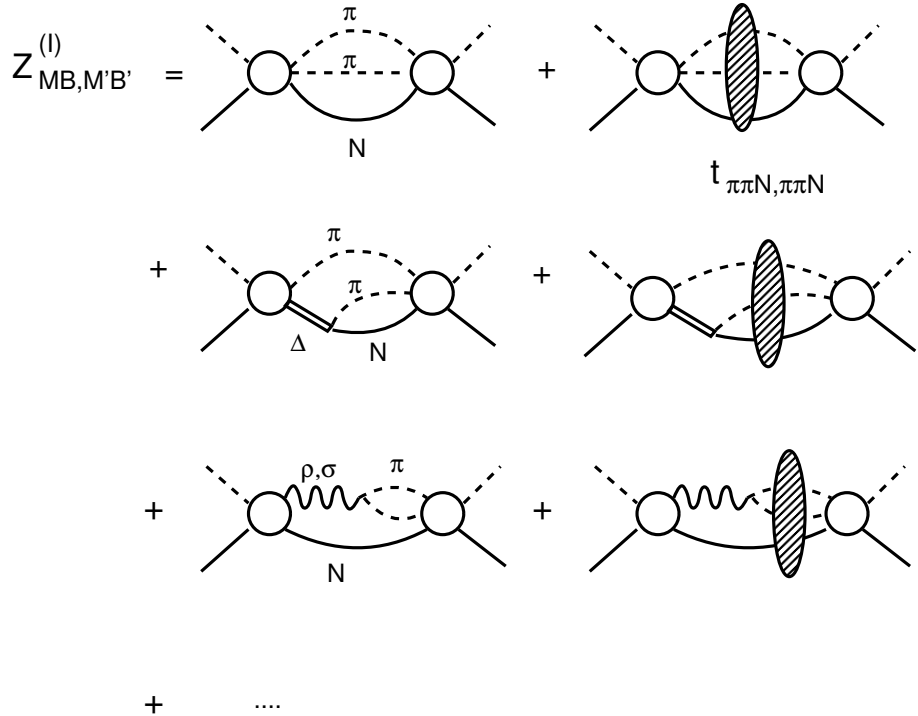


FIG. 16: Examples of mechanisms included in $Z_{MB,M'B'}^{(I)}(E)$ of Eq. (142).

$\pi\pi N$ propagator $1/(E - K_\pi - K_\pi - K_N + i\epsilon)$ and obviously can generate $\pi\pi N$ cut effects which are due to the $\pi\pi N$ vertex. This observation indicates that the πN scattering equation of Aaron, Amado and Young[47] can be related to our formulation if the interactions which are *only* determined by the $\pi\pi N$ vertex are kept in the equations presented above.

C. $MB \rightarrow \pi\pi N$ amplitudes

The amplitudes $T_{MB,M'B'} = t_{MB,M'B'} + t_{MB,M'B'}^R$ defined by Eq.(126) can be used directly to calculate the cross sections of $\pi N \rightarrow \pi N, \eta N$ and $\gamma N \rightarrow \pi N, \eta N$ reactions. They are also the input to the calculations of the two-pion production amplitudes. The

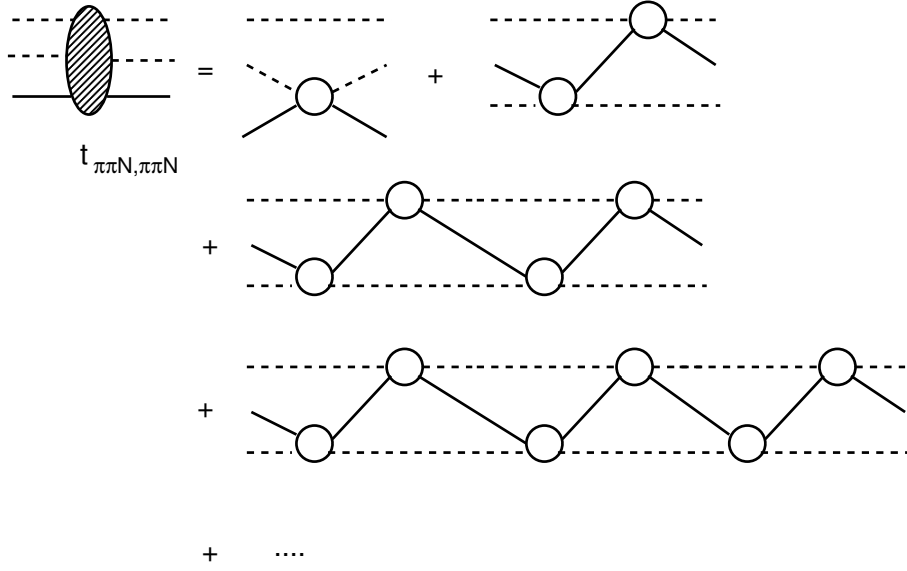


FIG. 17: Some of the leading order terms of $t_{\pi\pi N, \pi\pi N}$ of Eq. (143). The open circle represents the direct s-channel interaction v^s illustrated in Fig. 10 for the $MB = M'B' = \pi N$ case.

two-pion production amplitudes resulted from our derivations given in Appendix B of Ref. [28] are illustrated in Fig. 18. They can be cast exactly into the following form

$$T_{\pi\pi N, MB}(E) = T_{\pi\pi N, MB}^{dir}(E) + T_{\pi\pi N, MB}^{\pi\Delta}(E) + T_{\pi\pi N, MB}^{\rho N}(E) + T_{\pi\pi N, MB}^{\sigma N}(E) \quad (144)$$

with

$$T_{\pi\pi N, MB}^{dir}(E) = \langle \psi_{\pi\pi N}^{(-)}(E) | \sum_{M'B'} v_{\pi\pi N, M'B'} [\delta_{M'B', MB} + G_{M'B'}(E)(t_{M'B', MB}(E) + t_{M'B', MB}^R)] | MB \rangle, \quad (145)$$

$$T_{\pi\pi N, MB}^{\pi\Delta}(E) = \langle \psi_{\pi\pi N}^{(-)}(E) | \Gamma_{\Delta \rightarrow \pi N}^\dagger G_{\pi\Delta}(E) [t_{\pi\Delta, MB}(E) + t_{\pi\Delta, MB}^R(E)] | MB \rangle, \quad (146)$$

$$T_{\pi\pi N, MB}^{\rho N}(E) = \langle \psi_{\pi\pi N}^{(-)}(E) | h_{\rho \rightarrow \pi\pi}^\dagger G_{\rho N}(E) [t_{\rho N, MB}(E) + t_{\rho N, MB}^R(E)] | MB \rangle, \quad (147)$$

$$T_{\pi\pi N, MB}^{\sigma N}(E) = \langle \psi_{\pi\pi N}^{(-)}(E) | h_{\sigma \rightarrow \pi\pi}^\dagger G_{\sigma N}(E) [t_{\sigma N, MB}(E) + t_{\sigma N, MB}^R(E)] | MB \rangle. \quad (148)$$

In the above equations, the $\pi\pi N$ scattering wave function is defined by

$$\langle \psi_{\pi\pi N}^{(-)}(E) | = \langle \pi\pi N | \Omega_{\pi\pi N}^{(-)\dagger}(E), \quad (149)$$

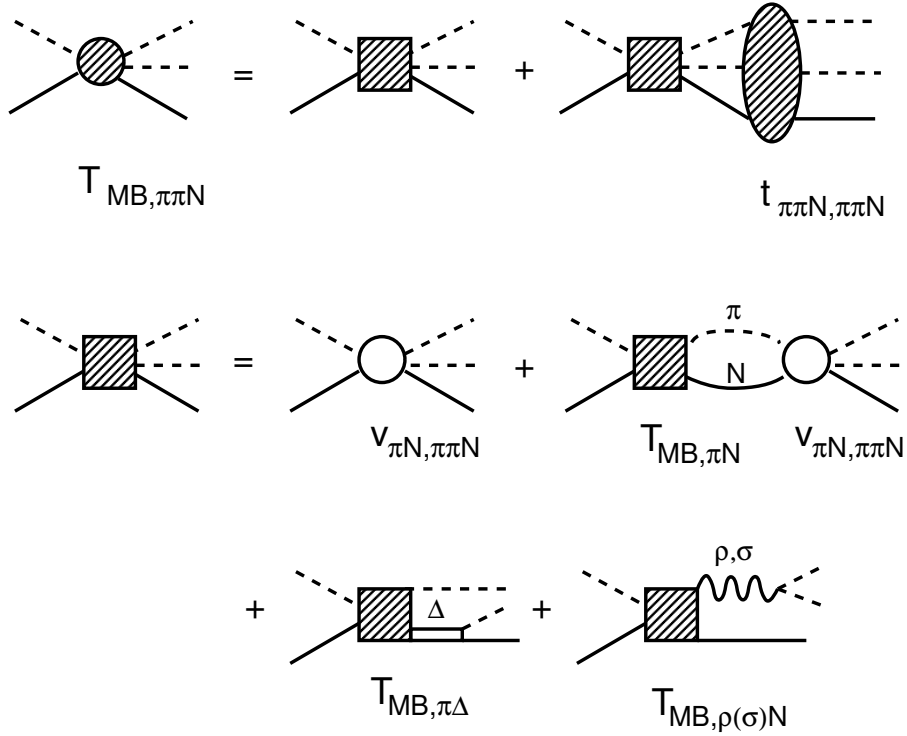


FIG. 18: Graphical representations of $T_{\pi\pi N, MB}$ defined by Eqs. (144)-(148).

where the scattering operator is defined by

$$\Omega_{\pi\pi N}^{(-)\dagger}(E) = \langle \pi\pi N | [1 + t_{\pi\pi N, \pi\pi N}(E) \frac{1}{E - K_\pi - K_\pi - K_N + i\epsilon}] \rangle. \quad (150)$$

Here the three-body scattering amplitude $t_{\pi\pi N, \pi\pi N}(E)$ is determined by the non-resonant interactions $v_{\pi\pi}$, $v_{\pi N, \pi N}$ and $v_{\pi\pi N, \pi\pi N}$, as defined by Eq. (143).

We note here that the direct production amplitude $T_{\pi\pi N, MB}^{dir}(E)$ of Eq. (145) is due to $v_{\pi\pi N, MB}$ interaction illustrated in Fig. 11, while the other three terms are through the unstable $\pi\Delta$, ρN , and σN states. Each term has the contributions from the non-resonant amplitude $t_{M'B', MB}(E)$ and resonant term $t_{M'B', MB}^R(E)$. As seen in Eq. (127)-(131), the resonant amplitude $t_{M'B', MB}^R(E)$ is influenced by the non-resonant amplitude $t_{M'B', MB}(E)$. This is an important consequence of unitarity condition Eq. (125).

D. Partial wave expansion of $MB \rightarrow MB$ amplitudes

We solve Eq. (135) in the partial-wave representation. To proceed, we follow the convention of Goldberger and Watson[11] to normalize the plane-wave state $|\vec{k}\rangle$ by

setting $\langle \vec{k}|\vec{k}' \rangle = \delta(\vec{k} - \vec{k}')$. In the center of mass frame, Eq. (123) then leads to the following formula of the cross section of $M(\vec{k}) + B(-\vec{k}) \rightarrow M(\vec{k}') + B(-\vec{k}')$ for stable particle channels $MB, M'B' = \gamma N, \pi N, \eta N$

$$\frac{d\sigma}{d\Omega} = \frac{(4\pi)^2}{k^2} \rho_{M'B'}(k') \rho_{MB}(k) \frac{1}{(2j_M + 1)(2j_B + 1)} \sum_{m_{j_M}, m_{j_B}} \sum_{m'_{j_M}, m'_{j_B}} | \langle M'B' | T(E) | MB \rangle |^2 \quad (151)$$

with

$$\begin{aligned} & \langle M'B' | T(E) | MB \rangle = \\ & \langle j'_M m'_{j_M}, i'_M m'_{i_M}; j'_B m'_{j_B}, \tau'_B m'_{\tau_B} | T_{M'B', MB}(\vec{k}', \vec{k}, E) | j_M m_{j_M}, i_M m_{i_M}; j_B m_{j_B}, \tau_B m_{\tau_B} \rangle, \end{aligned} \quad (152)$$

where $[(j_M, m_{j_M}), (i_M, m_{i_M})]$ and $[(j_B m_{j_B}), (\tau_B m_{\tau_B})]$ are the spin-isospin quantum numbers of mesons and baryons, respectively. The incoming and outgoing momenta k and k' are defined by the collision energy E

$$E = E_M(k) + E_B(k) = E_{M'}(k') + E_{B'}(k'), \quad (153)$$

and the phase-space factor is

$$\rho_{MB}(k) = \pi \frac{k E_M(k) E_B(k)}{E}. \quad (154)$$

The partial-wave expansion of the scattering amplitude is defined as

$$T_{M'B', MB}(\vec{k}', \vec{k}, E) = \sum_{JM, TM_T} \sum_{LS, L'S'} | Y_{L'(j'_M j'_B)S'}^{JM, TM_T}(\hat{k}') \rangle T_{L'S'M'B', LSMB}^{JT}(k', k, E) \langle Y_{L(j_M j_B)S}^{JM, TM_T}(\hat{k}) | \quad (155)$$

where the total angular vector in the spin-isospin space is defined by

$$\begin{aligned} | Y_{L(j_M j_B)S}^{JM, TM_T}(\hat{k}) \rangle &= \sum_{all \ m} | j_M m_{j_M}, i_M, m_{i_M}; j_B m_{j_B}, \tau_B m_{\tau_B} \rangle \langle TM_T | i_M \tau_B m_{i_M} m_{\tau_B} \rangle \\ &\times \langle JM | LS m_L m_S \rangle \langle Sm_S | j_M j_B m_{j_M} m_{j_B} \rangle Y_{Lm_L}(\hat{k}). \end{aligned} \quad (156)$$

Clearly, Eqs.(155)-(156) lead to

$$\begin{aligned} & T_{L'S'M'B', LSMB}^{JT}(k', k, E) \\ &= \int d\hat{k}' \int d\hat{k} \langle Y_{L'(j'_M j'_B)S'}^{JM, TM_T}(\hat{k}') | T_{M'B', MB}(\vec{k}', \vec{k}; E) | Y_{L(j_M j_B)S}^{JM, TM_T}(\hat{k}) \rangle. \end{aligned} \quad (157)$$

By also expanding the driving term $V_{MB,M'B'}(\vec{k}, \vec{k}', E)$ of Eq. (135) into the partial-wave form similar to Eq.(155), we then obtain a set of coupled one-dimensional integral equations

$$\begin{aligned} t_{L'S'M'B',LSMB}^{JT}(k', k, E) &= V_{L'S'M'B',LSMB}^{JT}(k', k, E) \\ &+ \sum_{M''B''} \sum_{L''S''} \int k''^2 dk'' V_{L'S'M'B',L''S''M''B''}^{JT}(k', k'', E) \\ &\quad \times G_{M''B''}(k'', E) t_{L''S''M''B'',LSMB}^{JT}(k'', k, E), \end{aligned} \quad (158)$$

where the driving term is

$$V_{L'S'M'B',LSMB}^{JT}(k', k) = v_{L'S'M'B',LSMB}^{JT}(k', k) + Z_{L'S'M'B',LSMB}^{(E)JT}(k', k, E). \quad (159)$$

The above partial-wave matrix elements of the non-resonant interaction $v_{M'B',MB}$ and one-particle-exchange interaction $Z_{M'B',MB}^{(E)}(E)$ are given in Appendices C and E of Ref. [28], respectively. There the numerical methods for evaluating them are also discussed in some details; in particular on the use of the transformation from the helicity representation to the partial-wave representation.

The propagators in Eq.(158) are given by taking the matrix elements in Appendix B of Ref. [28] we have

$$G_{MB}(k, E) = \frac{1}{E - E_M(k) - E_B(k) + i\epsilon} \quad (160)$$

for stable particle channels $MB = \pi N, \eta N$, and

$$G_{MB}(k, E) = \frac{1}{E - E_M(k) - E_B(k) - \Sigma_{MB}(k, E)} \quad (161)$$

for unstable particle channels $MB = \pi\Delta, \rho N, \sigma N$ with

$$\Sigma_{\pi\Delta}(k, E) = \frac{m_\Delta}{E_\Delta(k)} \int q^2 dq \frac{M_{\pi N}(q)}{[M_{\pi N}^2(q) + k^2]^{1/2}} \frac{|f_{\Delta,\pi N}(q)|^2}{E - E_\pi(k) - [(E_N(q) + E_\pi(q))^2 + k^2]^{1/2} + i\epsilon}, \quad (162)$$

$$\Sigma_{\rho N}(k, E) = \frac{m_\rho}{E_\rho(k)} \int q^2 dq \frac{M_{\pi\pi}(q)}{[M_{\pi\pi}^2(q) + k^2]^{1/2}} \frac{|f_{\rho,\pi\pi}(q)|^2}{E - E_N(k) - [(2E_\pi(q))^2 + k^2]^{1/2} + i\epsilon}, \quad (163)$$

$$\Sigma_{\sigma N}(k, E) = \frac{m_\sigma}{E_\sigma(k)} \int q^2 dq \frac{M_{\pi\pi}(q)}{[M_{\pi\pi}^2(q) + k^2]^{1/2}} \frac{|f_{\sigma,\pi\pi}(q)|^2}{E - E_N(k) - [(2E_\pi(q))^2 + k^2]^{1/2} + i\epsilon}, \quad (164)$$

where the vertex function $f_{\Delta,\pi N}(q)$ is from Ref.[34], $f_{\rho,\pi\pi}(q)$ and $f_{\sigma,\pi\pi}(q)$ are from the isobar fits[48] to the $\pi\pi$ phase shifts. They are given in Appendix D of Ref. [28].

The solutions of Eq. (158) are then used to calculate the non-resonant photo-production amplitudes. Here we use the helicity-LSJ mixed-representation that the initial γN state is specified by their helicities, $\lambda_\gamma, \lambda_N$, but the final MB is defined by the $(LS)J$ angular momentum variables

$$v_{MB,\gamma N}(\vec{k}, \vec{q}) = \sum_{JM, TM_T} \sum_{LS} \sum_{\lambda_\gamma \lambda_N} | Y_{L(j_M j_B)S}^{JM, TM_T}(\hat{k}) > v_{LSMB, \lambda_\gamma \lambda_N m_{\tau_N}}^{JT}(k, q, E) \\ \times \sqrt{\frac{2J+1}{4\pi}} D_{M, (\lambda_\gamma - \lambda_N)}^J(\phi_q, \theta_q, -\phi_q) < \lambda_\gamma, \lambda_N m_{\tau_N} | , \quad (165)$$

where $D_{m,m'}^J(\phi, \theta, -\phi) = e^{i(m+m')\phi} d_{m,m'}^j(\theta)$ with $d_{m,m'}^j(\theta)$ being the Wigner rotation function. Eq. (135) then leads to

$$t_{LSMB, \lambda_\gamma \lambda_N m_{\tau_N}}^{JT}(k, q, E) = v_{LSMB, \lambda_\gamma \lambda_N m_{\tau_N}}^{JT}(k, q, E) + \sum_{M'B'} \sum_{L'S'} \int k'^2 dk' t_{LSMB, L'S' M'B'}^{JT}(k, k', E) \\ \times G_{M'B'}(k', E) v_{L'S' M'B', \lambda_\gamma \lambda_N m_{\tau_N}}^{JT}(k', q, E) . \quad (166)$$

The matrix elements $v_{LSMB, \lambda_\gamma \lambda_N m_{\tau_N}}^{JT}(k, q, E)$ considered in our calculations are given in Appendix F of Ref. [28]. This unconventional representation, which is convenient for calculations, can be related to the usual multipole expansion, as also given in appendix G of Ref. [28].

E. JLMS model of πN scattering

The parameters of the hadronic interactions of the dynamical model described in the above subsections are given in Ref. [29]. The parameters are first determined by fitting the empirical πN elastic scattering amplitudes of SAID up to 2 GeV. Then the resulting parameters are refined by directly comparing the predicted differential cross section and target polarization asymmetry with the original data of the elastic $\pi^\pm p \rightarrow \pi^\pm p$ and charge-exchange $\pi^- p \rightarrow \pi^0 n$ processes.

We solve the coupled-channel equations defined in the previous section in the partial-wave representation. The input of these equations are the partial-wave matrix elements of $\Gamma_{N^* \rightarrow MB}$ and $v_{MB, M'B'}$ of Eqs. (120)-(121), with $MB, M'B' = \pi N, \eta N, \pi \Delta, \rho N, \sigma N$, and $Z_{MB, M'B'}^{(E)}$ of Eq. (136) with $MB, M'B' = \pi \Delta, \rho N, \sigma N$. The calculations of these

matrix elements have been given explicitly in the appendices of Ref. [28]. Here we only mention a few points which are needed for later discussions.

In deriving the non-resonant interactions $v_{MB,M'B'}$ of Eq. (136) we consider the tree-diagrams (Fig. 10) generated from a set of Lagrangians with π , η , σ , ρ , ω , N , and Δ fields. The higher mass mesons, such as a_0 , a_1 included in other meson-exchange πN models, such as the Jülich model [52], are not considered. The employed Lagrangians are given in Appendix C.

To solve the coupled-channel equations, Eq. (135), we need to regularize the matrix elements of $v_{MB,M'B'}$, illustrated in Fig. 10. Here we follow Ref. [34] in order to use the parameters determined in the Δ (1232) region as the starting parameters in our fits. For the v^s and v^u terms of Fig. 10, we include at each meson-baryon-baryon vertex a form factor of the following form

$$F(\vec{k}, \Lambda) = [\vec{k}^2 / ((\vec{k}^2 + \Lambda^2)]^2 \quad (167)$$

with \vec{k} being the meson momentum. For the meson-meson-meson vertex of v^t of Fig. 10, the form Eq. (167) is also used with \vec{k} being the momentum of the exchanged meson. For the contact term v^c , we regularize it by $F(\vec{k}, \Lambda)F(\vec{k}', \Lambda')$.

With the non-resonant amplitudes generated from solving Eq. (135), the resonant amplitude $t_{MB,M'B'}^R$ Eq. (127) then depends on the bare mass $M_{N^*}^0$ and the bare $N^* \rightarrow MB$ vertex functions. As discussed in Ref. [28], these bare N^* parameters can be taken from a hadron structure calculation which does not include coupling with meson-baryon continuum states or meson-exchange quark interactions. We use the following parameterization,

$$\Gamma_{N^*,MB(LS)}(k) = \frac{1}{(2\pi)^{3/2}} \frac{1}{\sqrt{m_N}} C_{N^*,MB(LS)} \left[\frac{\Lambda_{N^*,MB(LS)}^2}{\Lambda_{N^*,MB(LS)}^2 + (k - k_R)^2} \right]^{(2+L/2)} \left[\frac{k}{m_\pi} \right]^L \quad (168)$$

where L and S are the orbital angular momentum and the total spin of the MB system, respectively. The above parameterization accounts for the threshold k^L dependence and the right power $(2 + L/2)$ such that the integration for calculating the dressed vertex Eq. (130)-(131) is finite.

The partial-wave quantum numbers for the considered channels are listed in Table I. The numerical methods for handling the moving singularities due to the $\pi\pi N$ cuts in $Z_{MB,M'B'}^{(E)}$ (Fig. 15) in solving Eq. (135) are explained in detail in Ref [28]. To get the πN

elastic scattering amplitudes, we can use either the method of contour rotation by solving the equations on the complex momentum axis $k = ke^{-i\theta}$ with $\theta > 0$ or the Spline-function method developed in Refs. [50, 51] and explained in detail in Ref. [28]. We perform the calculations using these two very different methods and they agree within less than 1%. When $Z_{MB,M'B'}^{(E)}$ is neglected, Eq. (135) can be solved by the standard subtraction method since the resonant propagators, Eqs. (132), for unstable particle channels $\pi\Delta$, ρN , and σN are free of singularity on the real momentum axis. A code for this simplified case has also been developed to confirm the results from using the other two methods.

The method of contour rotation becomes difficult at high E since the required rotation angle θ is very small. The Spline function method has no such limitation and we can perform calculations at $W > 1.9$ GeV without any difficulty. Typically, 24 and 32 mesh points are needed to get convergent solutions of the coupled-channel integral equation (135). Such mesh points are also needed to get stable integrations in evaluating the dressed resonance quantities Eqs. (129)-(131).

The parameters associated with $Z_{MB,M'B'}^{(E)}$ of Eq. (136) are completely determined from fitting the $\pi\pi$ phase shifts in Refs. [34] and [48]. Thus the considered model has the following parameters: (a) the coupling constants associated with the Lagrangians, (b) the cutoff Λ for each vertex of $v_{MB,M'B'}$ (Fig. 10), (c) the coupling strength $C_{N^*,MB(LS)}$ and range k_R and $\Lambda_{N^*,MB(LS)}$ of the bare $N^* \rightarrow MB$ vertex Eq. (168), and (d) the bare mass $M_{N^*}^0$ of each N^* state. We determine these by fitting the πN scattering data.

The fitting procedure is as follows. We first perform fits to the πN scattering data up to about 1.4 GeV and including only one bare state, the Δ (1232) resonance. In these fits, the starting coupling constant parameters of $v_{MB,M'B'}$ are taken from the previous studies of πN and NN scattering, which are also given in Ref. [28]. Except the πNN coupling constant $f_{\pi NN}$ all coupling constants and the cutoff parameters are allowed to vary in the χ^2 -fit to the πN data. The coupled-channel effects can shift the coupling constants greatly from their starting values. We try to minimize these shifts by allowing the cutoff parameters to vary in a very wide range 500 MeV $< \Lambda < 2000$ MeV. Some signs of coupling constants, which could not be fixed by the previous works [53], are also allowed to change. We then use the parameters from these fits at low energies as the starting ones to fit the amplitudes up to 2 GeV by also adjusting the resonance parameters, $M_{N^*}^0$,

		(LS) of the considered partial waves				
		πN	ηN	$\pi\Delta$	σN	ρN
S_{11}	$(0, \frac{1}{2})$	$(0, \frac{1}{2})$		$(2, \frac{3}{2})$	$(1, \frac{1}{2})$	$(0, \frac{1}{2}), (2, \frac{3}{2})$
S_{31}	$(0, \frac{1}{2})$	—		$(2, \frac{3}{2})$	—	$(0, \frac{1}{2}), (2, \frac{3}{2})$
P_{11}	$(1, \frac{1}{2})$	$(1, \frac{1}{2})$		$(1, \frac{3}{2})$	$(0, \frac{1}{2})$	$(1, \frac{1}{2}), (1, \frac{3}{2})$
P_{13}	$(1, \frac{1}{2})$	$(1, \frac{1}{2})$		$(1, \frac{3}{2}), (3, \frac{3}{2})$	$(2, \frac{1}{2})$	$(1, \frac{1}{2}), (1, \frac{3}{2}), (3, \frac{3}{2})$
P_{31}	$(1, \frac{1}{2})$	—		$(1, \frac{3}{2})$	—	$(1, \frac{1}{2}), (1, \frac{3}{2})$
P_{33}	$(1, \frac{1}{2})$	—		$(1, \frac{3}{2}), (3, \frac{3}{2})$	—	$(1, \frac{1}{2}), (1, \frac{3}{2}), (3, \frac{3}{2})$
D_{13}	$(2, \frac{1}{2})$	$(2, \frac{1}{2})$		$(0, \frac{3}{2}), (2, \frac{3}{2})$	$(1, \frac{1}{2})$	$(2, \frac{1}{2}), (0, \frac{3}{2}), (4, \frac{3}{2})$
D_{15}	$(2, \frac{1}{2})$	$(2, \frac{1}{2})$		$(2, \frac{3}{2}), (4, \frac{3}{2})$	$(3, \frac{1}{2})$	$(2, \frac{1}{2}), (2, \frac{3}{2}), (4, \frac{3}{2})$
D_{33}	$(2, \frac{1}{2})$	—		$(0, \frac{3}{2}), (2, \frac{3}{2})$	—	$(2, \frac{1}{2}), (0, \frac{3}{2}), (2, \frac{3}{2})$
D_{35}	$(2, \frac{1}{2})$	—		$(2, \frac{3}{2}), (4, \frac{3}{2})$	—	$(2, \frac{1}{2}), (2, \frac{3}{2}), (4, \frac{3}{2})$
F_{15}	$(3, \frac{1}{2})$	$(3, \frac{1}{2})$		$(1, \frac{3}{2}), (3, \frac{3}{2})$	$(2, \frac{1}{2})$	$(3, \frac{1}{2}), (1, \frac{3}{2}), (3, \frac{3}{2})$
F_{17}	$(3, \frac{1}{2})$	$(3, \frac{1}{2})$		$(3, \frac{3}{2}), (5, \frac{3}{2})$	$(4, \frac{1}{2})$	$(3, \frac{1}{2}), (3, \frac{3}{2}), (5, \frac{1}{2})$
F_{35}	$(3, \frac{1}{2})$	—		$(1, \frac{3}{2}), (3, \frac{3}{2})$	—	$(3, \frac{1}{2}), (1, \frac{3}{2}), (3, \frac{3}{2})$
F_{37}	$(3, \frac{1}{2})$	—		$(3, \frac{3}{2}), (5, \frac{3}{2})$	—	$(3, \frac{1}{2}), (3, \frac{3}{2}), (5, \frac{3}{2})$

TABLE I: The orbital angular momentum (L) and total spin (S) of the partial waves included in solving the coupled channel Equation (135).

$C_{N^*, MB(LS)}$, k_R and $\Lambda_{N^*, MB(LS)}$. Here we need to specify the number of bare N^* states in each partial wave. The simplest approach is to assume that each of 3-star and 4-star resonances listed by the Particle Data Group [24] is generated from a bare N^* state of the model Hamiltonian Eq. (117). However, this choice is perhaps not well justified since the situation of the higher mass N^* 's is not so clear.

We thus start the fits including only the bare states which generate the lowest and well-established N^* resonance in each partial wave. The second higher mass bare state is then included when a good fit can not be achieved. We also impose the condition that if the resulting $M_{N^*}^0$ is too high > 2.5 GeV, we remove such a bare state in the fit. This is due to the consideration that the interactions due to such a heavy bare N^* state could be just the separable representation of some non-resonant mechanisms which should be

included in $v_{MB,M'B'}$. In some partial waves the quality of the fits is not very sensitive to the N^* couplings to $\pi\Delta$, ρN , and σN . But the freedom of varying these coupling parameters is needed to achieve good fits.

It is rather difficult to fit all partial waves simultaneously because the number of resonance parameters to be determined is very large. We proceed as follows. We first fit only 3 or 4 partial waves which have well established resonant states, and whose amplitudes have an involved energy dependence. These are the S_{11} , P_{11} , S_{31} and P_{33} partial waves. These fits are aimed at identifying the possible ranges of the parameters associated with $v_{MB,M'B'}$. We then gradually extend the fits to include more partial waves. For some cases, the fits can be reached easily by simply adjusting the bare N^* parameters. But it often requires some adjustments of the non-resonant parameters to obtain new fits. This procedure has to be repeated many times to explore the parameter space as much as we can. We use the fitting code MINUIT and the parallel computation facilities at NERSC in US and the Barcelona Supercomputing Center in Spain.

The most uncertain part of the fitting is to handle the large number of parameters associated with the bare N^* states. Here the use of the empirical partial-wave amplitudes from SAID is an essential step in the fit. It allows us to locate the ranges of the N^* parameters partial-wave by partial-wave for a given set of the parameters for the non-resonant $v_{MB,M'B'}$. Even with this, the information is far from complete for pinning down the N^* parameters. Perhaps the N^* parameters associated with the πN state are reasonably well determined in this fit to the πN scattering data. The parameters associated with ηN , $\pi\Delta$, ρN and σN can only be better determined by also fitting to the data of $\pi N \rightarrow \eta N$ and $\pi N \rightarrow \pi\pi N$ reactions. This will be pursued in our future calculations.

It is useful to note here that the leading-order effect due to $Z^{(E)}$ of the meson-baryon interaction Eq. (136) on πN elastic scattering is

$$\delta v_{\pi N, \pi N} = \sum_{MB, M'B' = \pi\Delta, \rho N, \sigma N} v_{\pi N, MB} G_{MB}(E) Z_{MB, M'B'}^{(E)} G_{M'B'}(E) v_{M'B', \pi N}. \quad (169)$$

We have found by explicit numerical calculations that $\delta v_{\pi N, \pi N}$ is much weaker than $v_{\pi N, \pi N}$ and hence the coupled channel effects due to $Z_{MB, M'B'}^{(E)}$ on πN elastic scattering amplitude are weak. One example obtained from our model is shown in Table II. Thus we first perform the fits without including $Z^{(E)}$ term to speed up the computation. We

then refine the parameters by including this term in the fits.

	$\text{Re}[t_{\pi N, \pi N}]$	$\text{Re}[t_{\pi N, \pi N}(Z^{(E)} = 0)]$	$\text{Im}[t_{\pi N, \pi N}]$	$\text{Im}[t_{\pi N, \pi N}(Z^{(E)} = 0)]$
S_{11}	-0.00481	-0.00557	0.0841	0.0827
P_{11}	0.0937	0.103	0.636	0.640
P_{13}	0.169	0.181	0.275	0.275
D_{13}	0.202	0.194	0.299	0.309
D_{15}	0.117	0.116	0.0179	0.0179
F_{15}	0.290	0.291	0.157	0.155
F_{17}	0.0360	0.0359	0.00293	0.00289
S_{31}	-0.433	-0.437	0.496	0.504
P_{31}	-0.253	-0.230	0.434	0.448
P_{33}	0.0506	0.0306	0.510	0.457
D_{33}	-0.00504	-0.0135	0.106	0.104
D_{35}	0.0551	0.0551	0.0540	0.0537
F_{35}	-0.0214	-0.0229	0.0259	0.0283
F_{37}	0.0625	0.0626	0.00502	0.00512

TABLE II: The effect of $Z_{MB, M'B'}^{(E)}$ on the πN scattering amplitudes $t_{\pi N, \pi N}$ from solving Eq. (135) at $E = 1.7$ GeV. The normalization is $t_{\pi N, \pi N} = (e^{2i\delta_{\pi N}} - 1)/(2i)$, where $\delta_{\pi N}$ is the πN scattering phase shift which could be complex at energies above the π production threshold.

We first locate the range of the parameters by fitting the empirical πN scattering amplitude of SAID [20]. We then check and refine the resulting parameters by directly comparing our predictions with the original πN scattering data.

Our fits to the empirical amplitudes of SAID [20] are given in Figs. 19-20 and Figs. 21-22 for the $T = 1/2$ and $T = 3/2$ partial waves, respectively. The resulting parameters are presented in Appendix D. The parameters associated with the non-resonant interactions, $v_{MB, M'B'}$ with $MB, M'B' = \pi N, \eta N, \pi\Delta, \rho N, \sigma N$, are given in Table IX for the coupling constants of the starting Lagrangian and Table X for the cutoffs of the form factors defined by Eq. (167). The resulting bare N^* parameters are listed in Tables XI-XIII

From Figs. 19-22, one can see that the empirical πN amplitudes can be fitted very

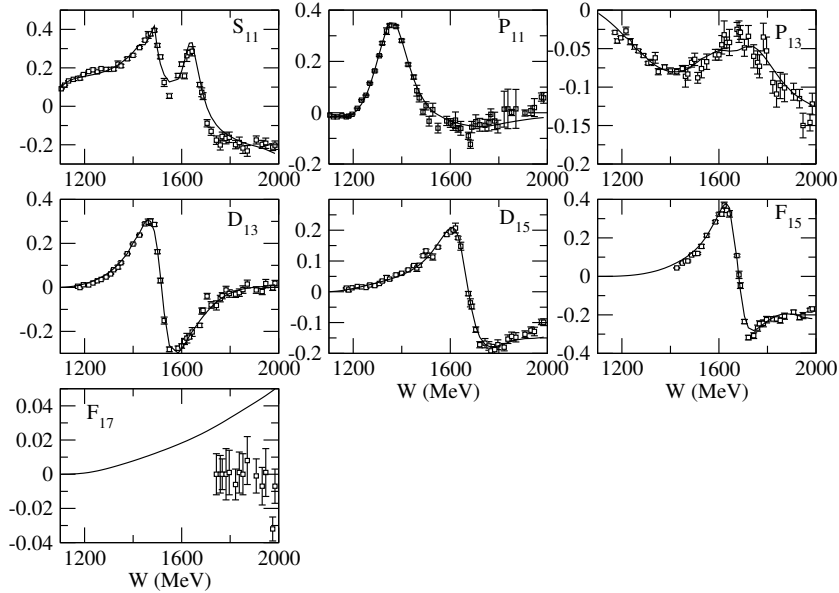


FIG. 19: Real parts of the calculated πN partial wave amplitudes (Eq. (126)) of isospin $T = 1/2$ are compared with the energy independent solutions of Ref. [20].

well. The most significant discrepancies are in the imaginary part of S_{31} in Fig.22. The agreement is also poor for the F_{17} in Fig.19-20 and D_{35} in Figs.21-22, but there are rather large errors in the data. Our parameters are therefore checked by directly comparing our predictions with the data of differential cross sections $d\sigma/d\Omega$ and target polarization asymmetry P of elastic $\pi^\pm p \rightarrow \pi^\pm p$ and charge-exchange $\pi^- p \rightarrow \pi^0 n$ processes. Our results (solid red curves) are shown in Figs.23-27. Clearly, our model is rather consistent with the available data, and are close to the results (dashed blue curves) calculated from the SAID's amplitudes. Thus our model is justified despite the differences with the SAID's amplitudes seen in Fig.19-22.

It will be important to further refine our parameters by fitting the data of other πN scattering observables, such as the recoil polarization and double polarization. Hopefully, such data can be obtained from the new hadron facilities at JPARC in Japan.

Our model is further checked by examining our predictions of the total cross sections σ^{tot} which can be calculated from the forward elastic scattering amplitudes by using the optical theorem. The total elastic scattering cross sections σ^{el} can be calculated from the

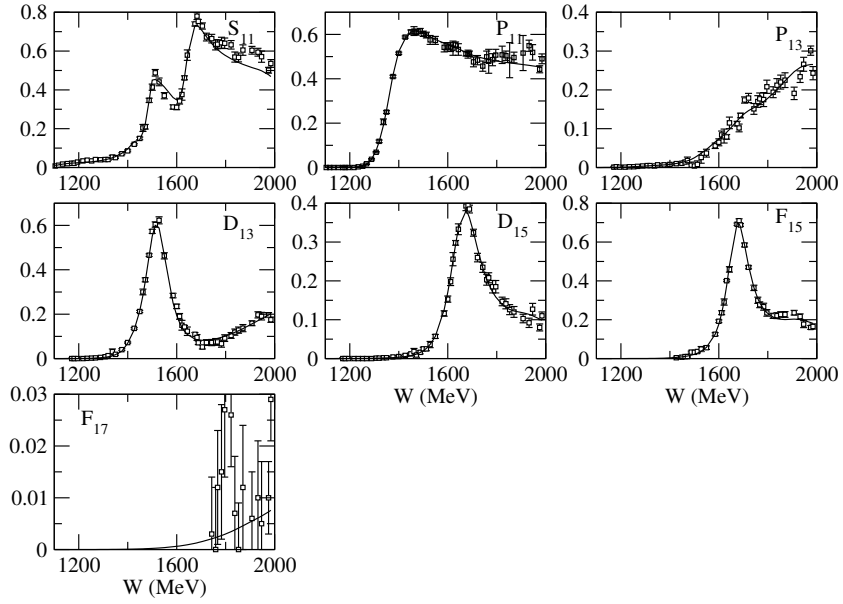


FIG. 20: Imaginary parts of the calculated πN partial wave amplitudes (Eq. (126)) of isospin $T = 1/2$ are compared with the energy independent solutions of Ref. [20].

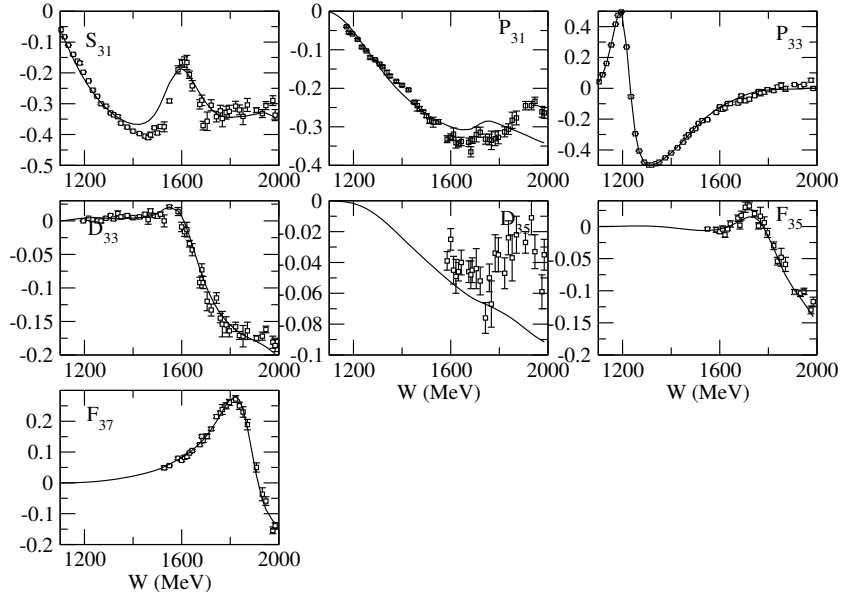


FIG. 21: Real parts of the calculated πN partial wave amplitudes (Eq. (126)) of isospin $T = 3/2$ are compared with the energy independent solutions of Ref. [20].

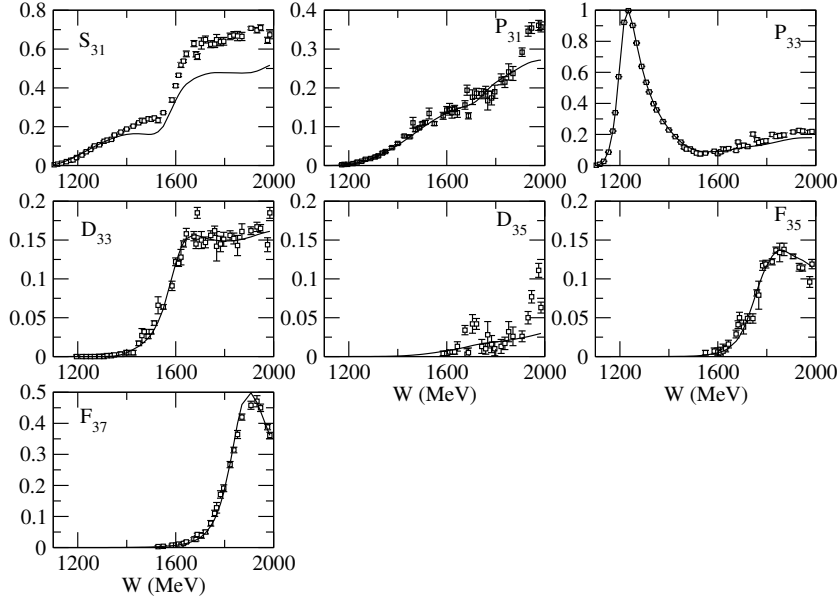


FIG. 22: Imaginary parts of the calculated πN partial wave amplitudes (Eq. (126)) of isospin $T = 3/2$ are compared with the energy independent solutions of Ref. [20].

predicted partial wave amplitudes. With the normalization $\langle \vec{k} | \vec{k}' \rangle = \delta(\vec{k} - \vec{k}')$ used in Ref. [28], we have

$$\sigma_T^{el}(E) = \sum_{T=1/2,3/2} \sigma_T^{el}(E) \quad (170)$$

with

$$\sigma_T^{el}(E) = \frac{(4\pi)^2}{k^2} \rho_{\pi N}(E) \sum_{JLS} \frac{(2J+1)}{2} |T_{L'S'(\pi N), LS(\pi N)}^{TJ}(k, k, E)|^2, \quad (171)$$

where $\rho_{\pi N}(E) = \pi k E_\pi(k) E_N(k)/E$ with k determined by $E = E_\pi(k) + E_N(k)$ and the amplitude $T_{L'S'(\pi N), LS(\pi N)}^{TJ}(k, k; E)$ is the partial-wave solution of Eq. (126). Similarly, the total $\pi N \rightarrow \eta N$ cross sections can be calculated from

$$\sigma_{\pi N \rightarrow \eta N}^{tot} = \frac{(4\pi)^2}{k^2} \rho_{\pi N}^{1/2}(E) \rho_{\eta N}^{1/2}(E) \sum_{JLS} \frac{(2J+1)}{2} |T_{\eta N(LS), \pi N(LS)}^{T=1/2, J}(k', k, E)|^2 \quad (172)$$

where $\rho_{\eta N}(E) = \pi k' E_\eta(k') E_N(k')/E$ with k' determined by $E = E_\eta(k') + E_N(k')$. We can also calculate the contribution from each of the unstable channels, $\pi\Delta$, ρN , and σN , to the total $\pi N \rightarrow \pi\pi N$ cross sections. For example, we have for the $\pi N \rightarrow \pi\Delta \rightarrow \pi\pi N$

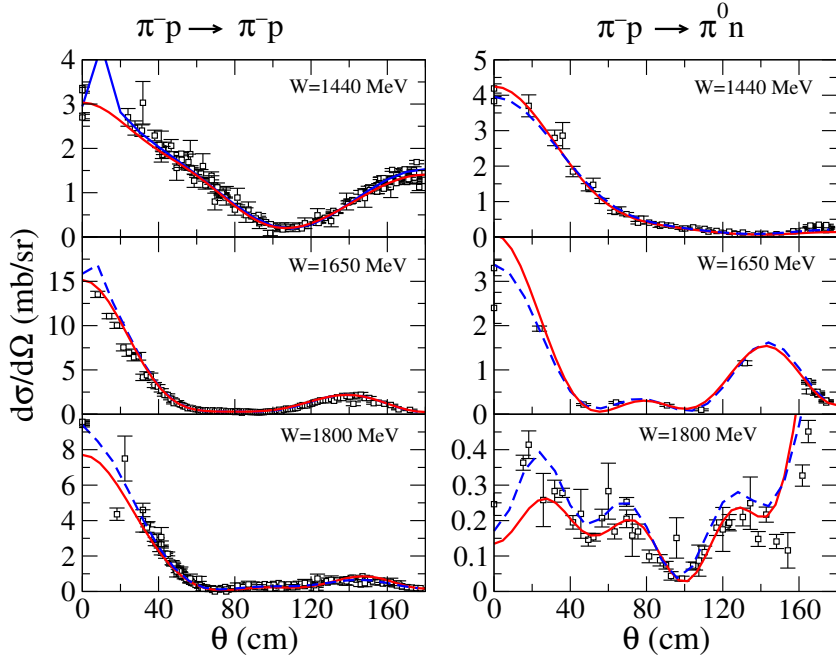


FIG. 23: Differential cross section for several different center of mass energies. Solid red curve corresponds to our model while blue dashed lines correspond to the SP06 solution of SAID [20]. All data have been obtained through the SAID online applications. Ref. [20].

contribution in the center of mass frame

$$\sigma_{\pi\Delta}^{rec}(E) = \int_{m_N+m_\pi}^{E-m_\pi} dM_{\pi N} \frac{M_{\pi N}}{E_\Delta(k)} \frac{\Gamma_{\pi\Delta}(k, E)/(2\pi)}{|E - E_\pi(k) - E_\Delta(k) - \Sigma_{\pi\Delta}(k, E)|^2} \sigma_{\pi N \rightarrow \pi\Delta}(k, E) \quad (173)$$

where k is defined by $M_{\pi N} = E_\pi(k) + E_N(k)$, $E_{\pi N}(k) = [M_{\pi N}^2 + k^2]^{1/2}$, $\Sigma_{\pi\Delta}(k, E)$ is defined in Eq.(162), $\Gamma_{\pi\Delta}(k, E) = -2Im(\Sigma_{\pi\Delta}(k, E))$, and

$$\sigma_{\pi N \rightarrow \pi\Delta}(k, E) = 4\pi \rho_{\pi N}(k_0) \rho_{\pi\Delta}(k) \sum_{L'S', LS, J} \frac{2J+1}{(2S_N+1)(2S_\pi+1)} |T_{\pi\Delta(L'S'), \pi N(LS)}^J(k, k_0; E)|^2 \quad (174)$$

where k_0 is defined by $E = E_\pi(k_0) + E_N(k_0)$ and $\rho_{ab}(k) = \pi k E_a(k) E_b(k)/E$. The amplitude $T_{L'S'(\pi\Delta), LS(\pi N)}^J(k, k_0; E)$ is the partial-wave solution of Eq.(126). The corresponding expressions for the unstable channels ρN and σN can be obtained from Eqs. (173)-(174) by changing the channel labels.

The predicted σ^{tot} (solid curves) along with the resulting total elastic scattering cross sections σ^{el} compared with the data of π^+p reaction are shown in Fig. 28. Clearly, the

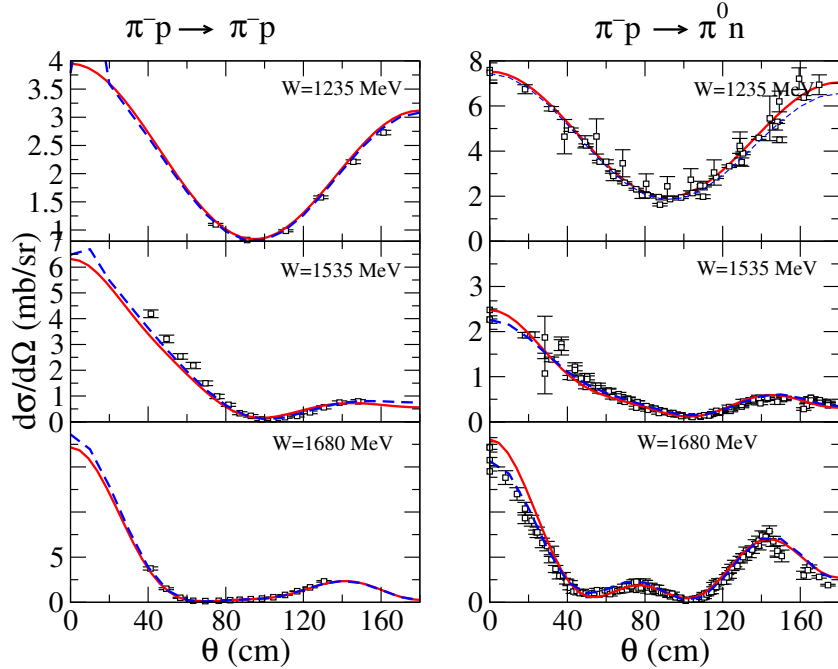


FIG. 24: Differential cross section for several different center of mass energies. Similar description as Fig. 23. All data have been obtained through the SAID online applications. Ref. [20].

model can account for the data very well within the experimental errors. Here only the $T = 3/2$ partial waves are relevant. Equally good agreement with the data for π^-p reaction are shown in the left side of Fig. 29. In the right side, we show how the contributions from each channel add up to get the total cross sections. The comparison of the contribution from ηN channel with the data is shown in Fig. 30. It is possible to improve the fit to this data by adjusting $N^* \rightarrow \eta N$ parameters. But this can be done correctly only when the differential cross section data of $\pi N \rightarrow \eta N$ are included in the fit.

The contributions from $\pi\Delta$, ρN and σN intermediate states to the $\pi^-p \rightarrow \pi\pi N$ total cross sections calculated from our model can be seen in the right side of Fig. 29. These predictions remain to be verified by the future experiments. The existing $\pi N \rightarrow \pi\pi N$ data are not sufficient for extracting model independently the contributions from each unstable channel.

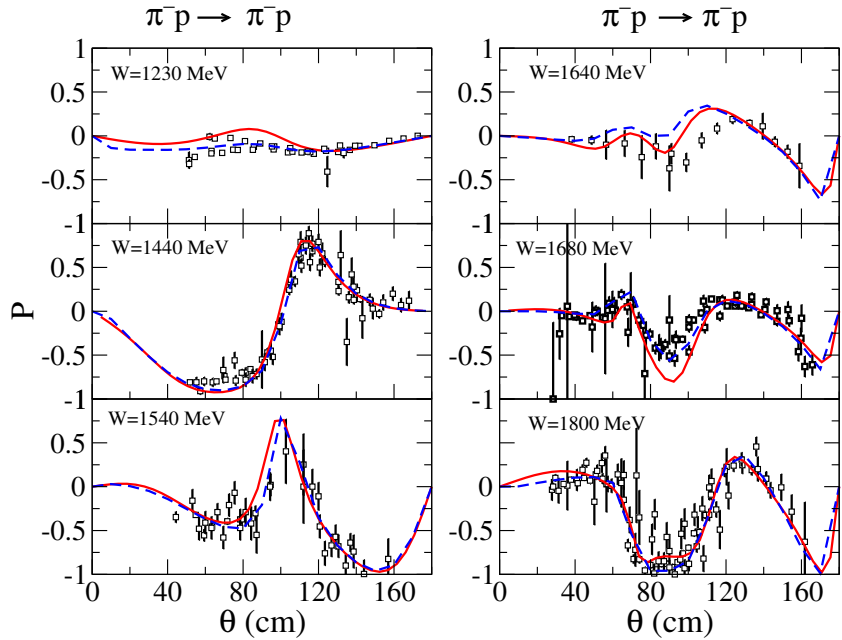


FIG. 25: Target polarization asymmetry, P , for several different center of mass energies. Similar description as Fig. 23. All data have been obtained through the SAID online applications. Ref. [20].

The results shown in Figs. 28-30 indicate that our parameters are consistent with the total cross section data.

F. Pion electroproduction

We perform a dynamical coupled-channel analysis of $p(e, e'\pi)N$ data in the region of $E \leq 1.6$ GeV and $Q^2 \leq 1.45$ (GeV/c) 2 . This model is an extension of the analysis [30] of pion photoproduction reactions. With the hadronic parameters of the employed dynamical coupled-channels model determined in analyzing the πN reaction data [29, 55], the only freedom in analyzing the electromagnetic meson production reactions is the electromagnetic coupling parameters of the model. If the parameters listed in Ref. [28] are used to calculate the non-resonant interaction, the only parameters to be determined from the data of pion electroproduction reactions are the bare $\gamma^* N \rightarrow N^*$ helicity amplitudes for the lowest N^* states in P_{33} , P_{11} , S_{11} and D_{13} partial waves. Such a highly constrained

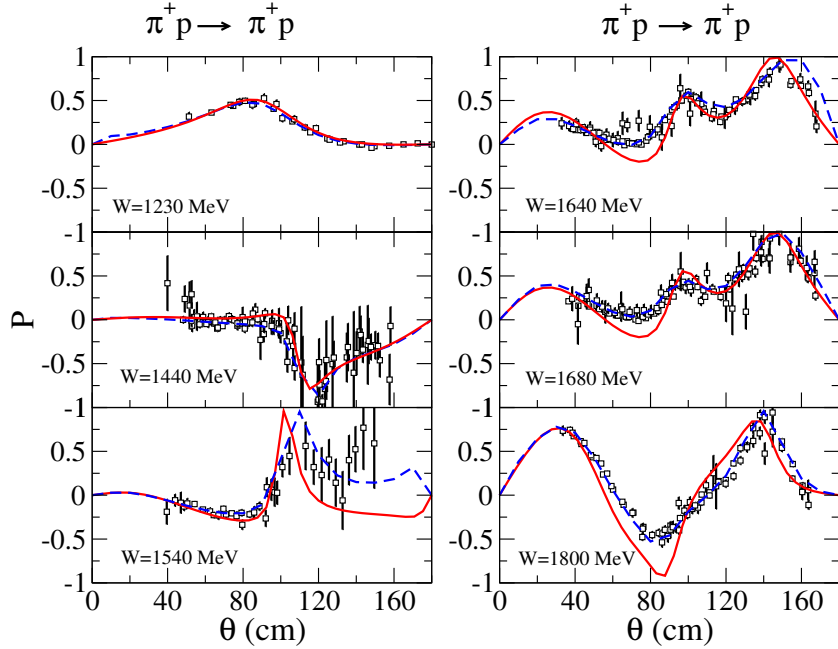


FIG. 26: Target polarization asymmetry, P , for several different center of mass energies. Description as in Fig. 23. All data have been obtained through the SAID online applications. Ref. [20].

analysis was performed in Ref. [30] for pion photoproduction. It was found that the available data of $\gamma p \rightarrow \pi^0 p$, $\pi^+ n$ can be fitted reasonably well up to invariant mass $E \leq 1.6$ GeV. In this work we extend this effort to analyze the pion electroproduction data in the same E region.

The resonant amplitude is given by replacing initial meson-baryon state in Eq. (127) with $\gamma^* N$,

$$t_{LS_N\pi N, \lambda_\gamma \lambda_N}^{R,J}(k, q, E, Q^2) = \sum_{N_i^*, N_j^*} [\bar{\Gamma}_{N_i^*, LS_N\pi N}^J(k, E)]^* D_{i,j}(E) \bar{\Gamma}_{N_j^*, \lambda_\gamma \lambda_N}^J(q, E, Q^2), \quad (175)$$

where $S_N = 1/2$ is the nucleon spin, $E = \omega + E_N(q)$ is the invariant mass of the $\gamma^* N$ system. The dressed $N^* \rightarrow \pi N$ vertex $\bar{\Gamma}_{N_i^*, LS_N\pi N}^J(k, E)$ and N^* propagator $D_{i,j}(E)$ have been determined and given explicitly in Ref. [30]. The dressed $\gamma^* N \rightarrow N^*$ vertex function is

$$\bar{\Gamma}_{N^*, \lambda_\gamma \lambda_N}^J(q, E, Q^2) = \Gamma_{N^*, \lambda_\gamma \lambda_N}^J(q, Q^2)$$

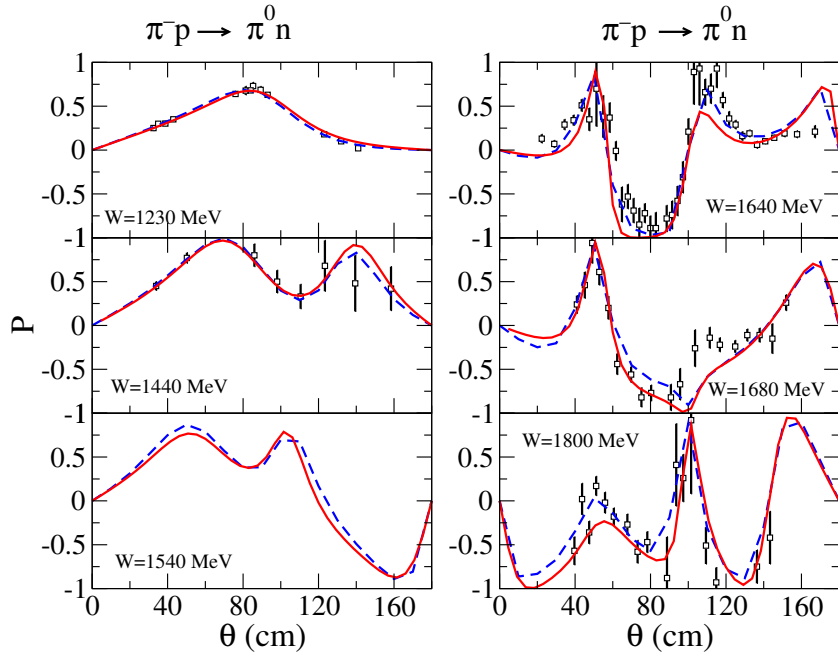


FIG. 27: Target polarization asymmetry, P , for several different center of mass energies. Description as in Fig. 23. All data have been obtained through the SAID online applications. Ref. [20].

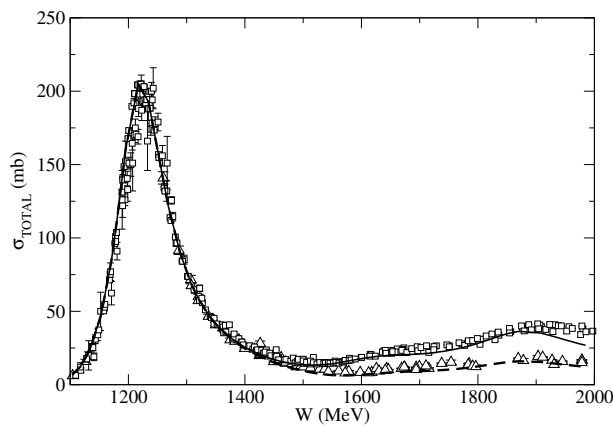


FIG. 28: The predicted total cross sections of the $\pi^+ p \rightarrow X$ (solid curve) and $\pi^+ p \rightarrow \pi^+ p$ (dashed curve) reactions are compared with the data. Squares and triangles are the corresponding data from Ref. [24].

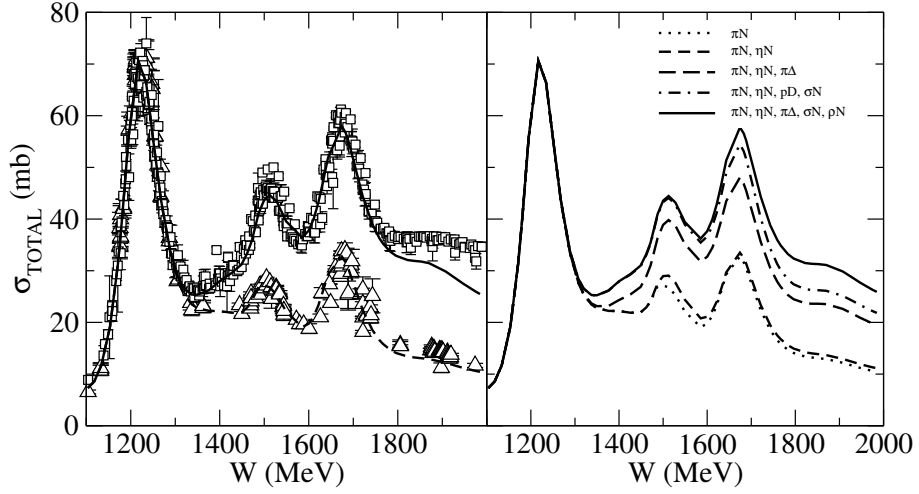


FIG. 29: Left: The predicted total cross sections of the $\pi^- p \rightarrow X$ (solid curve) and $\pi^- p \rightarrow \pi^- p + \pi^0 n$ (dashed curve) reactions are compared with the data. Open squares are the data on $\pi^- p \rightarrow X$ from Ref. [24], open triangles are obtained by adding the $\pi^- p \rightarrow \pi^- p$ and $\pi^- p \rightarrow \pi^0 n$ data obtained from Ref. [24] and SAID database [54] respectively. Right: Show how the predicted contributions from each channel are added up to the predicted total cross sections of the $\pi^- p \rightarrow X$.

$$+ \sum_{M'B'} \sum_{L'S'} \int k'^2 dk' \bar{\Gamma}_{N^*, L'S'M'B'}^J(k', E) G_{M'B'}(k', E) v_{L'S'M'B', \lambda_\gamma \lambda_N}^J(k', q, Q^2). \quad (176)$$

We define the bare $\gamma^* N \rightarrow N^*$ vertex functions $\Gamma_{N^*, \lambda_\gamma \lambda_N}^J(q, Q^2)$ of Eq. (176). We parameterize these functions as

$$\Gamma_{N^*, \lambda_\gamma \lambda_N}^J(q, Q^2) = \frac{1}{(2\pi)^{3/2}} \sqrt{\frac{m_N}{E_N(q)}} \sqrt{\frac{q_R}{|q_0|}} G_\lambda(N^*, Q^2) \delta_{\lambda, (\lambda_\gamma - \lambda_N)}, \quad (177)$$

where q_R and q_0 are defined by $M_{N^*} = q_R + E_N(q_R)$ with N^* mass and $E = q_0 + E_N(q_0)$, respectively, and

$$G_\lambda(N^*, Q^2) = A_\lambda(N^*, Q^2), \quad \text{for transverse photon,} \quad (178)$$

$$= S_\lambda(N^*, Q^2), \quad \text{for longitudinal photon.} \quad (179)$$

We also cast the helicity amplitudes of the dressed vertex Eq. (176) into the form of

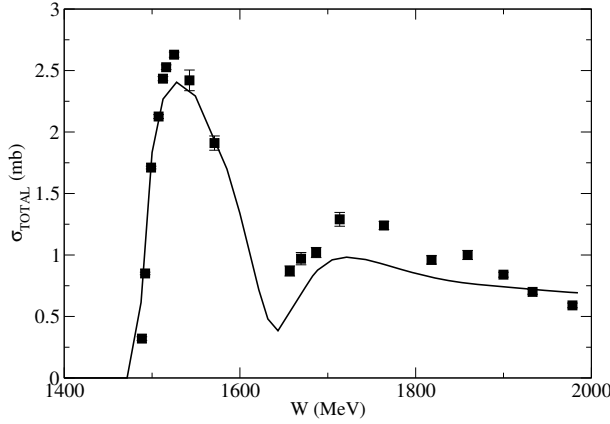


FIG. 30: The predicted total cross sections of $\pi p \rightarrow \eta p$ reaction are compared with the data [74, 75].

Eq. (177) with dressed helicity amplitudes

$$\bar{A}_\lambda(N^*, Q^2) = A_\lambda(N^*, Q^2) + A_\lambda^{\text{m.c.}}(N^*, Q^2), \quad (180)$$

$$\bar{S}_\lambda(N^*, Q^2) = S_\lambda(N^*, Q^2) + S_\lambda^{\text{m.c.}}(N^*, Q^2), \quad (181)$$

where $A_\lambda^{\text{m.c.}}(N^*, Q^2)$ and $S_\lambda^{\text{m.c.}}(N^*, Q^2)$ are due to the meson cloud effect defined by the second term of Eq. (176). Here we emphasize these helicity amplitudes are defined at the real mass of N^* in order to discuss the difference between bare amplitudes and dressed amplitudes due to the shift by meson cloud effects. Helicity amplitudes in terms of the residue of resonance poles on complex energy plane will be given and discussed in Section V.

We first try to fix the bare helicity amplitudes by fitting to the data of $\sigma_T + \epsilon\sigma_L$, σ_{LT} , and σ_{TT} of $p(e, e'\pi^0)p$ in Ref.[56] which covers almost all (E, Q^2) region we are considering (see Table.III). The formula for calculating σ_α from the amplitudes are given in Ref. [44]. In a purely phenomenological approach, we first vary all of the helicity amplitudes of 16 bare N^* states, considered in analyzing the $\pi N \rightarrow \pi N, \pi\pi N$ data [29, 55], in the fits to the data. It turns out that only the helicity amplitudes of the first N^* states in S_{11} , P_{11} , P_{33} and D_{13} are relevant in the considered $E \leq 1.6$ GeV. Thus in this paper only the bare helicity amplitudes associated with those four bare N^* states (total 10 parameters) are varied in the fit and other bare helicity amplitudes are set to zero. The numerical fit

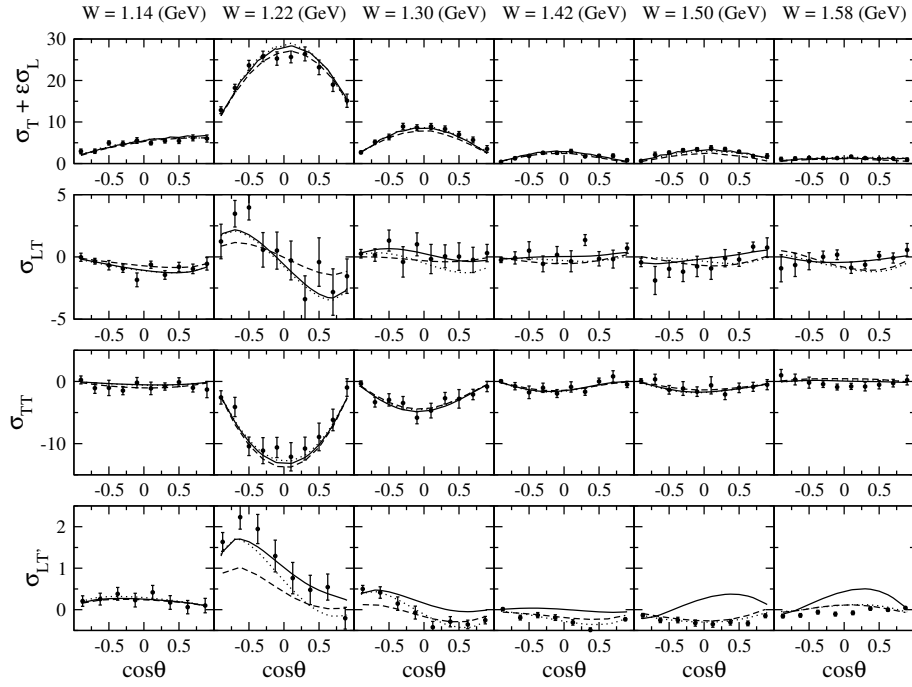


FIG. 31: Fit to $p(e, e'\pi^0)p$ structure functions at $Q^2 = 0.4$ (GeV/c) 2 . Here $\theta \equiv \theta_\pi^*$. The solid curves are the results of Fit1, the dashed curves are of Fit2, and the dotted curves are of Fit3. (See text for the description of each fit.) The data are taken from Refs. [56, 59].

is performed at each Q^2 independently, using the MINUIT library.

The results of the fits are the solid curves in the top three rows of Figs. 31-33. Clearly our results from this fit agree with the data well. We obtain similar quality of fits to the data of Ref. [56] at other Q^2 values listed in Table. III. We have also used the magnetic $M1$ form factor of $\gamma^*N \rightarrow \Delta(1232)$ extracted from previous analyses as data for fitting. The results are shown in Fig. 34. We refer the results of this fit to as ‘‘Fit1’’.

In Fig. 35, we present the G_M^* , G_E^* , and G_C^* form factors of $\gamma^*N \rightarrow \Delta(1232)$ transition obtained from Fit1 (solid points). In the same figure, we also show the meson cloud effect in the form factors. Within our model, it has a significant contribution at low Q^2 , but rapidly decreases as Q^2 increases, particularly for G_E^* and G_C^* . These results are similar to the previous findings [45, 57].

The helicity amplitudes of S_{11} , P_{11} , and D_{13} resulting from Fit1 are shown in Fig. 36. The solid circles are the absolute magnitude of the dressed helicity amplitudes (180) and (181). The errors there are assigned by MIGRAD in the MINUIT library. More

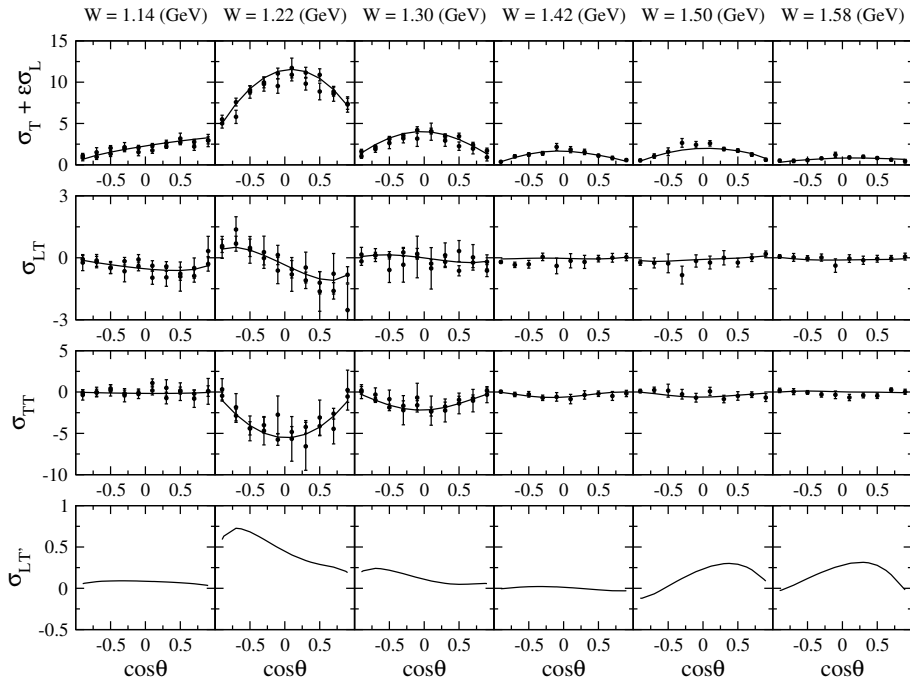


FIG. 32: Fit to $p(e, e'\pi^0)p$ structure functions at $Q^2 = 0.9$ $(\text{GeV}/c)^2$. Here $\theta \equiv \theta_\pi^*$. The data are taken from Ref. [56].

detailed analysis of the errors is perhaps needed, but will not be addressed here. The meson cloud effect (dashed curves), as defined by $A_\lambda^{\text{m.c.}}$ and $S_\lambda^{\text{m.c.}}$ of Eqs. (180) and (181) and calculated from the second term of Eq. (176), are the necessary consequence of the unitarity conditions. They do not include the bare helicity term determined here and are already fixed in the photoproduction analysis [30]. Within our model (and within Fit1), the meson cloud contribution is relatively small in S_{11} and $A_{1/2}$ of D_{13} even in the low Q^2 region.

Here we note that our helicity amplitudes defined in Eqs. (180) and (181) are different from the commonly used convention, say A_λ^{cnv} and S_λ^{cnv} , which are obtained from the imaginary part of the $\gamma^*N \rightarrow \pi N$ multipole amplitudes [58]. This definition leads to helicity amplitudes which are real, while our dressed amplitudes are complex. It was shown in Ref. [45] that for the $\Delta(1232)$ resonance our dressed helicity amplitudes (180) and (181) can be reduced to A_λ^{cnv} and S_λ^{cnv} , if we replace the Green function $G_{\pi N}$ with its principal value in all loop integrals appearing in the calculation. However, such reduction is not so trivial for higher resonance states because the unstable $\pi\Delta, \rho N, \sigma N$ channels open, and thus the direct comparison of the helicity amplitudes from other analyses

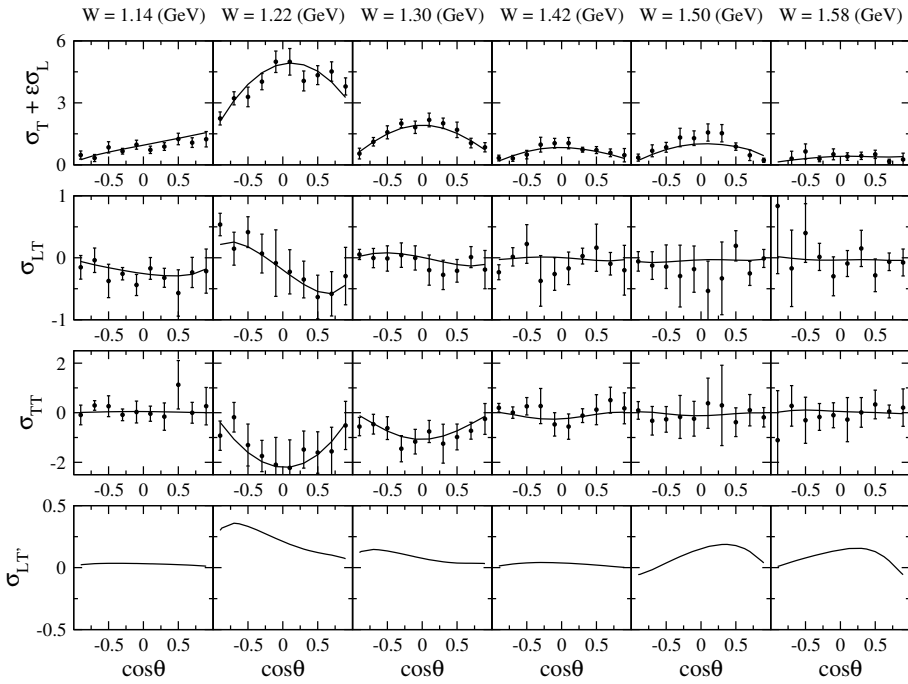


FIG. 33: Fit to $p(e, e'\pi^0)p$ structure functions at $Q^2 = 1.45$ (GeV/c) 2 . Here $\theta \equiv \theta_\pi^*$. The data are taken from Ref. [56].

becomes unclear. We will again discuss the complex helicity amplitudes in terms of resonance poles and residues in Section V.

At $Q^2 = 0.4$ (GeV/c) 2 , the data of all structure functions both for $p(e, e'\pi^0)p$ and $p(e, e'\pi^+)n$ are available as seen in Table. III. To see the sensitivity of the resulting helicity amplitudes to the amount of the data included in the fits, we further carry out two fits at this Q^2 , referred to as Fit2 and Fit3, respectively. Fit2 (Fit3) further includes the data of Refs. [59–61] (Ref. [59]) in the fit in addition to those of Ref. [56] which are used in Fit1. This means that Fit2 includes all available data both from $p(e, e'\pi^0)p$ and $p(e, e'\pi^+)n$, whereas Fit3 includes the same data but from $p(e, e'\pi^0)p$ only. The results of each fit are the dashed and dotted curves in Fig. 31 for $p(e, e'\pi^0)p$ and Fig. 37 for $p(e, e'\pi^+)n$, respectively.

The resulting bare helicity amplitudes are listed in the third (Fit2) and fourth (Fit3) columns of Table II and compare with that from Fit1. The corresponding change in the $\gamma N \rightarrow \Delta(1232)$ form factors and the dressed helicity amplitudes are also shown as open circles and triangles in Figs. 35 and 36. A significant change among the three different fits is observed in most of the results except G_M^* in P_{33} . This indicates that fitting the

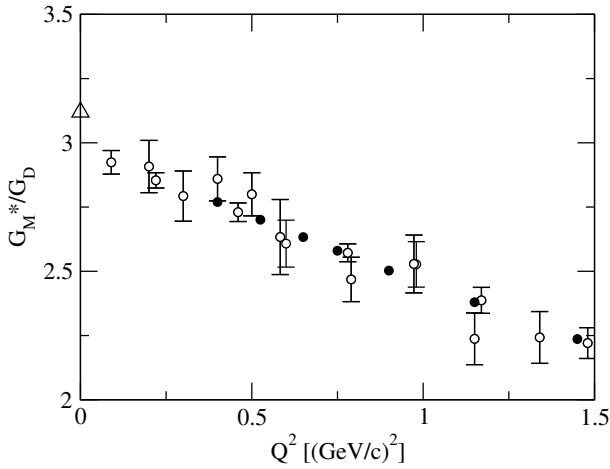


FIG. 34: G_M^* normalized by the dipole factor $G_D = [1 + Q^2/0.71(\text{GeV}/c)^2]^{-2}$. The solid black circles at $Q^2 > 0$ are our fit to the values extracted from previous analyses (those values are taken from Ref. [30]). The triangle at $Q^2 = 0$ is from our photoproduction analysis [30].

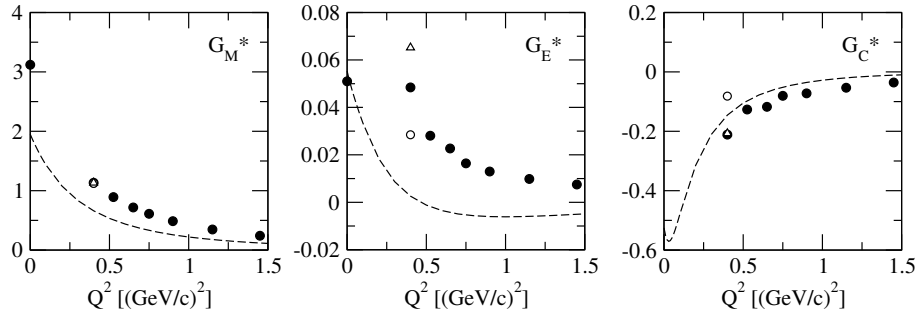


FIG. 35: The $\gamma^* N \rightarrow \Delta(1232)$ form factors. Solid points are from Fit1; dashed curves are the meson cloud contribution. Open circles and triangles at $Q^2 = 0.4 (\text{GeV}/c)^2$ are from Fit2 and Fit3, respectively. The three points are almost overlapped in G_M^* . The solid point at $Q^2 = 0$ is obtained from the photoproduction reaction analysis in Ref. [30].

data listed in Table III are far from sufficient to pin down the $\gamma^* N \rightarrow N^*$ transition form factors up to $Q^2 = 1.45 (\text{GeV}/c)^2$. It clearly indicates the importance of obtaining data from complete or over-complete measurements of most, if not all, of the independent $p(e, e'\pi)N$ polarization observables. Such measurements were made by Kelly et al. [62] in the $\Delta(1232)$ region and will be performed at JLab for wide ranges of E and Q^2 in the next few years [5].

It has been seen in Fig. 37 that all of our current fits underestimate σ_T of $p(e, e'\pi^+)n$ at

Q^2 (GeV/c) 2	$\gamma^* p \rightarrow \pi^0 p$	$\gamma^* p \rightarrow \pi^+ n$
0.3	—	$\sigma_T + \epsilon\sigma_L, \sigma_{LT}, \sigma_{TT}$ [60]
0.4	$\sigma_T + \epsilon\sigma_L, \sigma_{LT}, \sigma_{TT}$ [56]; $\sigma_{LT'}$ [59]	$\sigma_T + \epsilon\sigma_L, \sigma_{LT}, \sigma_{TT}$ [60]; $\sigma_{LT'}$ [61]
0.5	—	$\sigma_T + \epsilon\sigma_L, \sigma_{LT}, \sigma_{TT}$ [60] ^a
0.525	$\sigma_T + \epsilon\sigma_L, \sigma_{LT}, \sigma_{TT}$ [56]	—
0.6	—	$\sigma_T + \epsilon\sigma_L, \sigma_{LT}, \sigma_{TT}$ [60] ^b
0.65	$\sigma_T + \epsilon\sigma_L, \sigma_{LT}, \sigma_{TT}$ [56]; $\sigma_{LT'}$ [59]	$\sigma_{LT'}$ [61]
0.75	$\sigma_T + \epsilon\sigma_L, \sigma_{LT}, \sigma_{TT}$ [56]	—
0.9	$\sigma_T + \epsilon\sigma_L, \sigma_{LT}, \sigma_{TT}$ [56]	—
1.15	$\sigma_T + \epsilon\sigma_L, \sigma_{LT}, \sigma_{TT}$ [56]	—
1.45	$\sigma_T + \epsilon\sigma_L, \sigma_{LT}, \sigma_{TT}$ [56]	—

^aThe data are available up to $E = 1.51$ GeV

^bThe data are available up to $E = 1.41$ GeV

TABLE III: Available structure function data at $Q^2 \leq 1.45$ (GeV/c) 2 .

	Fit1	Fit2	Fit3
	(Ref. [56] data)	(Refs. [56, 59–61] data)	(Refs. [56, 59] data)
$S_{11} A_{1/2}$	100.80 ± 1.46	83.25 ± 1.21	48.29 ± 5.46
$S_{11} S_{1/2}$	-119.30 ± 20.41	-9.85 ± 1.69	-53.53 ± 4.75
$P_{11} A_{1/2}$	33.18 ± 2.11	-15.68 ± 1.00	20.17 ± 10.37
$P_{11} S_{1/2}$	37.29 ± 2.26	52.23 ± 3.16	131.00 ± 5.87
$P_{33} A_{3/2}$	-146.00 ± 0.60	-137.50 ± 0.56	-150.80 ± 1.03
$P_{33} A_{1/2}$	-54.47 ± 0.61	-62.57 ± 0.69	-46.29 ± 1.73
$P_{33} S_{1/2}$	7.85 ± 1.25	-7.66 ± 1.22	7.34 ± 1.69
$D_{13} A_{3/2}$	-44.01 ± 1.31	-67.01 ± 1.99	-98.63 ± 2.92
$D_{13} A_{1/2}$	97.11 ± 8.51	14.34 ± 1.26	70.02 ± 4.83
$D_{13} S_{1/2}$	-18.35 ± 1.37	19.43 ± 1.45	4.11 ± 2.76

TABLE IV: Ambiguity of resulting bare helicity amplitudes [the results are at $Q^2 = 0.4$ (GeV/c) 2]. The errors are assigned by MIGRAD in the MINUIT library.

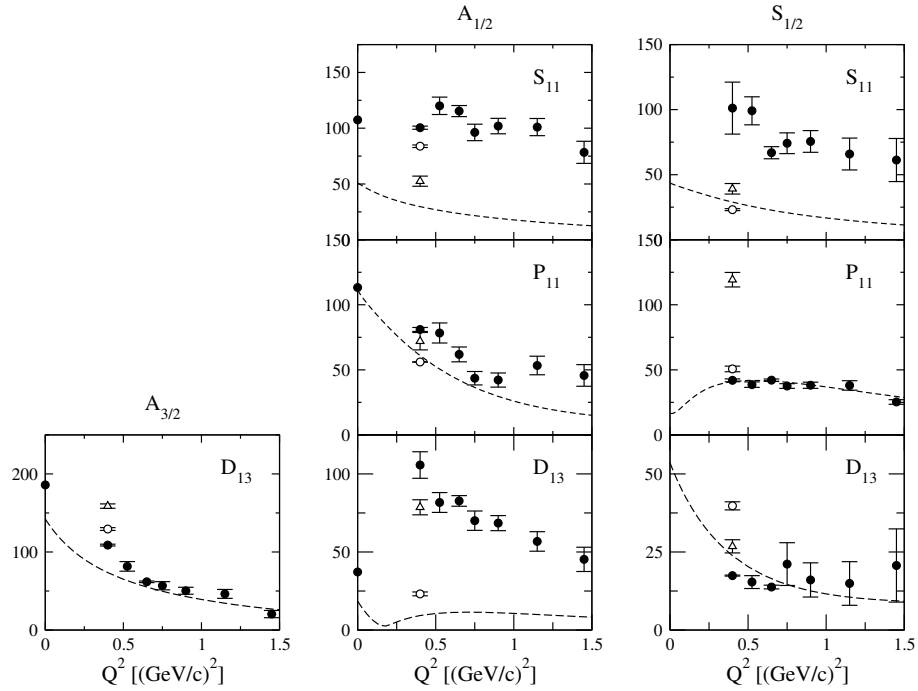


FIG. 36: Extracted helicity amplitudes for S_{11} at $E = 1535$ MeV (upper panels), P_{11} at $E = 1440$ MeV (middle panels), and D_{13} at $E = 1520$ MeV (lower panels). The meaning of each point and curve is same as in Fig. 35.

forward angles. We find that this can be improved by further varying the S_{31} and P_{13} bare helicity amplitudes within their reasonable range. In Fig. 38, the results with the nonzero S_{31} and P_{13} bare helicity amplitudes (solid curves) are compared with the results without varying those amplitudes (dashed curves). The resulting values of the bare helicity amplitudes are $(A_{1/2}^{S_{31}}, S_{1/2}^{S_{31}}) = (121.6, 59.6)$ and $(A_{3/2}^{P_{13}}, A_{1/2}^{P_{13}}, S_{1/2}^{P_{13}}) = (-73.2, -42.9, 41.5)$. The parameters of Fit2 are used for S_{11} , P_{11} , P_{33} , and D_{13} in both curves. In the figure we have just shown the results at $E \sim 1.3$ GeV. We confirm that the same consequence is obtained also at other E , and find that the P_{13} (S_{31}) has contributions mainly at low (high) E . We also find that the inclusion of the bare S_{31} and P_{13} helicity amplitudes does not change other structure functions than σ_T of $p(e, e'\pi^+)n$ (at most, most of the change is within the error). This indicates that those two helicity amplitudes are rather relevant to $p(e, e'\pi^+)n$, but not to $p(e, e'\pi^0)p$. As shown in Table III, however, no enough data is currently available for $p(e, e'\pi^+)n$ above $Q^2 = 0.4$ $(\text{GeV}/c)^2$. The data both of the $p(e, e'\pi^0)p$ and $p(e, e'\pi^+)n$ at same Q^2 values are desirable to pin down the Q^2 dependence

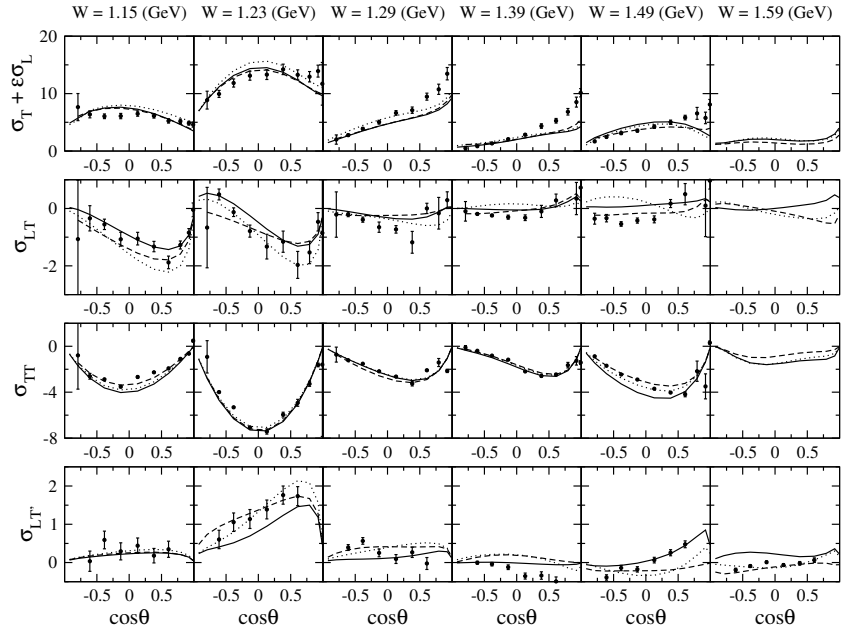


FIG. 37: Structure functions of $p(e, e'\pi^+)n$ at $Q^2 = 0.4$ (GeV/c) 2 . Here $\theta \equiv \theta_{\pi}^*$. The solid curves are the results of Fit1, the dashed curves are of Fit2, and the dotted curves are of Fit3. (See text for the description of each fit.) As for the $\sigma_{LT'}$, results at $E = 1.14, 1.22, 1.3, 1.38, 1.5, 1.58$ GeV (from left to right of the bottom row) are shown, in which the data are available. The data in the figure are taken from Ref. [60, 61].

of the S_{31} and P_{13} helicity amplitudes.

We now turn to show the coupled-channels effect. In Fig. 39, we see that when only the πN intermediate state is kept in the $M'B'$ summation of the non-resonant amplitude [Eq. (135)] and the dressed $\gamma^* N \rightarrow N^*$ vertices [Eq. (176)], the predicted total transverse and longitudinal cross sections σ_T and σ_L of $p(e, e'\pi^0)p$ are changed from the solid to dashed curves. This corresponds to only examining the coupled-channels effect on the electromagnetic (Q^2 -dependent) part in the $\gamma^* N \rightarrow \pi N$ amplitude. All coupled-channels effects on the non-electromagnetic interactions are kept in the calculations. We find that the coupled-channels effect tends to decrease when Q^2 increases. This is rather clearly seen in σ_T . In particular, the coupled-channels effect on σ_T at high $E \sim 1.5$ GeV is small (10-20%) already at $Q^2 = 0.4$ (GeV/c) 2 . (The effect is about 30-40% at $Q^2 = 0$ [30].) This is understood as follows. In Eq. (175) we can further split the resonant amplitude t^R as $t^R = t_{\text{bare}}^R + t_{\text{m.c.}}^R$, where t_{bare}^R and $t_{\text{m.c.}}^R$ are the same as t^R but replacing

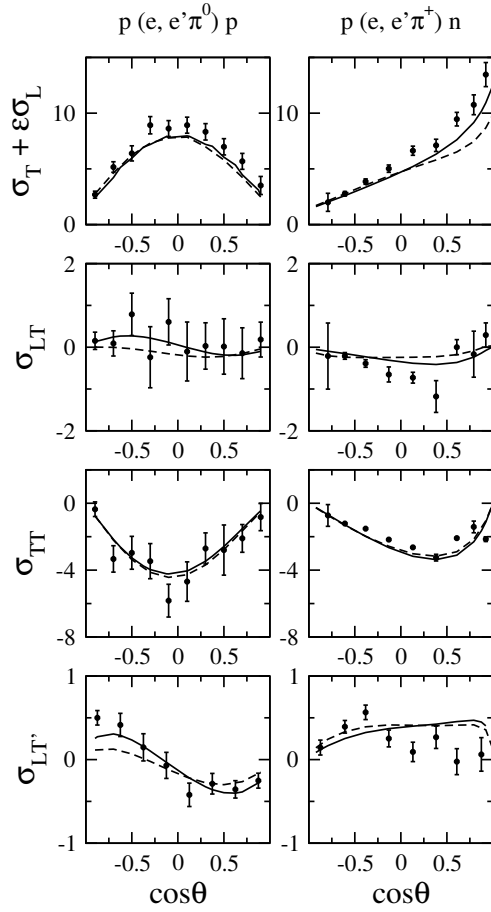


FIG. 38: Contribution of the S_{31} and P_{13} helicity amplitudes at $Q^2 = 0.4$ (GeV/c) 2 . The left (right) panels are the structure functions of $p(e, e'\pi^0)p$ [$p(e, e'\pi^+)n$] reaction at $E = 1.3$ GeV ($E = 1.29$ GeV). Solid (dashed) curves are the results with (without) nonzero S_{31} and P_{13} bare helicity amplitudes. The parameters of Fit2 are used for the S_{11} , P_{11} , P_{33} , and D_{13} helicity amplitudes in both curves. The data are from Refs. [56, 59–61].

$\bar{\Gamma}_{N^*, \lambda_\gamma \lambda_N}^J$ with its bare part $\Gamma_{N^*, \lambda_\gamma \lambda_N}^J$ and meson cloud part [the second term of Eq. (176)], respectively. The coupled-channels effect shown in Fig. 39 comes from $t_{LS_N \pi N, \lambda_\gamma \lambda_N}^J$ and $t_{m.c.}^R$. We have found that the relative importance of the coupled-channels effect in each part remains the same for increasing Q^2 . However, the contribution of non-resonant mechanisms both on $t_{LS_N \pi N, \lambda_\gamma \lambda_N}^J$ and $t_{m.c.}^R$ to the structure functions decreases for higher Q^2 compared with t_{bare}^R . This explains the smaller coupled-channels effect compared with the photoproduction reactions [30]. The decreasing non-resonant interaction at higher Q^2 is due to its long range nature, thus indicating that higher Q^2 reactions provide a

clearer probe of N^* . We obtain similar results also for $p(e, e'\pi^+)n$.

It is noted, however, that the above argument does not mean coupled-channels effect is negligible in the full $\gamma^*N \rightarrow \pi N$ reaction process. In the above analysis we kept the coupled-channels effect on the hadronic non-resonant amplitudes, the strong N^* vertices, and the N^* self-energy, which are Q^2 -independent and remain important irrespective of Q^2 . We have found in the previous analyses [29, 55] that the coupled-channels effect on them is significant in all energy region up to $E = 2$ GeV.

In Fig. 40, we show the coupled-channels effect on the five-fold differential cross section. The coupled-channels effects are significant at low E , whereas they are small at high E . This is consistent with the above discussions because the five-fold differential cross sections are dominated by σ_T . Here we also see that our full results (solid curves) are in good agreement with the original data, although we performed the fits by using the structure function data listed in Table III.

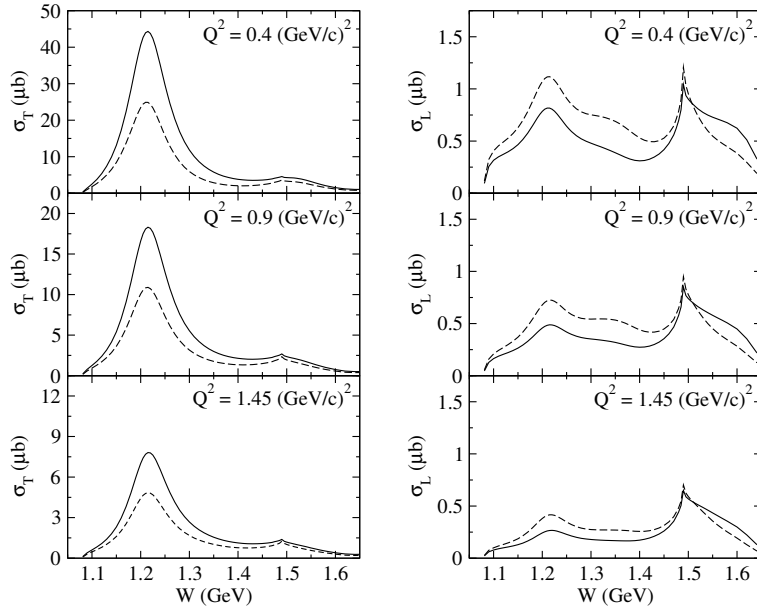


FIG. 39: Coupled-channels effect on the integrated structure functions $\sigma_T(E)$ and $\sigma_L(E)$ for $Q^2 = 0.4, 0.9, 1.45$ $(\text{GeV}/c)^2$ for $p(e, e'\pi^0)p$ reactions. The solid curves are the full results calculated with the bare helicity amplitudes of Fit1. The dashed curves are the same as solid curves but only the πN loop is taken in the $M'B'$ summation in Eqs. (135) and (176).

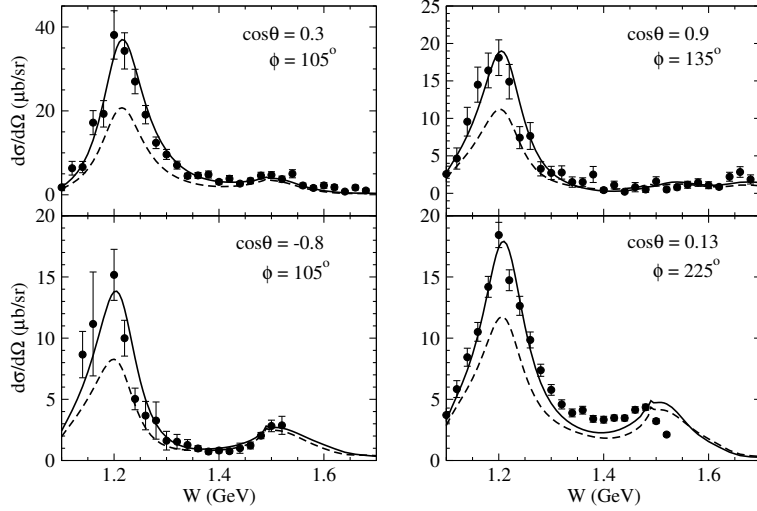


FIG. 40: Coupled-channels effect on the five-fold differential cross sections $\Gamma_\gamma^{-1}[d\sigma/(dE_{e'}d\Omega_{e'}d\Omega_\pi^*)]$ of $p(e, e'\pi^0)p$ (upper panels) and $p(e, e'\pi^+)n$ (lower panels) at $Q^2 = 0.4$ (GeV/c) 2 . Here $\theta \equiv \theta_\pi^*$ and $\phi \equiv \phi_\pi^*$. The solid curves are the full results calculated with the bare helicity amplitudes of Fit1. The dashed curves are the same as the solid curves but only the πN loop is taken in the $M'B'$ summation in Eqs. (135) and (176). The data are taken from Ref. [63]

V. RESULTS AND DISCUSSIONS

A. Analytic continuation and pole positions

To extract the information of resonance poles from the dynamical coupled channel model described in Section IV, it is necessary to choose the proper integral path for analytic continuation. We need to choose the contours C_{MB} and C_3 appropriately to solve the coupled channel problem for E on various possible unphysical sheets of the Riemann surface as described in Section II. This requires careful examinations of the locations of the on-shell momentum of each propagator $G_{MB}(k, E)$ and the $\pi\pi N$ cut in the self energies, such as $\Sigma_{\pi\Delta}(k, E)$ of Eq. (162), of the unstable particle channels.

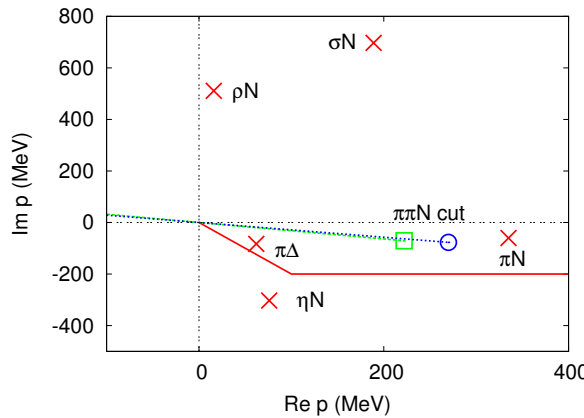


FIG. 41: Singularities and integral path on the complex momentum plane at $E = 1357 - 76i$ MeV. Red crosses are singularities of meson-baryon propagator given by Eqs. (182) and (183). Green line and square (blue line and circle) are $\pi\pi N$ cut and a branch point for the selfenergy of $\pi\Delta$ by Eq. (185) (σN and ρN by Eq. (185)). Red line shows an integral path.

Here we present one example, the case for a pole on P_{11} partial wave amplitude which corresponds to $N^*(1440)$. In Fig. 41, the singularities of meson-baryon propagator on complex momentum plane at $E = 1357 - 76i$ MeV, that turns out to be the pole position on complex energy plane as a result of the pole search, are shown by red crosses. Each singularity of meson-baryon propagator is obtained by solving

$$E - E_M(p) - E_B(p) = 0, \quad (182)$$

for stable particle channels $MB = \pi N, \eta N$, and

$$E - E_M(p) - E_B(p) - \Sigma_{MB}(p, E) = 0, \quad (183)$$

for unstable particle channels $MB = \pi\Delta, \rho N, \sigma N$. The left-hand side of these two equations are the denominator of propagator $G_{MB}(p, E)$ given by Eq. (160) and (161). The branch point of $\pi\pi N$ cut in the self energy $\Sigma_{\pi\Delta}$, $\Sigma_{\sigma N}$ and $\Sigma_{\rho N}$ are given as

$$E = E_\pi(p_0) + [(m_\pi + m_N)^2 + p_0^2]^{1/2} \quad \text{for } \pi\Delta, \quad (184)$$

$$E = E_N(p_0) + [(2m_\pi)^2 + p_0^2]^{1/2} \quad \text{for } \rho N \text{ and } \sigma N, \quad (185)$$

and they are shown in Fig. 41 by green line and square for $\pi\Delta$ and by blue line and circle for ρN and σN . Actually, the singularities for each meson-baryon channel are on the different momentum plane and we can choose a different integral path for each channel independently, which means we can choose a different Riemann sheet of each channel. Here, for simplicity, we illustrate all singularities on the single complex plane and take the same path for every channel in Fig. 41, where the path is shown by red line. The real part of the considered energy is 1357 MeV, that is above the threshold energies for πN and $\pi\pi N$, and below that for ηN , σN and ρN . So the unphysical sheet for πN and $\pi\pi N$ is the nearest sheet from the physical region and we choose the path below the singularities of πN and $\pi\pi N$ for analytic continuation to the unphysical sheet of them. On the other hand, the physical sheet for ηN , σN and ρN is the nearest sheet from the physical region and we take the path above the singularity of ηN . Singularities of σN and ρN are on the upper half of complex momentum plane, which means we look at the physical sheet for such channels by the considered path. We choose the unphysical sheet of $\pi\Delta$ in Fig. 41, though the both of unphysical and physical sheets for $\pi\Delta$ are close to the physical region because the $\pi\Delta$ threshold is just close to 1357 MeV. Thus we can calculate the amplitude at the complex energy $E = 1357 - 76i$ MeV.

We search for poles of the total amplitudes from finding the zeros of the determinant of $D^{-1}(E)$ defined by Eq. (128). Here we use the well-established Newton iteration method in Appendix A. We have performed searches in the $(m_\pi + m_N) \leq \text{Re}(E) \leq 2000$ MeV and $-\text{Im}(E) \leq 350$ MeV region within which PDG's 3- and 4-stars resonances are listed. Poles with very large widths are more difficult to locate precisely with our numerical methods and hence will not be discussed here. In Table V, the extracted resonance poles positions

	$M_{N^*}^0$ (MeV)	M_R (MeV)	Location	PDG (MeV)
S_{11}	1800	(1540, 191)	(<i>uuuupp</i>)	(1490 - 1530, 45 - 125)
	1880	(1642, 41)	(<i>uuuupp</i>)	(1640 - 1670, 75 - 90)
P_{11}	1763	(1357, 76)	(<i>upuupp</i>)	(1350 - 1380, 80 - 110)
	1763	(1364, 105)	(<i>upuppp</i>)	
	1763	(1820, 248)	(<i>uuuuup</i>)	(1670 - 1770, 40 - 190)
	2037	(1999, 321)	(<i>uuuuuu</i>)	
P_{13}	1711	—		(1660 - 1690, 57 - 138)
D_{13}	1899	(1521, 58)	(<i>uuuupp</i>)	(1505 - 1515, 52 - 60)
D_{15}	1898	(1654, 77)	(<i>uuuupp</i>)	(1655 - 1665, 62 - 75)
F_{15}	2187	(1674, 53)	(<i>uuuupp</i>)	(1665 - 1680, 55 - 68)
S_{31}	1850	(1563, 95)	(<i>u-uup-</i>)	(1590 - 1610, 57 - 60)
P_{31}	1900	—		(1830 - 1880, 100 - 250)
P_{33}	1391	(1211, 50)	(<i>u-ppp-</i>)	(1209 - 1211, 49 - 51)
	1600	—		(1500 - 1700, 200 - 400)
D_{33}	1976	(1604, 106)	(<i>u-uup-</i>)	(1620 - 1680, 80 - 120)
F_{35}	2162	(1738, 110)	(<i>u-uuu-</i>)	(1825 - 1835, 132 - 150)
	2162	(1928, 165)	(<i>u-uuu-</i>)	
F_{37}	2138	(1858, 100)	(<i>u-uuu-</i>)	(1870 - 1890, 110 - 130)

TABLE V: The resonance pole positions M_R [listed as $(\text{Re } M_R, -\text{Im } M_R)$] extracted from the dynamical model in the different unphysical sheets are compared with the values of 3- and 4-stars nucleon resonances listed in the PDG [24]. “—” for $P_{33}(1600)$, P_{13} and P_{31} indicates that no resonance pole has been found in the considered complex energy region, $\text{Re}(E) \leq 2000$ MeV and $-\text{Im}(E) \leq 350$ MeV.

(M_R) are compared with the bare N^* masses ($M_{N^*}^0$) of our model and the 3- and 4-star values listed by PDG [24]. Like the previous works [64, 67], we only look for poles which are close to the physical region and have effects on πN scattering observables. All of these poles are on the unphysical sheet of the πN channel, but could be on either unphysical

(u) or physical (p) sheets of other channels considered in this analysis. We will indicate the sheets where the identified poles are located by $(s_{\pi N}, s_{\eta N}, s_{\pi\pi N}, s_{\pi\Delta}, s_{\rho N}, s_{\sigma N})$, where s_{MB} and $s_{\pi\pi N}$ can be u or p or $-$ denoting no coupling to this channel. Let us remark that the only physical sheet is the $(pppppp)$. On that sheet the full amplitude should be analytic except for a bound state pole and a unitary cut. Any other sheet is unphysical.

With the exception of the $P_{33}(1600)$, P_{13} and P_{31} cases, all pole positions listed by the PDG are consistent with our results. One possible reason for not finding these poles is that their imaginary part may be beyond the $-\text{Im}(M_R) \leq 350$ MeV region where our analytic continuation method is accurate and is covered in our searches. Another possibility is that these resonances, if indeed exist, are perhaps due to the mechanisms which are beyond our model, but are particularly sensitive to these partial waves. The P_{11} pole at $1999 - 321i$ MeV has no corresponding resonance on the PDG. The imaginary part of this pole is so large that we might hardly compare it with the analysis of experimental results.

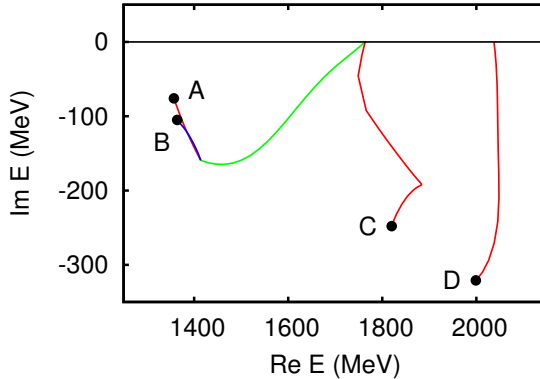


FIG. 42: Trajectories of the evolution of P_{11} resonance poles A (1357, -76), B (1364, -105), C (1820, -248) and D(1999, -321) from a bare N^* with 1763 MeV and 2037 MeV, as the couplings of the bare N^* with the meson-baryon reaction channels are varied from zero to the full strengths of our model.

For P_{11} channel we find four poles below 2 GeV. Two of them near 1360 MeV are close to the $\pi\Delta$ threshold. This finding is consistent with the earlier analysis of VPI[26] and Cutkosky and Wang[27], and the recent analysis by the GWU/VPI[67] and Juelich[68]

Analysis	P_{11} poles (MeV)
This work (JLMS model)	(1357, -76) (1364, -105)
GWU/VPI [67]	(1359, -82) (1388, -83)
Jülich model [68]	(1387, -74) (1387, -71)

TABLE VI: P_{11} resonance poles extracted from three different approaches and near the Roper resonance position of PDG are compared.

groups as seen in Table VI. We find that they are on different sheets: (1357, -76) and (1346, -105) are on the unphysical and physical sheet of the $\pi\Delta$ channel, respectively.

Within our model, we can further study the dynamical origin of these two nearby poles around the $\pi\Delta$ threshold. The way the identified resonance poles evolve dynamically from their bare masses (listed in Table V) through their coupling with reaction channels can be examined by tracing the zeros of $\det[D^{-1}(E)] = \det[E - M_{N^*}^0 - \sum_{MB} y_{MB} M_{MB}(E)]$ in the region $0 \leq y_{MB} \leq 1$, where $M_{MB}(E)$ is the contribution of channel MB to the self energy defined by Eq. (128). Each y_{MB} is varied independently to find continuous evolution paths through the various Riemann sheets on which our analytic continuation method is valid.

For the P_{11} case we found the three poles are associated to one bare state as shown in Fig. 42. The poles A(1357, -76), B(1364, -105) and C(1820, -248) evolve from the same bare state with a mass of 1763 MeV. The pole D(1999, -321) corresponds to the other bare state with a mass of 2037 MeV. The poles A and B are on the physical sheet of the ηN channel and their difference occurs due to the choice of the sheet for $\pi\Delta$ channel. The green curve indicates how the bare state evolves through varying all coupling strengths except keeping $y_{\pi\Delta} = 0$, to about $Re(M_R) \sim 1400$ MeV. By further varying $y_{\pi\Delta}$ to 1 of the full model, it then splits into two trajectories; one moves to pole A on the unphysical sheet and the other to B on the physical sheet of $\pi\Delta$ channel. Our finding suggests that the number of resonance poles found from the analysis of pion-nucleon scattering amplitudes does not necessarily correspond to the number of the 'bare' states. The dynamical coupled channel induces multi-poles from a single bare state. Although a cusp-like move may be seen in the trajectory to the pole C, it is not actually a cusp but a differentiable curve. It is due to the influence of the upper resonance D.

Next, we apply the procedure for extracting residues of resonance poles developed in Section III by presenting the results for P_{33} , D_{13} and P_{11} partial waves. The extracted residues $Re^{i\phi}$, defined in Eq.(114), for πN amplitude are compared with some of the previous works in Table VII. We see that the agreement in P_{33} and D_{13} are excellent. For P_{11} , there are significant differences between four analysis. As discussed in Ref.[27], it could be mainly due to the differences in the employed reaction models. On the other hand, the difference between the predicted P_{11} amplitudes at $E >$ about 1.6 GeV could be the reason why the third P_{11} pole is not found in Juelich analysis[68].

	EBAC-DCC		GWU-VPI[67]		Cutkosky[3]		Juelich[68]	
	R	ϕ	R	ϕ	R	ϕ	R	ϕ
$P_{33}(1210)$	52	-46	52	-47	53	-47	47	-37
$D_{13}(1521)$	38	7	38	-6	35	-12	32	-18
$P_{11}(1356)$	37	-111	38	-98	52	-100	48	-64
(1364)	64	-99	86	-46	-	-		
(1820)	20	-168	-	-	9	-167	-	-

TABLE VII: The extracted πN residues $Re^{i\phi}$ defined by Eq.(114).

B. Electromagnetic form factors

We extract the electromagnetic transition form factor of N^* in terms of the residue of resonance poles. This procedure is applied to $\Delta(1232)P_{33}$, $N^*(1520)D_{13}$ and $N^*(1440)P_{11}$ resonances. The resulting form factor is compared with the previous works and the analysis by CLAS. It is noted that helicity amplitudes defined at a real energy introduced in Section IV must be distinguished from the results in this section, which is extracted directly from the resonance pole with complex energy.

For the pion electromagnetic production helicity amplitudes, we replace the initial πN state as γN in Section III. Eq. (106) leads to the following expression of electromagnetic form factor,

$$\bar{\Gamma}_{\gamma^* N}^R = \sum_i \chi_i \bar{\Gamma}_{\gamma^* N, i}(q^0, M_R), \quad (186)$$

where

$$q_0 = \sqrt{\left(\frac{M_R^2 + Q^2 + m_N^2}{2M_R}\right)^2 - m_N^2}. \quad (187)$$

The electromagnetic N - N^* transition form factor is defined by matrix element of the electromagnetic currents between nucleon and N^*

$$A_{3/2}(Q^2) = X \langle N^*, s_z = 3/2 | -\vec{J}(Q^2) \cdot \vec{\epsilon}_{+1} | N, s_N = 1/2 \rangle, \quad (188)$$

$$A_{1/2}(Q^2) = X \langle N^*, s_z = 1/2 | -\vec{J}(Q^2) \cdot \vec{\epsilon}_{+1} | N, s_N = -1/2 \rangle, \quad (189)$$

$$S_{1/2}(Q^2) = X \langle N^*, s_z = 1/2 | J^0(Q^2) | N, s_N = 1/2 \rangle, \quad (190)$$

where $\vec{\epsilon}_{+1} = -(\hat{x} + i\hat{y})/\sqrt{2}$,

$$X = \sqrt{\frac{E_N(\vec{q})}{m_N}} \frac{1}{\sqrt{2K}},$$

with $K = (M_R^2 - m_N^2)/(2M_R)$. The above definition was originally introduced for the constituent quark model[66]. If $\langle N^* |$ is a resonance state, then the above expression at resonance position M_R must be evaluated by using Eq.(106). We thus have

$$A_{3/2}(Q^2) = XX' \sum_j \chi_j \bar{\Gamma}_{\gamma^* N, j}(Q^2, M_R, \lambda_\gamma = 1, \lambda_N = -1/2), \quad (191)$$

$$X' = \sqrt{\frac{(2j+1)(2\pi)^3(2q_0)}{4\pi}}. \quad (192)$$

Here the additional factor X' is due to our normalization of the vertex function $\bar{\Gamma}$. The above helicity amplitudes are in general complex number. $A_{1/2}$ and $S_{1/2}$ have similar expressions.

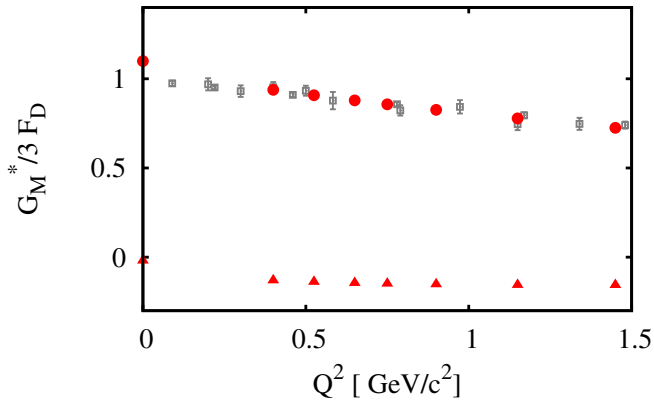
To extract helicity amplitudes using Eq.(191), we use the multipole amplitudes calculated from using the parameters determined in Ref.[31]. Our results at photon point are listed in Table VIII. We observe that the real parts of our results for P_{33} and D_{13} are in good agreement with several previous results[1, 69–71]. The large differences in P_{11} indicate that more investigations are needed to understand the differences between our resonance extraction method within a coupled-channel model and other methods which are mainly based on the Breit-Wigner parametrization of single channel K-matrix amplitudes.

For P_{33} we can use the standard relation[34] to evaluate the N - Δ magnetic transition form factor G_M^* in terms of helicity amplitudes. The real parts of our results are the solid

		EBAC	Arndt04/96	Ahrens04/02	Dugger07	Blanpied01
$P_{33}(1210)$	$A_{3/2}$	-269+12i	-258	-243		-267
	$A_{1/2}$	-132+38i	-137	-129		-136
$D_{13}(1521)$	$A_{3/2}$	125+22i	165 ± 5	147 ± 10	142 ± 2	
	$A_{1/2}$	-42+8i	-20 ± 73	-28 ± 3	-28 ± 2	
$P_{11}(1356)$ (1364)	$A_{1/2}$	-12+2i	-63 ± 5		-51 ± 2	
	$A_{1/2}$	-14+22i				

TABLE VIII: The extracted $\gamma N \rightarrow N^*$ helicity amplitudes are compared with previous results.

circles in Fig. 43, which are in good agreement with the previous analysis. In the same figure, we also show that the imaginary parts of our results are much weaker. This result and the results of Table VIII suggest that we can only make meaningful comparisons with the results from analysis based on the Breit-Wigner parametrization of single channel K-matrix amplitudes only for the cases that the imaginary parts are small. This turns out to be also the case of the $D_{13}(1521)$ resonance. In Fig. 44, we see that the real parts of our $A_{3/2}$ and $A_{1/2}$ are in good agreement with the results from CLAS collaboration[73]. The large differences in $S_{1/2}$ perhaps are mainly from the fact that the longitudinal parts of the amplitudes can not be well determined with the available data.

FIG. 43: The magnetic $N\Delta$ (1232) transition form factor $G_M^*(Q^2)$ defined in Ref.[34]. $G_D = 1. / (1 + Q^2 / b^2)^2$ with $b^2 = 0.71$ $(\text{GeV}/c)^2$. The solid circles (solid triangles) are the real (imaginary) parts of our results. The other data points are from previous analysis[72].

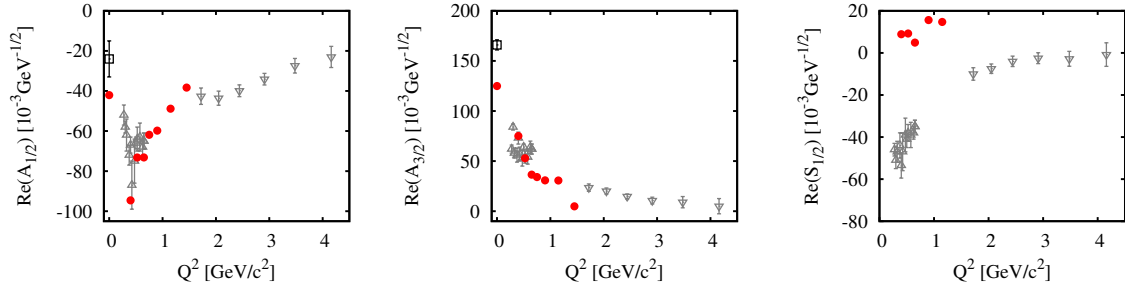


FIG. 44: The solid circles are the real parts of the extracted $\gamma N \rightarrow N^*(D_{13}(1520))$ form factors. The data are from CLAS collaboration[73]. transition form factors

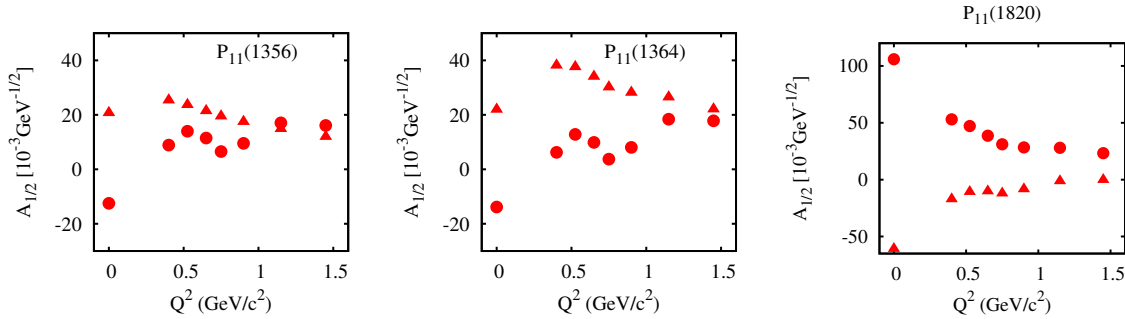


FIG. 45: The extracted $\gamma N \rightarrow N^*(1356), N^*(1364), N^*(1820)$ transition form factors of P_{11} . The solid circles (solid triangles) are their real (imaginary) parts.

For P_{11} , almost degenerate two poles are related to the resonance and the imaginary parts of the calculated helicity amplitudes for the three poles are very large. Thus it is not clear how to compare our results with previous results. We thus show both the real parts (solid circles) and imaginary parts (solid triangles) in Fig. 45. It seems that the structure of the pole at 1356 MeV and that of 1364 MeV are similar. In particular their real parts of $A_{1/2}$ change sign at low Q^2 , similar to what have been seen in the results from CLAS collaboration[73].

In this subsection, we have extracted the electromagnetic form factor from each pole associated with $N^*(1440)P_{11}$ respectively, but we should treat two poles at the same time because the both of them have influence with the physical sheet. We will investigate the double pole structure and try to develop the method for extracting the resonance parameter of Roper from these two poles in the next subsection.

C. Two pole approximation for P_{11} amplitude

It has been known that two poles are associated with $N^*(1440)P_{11}$ and we have shown the dynamical origin of the two poles is the single bare resonance in this section. The residues of those poles are extracted but it has not been known how to interpret the information of the two poles to understand the nature of the Roper resonance. Here we will present that we can successfully reproduce the πN elastic amplitude for P_{11} by applying two-channel Breit-Wigner formula described in Section II to two poles associated with $N^*(1440)$. At present this is a phenomenological attempt for the approximation, but this is an essential step toward extracting the transition form factor of Roper resonance and investigating the method for interpreting resonances which has two-pole structures.

When the resonance energy is close to the threshold energy of opening of a new channel, the convergence radius of Laurent expansion is limited. It is however when we take account of the threshold effects which appear in phase space integral we can extend the pole expansion of the scattering amplitude in a wider energy region. An example is two-channel Breit-Wigner form discussed in Section II,

$$F(E) = -\frac{R_1 p_1}{E - M + i\gamma_1 p_1 + i\gamma_2 p_2}, \quad (193)$$

where p_1 and p_2 are the on-shell momentum for the first and second channel. We have seen that two-channel Breit-Wigner formula can be naturally derived from the coupled channel equation.

When the resonance energy is close to the threshold of some channel, we may use an approximate form of the above formula, since only the closest threshold may play a significant role. We use the following formula with the channel momentum p of the newly opening channel,

$$F(E) = -\frac{R + \gamma' p}{E - (M^{res} + \gamma p)} + C + \dots \quad (194)$$

This parameterization generates two resonance poles in physical and unphysical sheet of the opening channel. In other words, a single resonance can have a pole in two Riemann sheet. The above parameterization will be extremely useful when both of the two resonance poles are close to the threshold. We write Laurent expansion of the resonance

poles as

$$F(E) = -\frac{R_i}{E - M_i^{res}} + c_i, \quad (195)$$

with $i = 1, 2$ for the poles at physical and unphysical sheets. In this case we can derive resonance parameters $R, M^{res}, \gamma, \gamma', C$ from the residue and resonance energy of Eq. (195) from each resonance pole. The parameters are given as

$$\gamma = \frac{M_1^{res} - M_2^{res}}{p_1 - p_2}, \quad (196)$$

$$M^{res} = M_1^{res} - \gamma p_1, \quad (197)$$

$$\gamma' = \frac{R_1(1 - \gamma dp_1/dE) - R_2(1 - \gamma dp_2/dE)}{p_1 - p_2}, \quad (198)$$

$$R = R_1(1 - \gamma dp_1/dE) - p_1\gamma', \quad (199)$$

$$C = \tilde{C}_1 - dp_1, \quad (200)$$

$$d = \frac{\tilde{C}_1 - \tilde{C}_2}{p_1 - p_2}, \quad (201)$$

$$\tilde{C}_i = C_i - \frac{dp_i/dE\gamma' + R_i\gamma d^2p_i/dE^2/2}{1 - \gamma dp_1/dE}. \quad (202)$$

The above formula can be derived assuming $C = c_a + c_bp$ and neglect c_b term since we have not included higher order of the energy dependence.

We applied the above formula for two poles of P_{11} obtained at Section III A. Fig. 46 shows the full amplitude of P_{11} by our model shown by red circles and green triangles agrees well with the approximated amplitude by Eq. (193) indicated by red and green lines, which means two-channel Breit-Wigner formula can well describe the amplitude with two-pole structure. If γ' in Eq. (193) is sufficiently small, we can regard R as the 'residue' of the Roper resonance and extract the transition form factor from it, but more discussions may be needed to declare what is the most appropriate method for understanding a resonance with multi-pole structure.

VI. SUMMARY

We have developed an analytic continuation method for extracting resonance parameters such as mass, width, electromagnetic transition form factors from a dynamical reaction model for $\pi N - \pi N$ and $\gamma^* N - \pi N$ amplitudes. This is the first application of

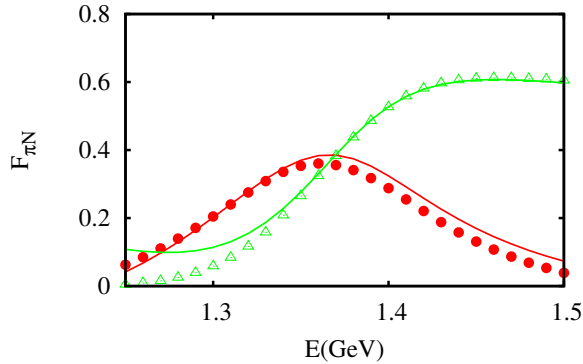


FIG. 46: πN elastic amplitude of P_{11} . The solid circles (solid triangles) are their real (imaginary) parts by the dynamical model. Red (green) line is the real (imaginary) part of approximated amplitudes by Eq. (193).

the analytic continuation method to a dynamical model which includes unstable particle channels σN , ρN and $\pi\Delta$ coupled with $\pi\pi N$.

We have also applied the analytic continuation method to the dynamical coupled channel model of meson production reactions developed in Ref.[28–31]. From the dynamical model, we have extracted pole positions of the all partial wave amplitudes and residues of P_{33} , D_{13} , and P_{11} partial waves. Except the $P_{33}(1600)$, P_{13} and P_{31} cases, pole positions of 3- and 4-star resonances listed by the PDG are consistent with our results. We have shown that two poles associated with $N^*(1440)P_{11}$, which are different in the Riemann sheet of $\pi\Delta$ channel, are originated in the single bare resonance dynamically and another pole at 1820 MeV on P_{11} has the same origin as the two poles. For residues associated with πN channel, we agree with most of the previous results[3, 26, 67, 68] for $P_{33}(1232)$, $D_{13}(1521)$ and two P_{11} poles near 1360 MeV. For residues associated with γ^*N channel, the corresponding helicity amplitudes for $P_{33}(1232)$ and $D_{13}(1521)$ are dominated by their real parts which are in good agreement with other analysis based on the Breit-Wigner parametrization of K-matrix amplitudes. We have successfully reproduced the πN elastic amplitude of P_{11} from two poles corresponding to the Roper resonance by using approximation with two-channel Breit-Wigner formula. With the progress made in this work, we can proceed to extract electromagnetic form factor of $P_{11}(1440)$ from two poles and that of all the other resonances.

Acknowledgments

I am sincerely grateful to Prof. Toru Sato, who is my academic supervisor, for plenty of useful discussions and warm encouragement throughout my research. I also would like to offer my deepest gratitude to Dr. Tung-Shung Harry Lee for many fruitful advices and discussions. I owe a very important debt to Prof. Akihiko Matsuyama, Dr. Bruno Julia-Diaz, Dr. Hiroyuki Kamano and Dr. Satoshi Nakamura for insightful discussions and collaboration. And I am deeply grateful to Prof. Masayuki Asakawa, Prof. Takashi Nakano, Prof. Atsushi Hosaka and Prof. Hiroyuki Noumi for constructive comments and suggestions. I wish to thank all members of the nuclear theory group of Osaka University for useful discussions and much help. Finally, I would like to express my sincere gratitude to my parents for their continuous encouragement and help.

APPENDIX A: NEWTON'S METHOD

We use Newton's method to obtain a pole position numerically as a zero point of the inverse of N^* propagator on the complex energy plane.

1. Function of single variable

Usual Newton's method for a function of single variable is

$$f(x_n) + f'(x_n)(x_{n+1} - x_n) = 0, \quad (\text{A1})$$

$$x_{n+1} = x_n - \frac{f(x_n)}{f'(x_n)}, \quad (\text{A2})$$

where $f(x_n)$ and x_n are real. Starting from x_1 close to a zero point of $f(x)$, we can expect $f(x_n) \simeq 0$ for sufficiently large n .

2. Function of multi variables

Supposing two real functions f_1 and f_2 and two real variables x and y , Newton's method for them is

$$\begin{pmatrix} f_1(x_n, y_n) \\ f_2(x_n, y_n) \end{pmatrix} + \begin{pmatrix} \frac{\partial}{\partial x} f_1(x_n, y_n) & \frac{\partial}{\partial y} f_1(x_n, y_n) \\ \frac{\partial}{\partial x} f_2(x_n, y_n) & \frac{\partial}{\partial y} f_2(x_n, y_n) \end{pmatrix} \begin{pmatrix} x_{n+1} - x_n \\ y_{n+1} - y_n \end{pmatrix} = \begin{pmatrix} 0 \\ 0 \end{pmatrix}, \quad (\text{A3})$$

or

$$\vec{f}(\vec{x}_n) + J(\vec{x}_n)(\vec{x}_{n+1} - \vec{x}_n) = \vec{0}, \quad (\text{A4})$$

where the matrix J is

$$J(\vec{x}_n) = \begin{pmatrix} \frac{\partial}{\partial x} f_1(x_n, y_n) & \frac{\partial}{\partial y} f_1(x_n, y_n) \\ \frac{\partial}{\partial x} f_2(x_n, y_n) & \frac{\partial}{\partial y} f_2(x_n, y_n) \end{pmatrix}. \quad (\text{A5})$$

\vec{x}_{n+1} is obtained by

$$\vec{x}_{n+1} = \vec{x}_n - J^{-1}(\vec{x}_n) \vec{f}(\vec{x}_n). \quad (\text{A6})$$

The both of $f_1(x_n, y_n)$ and $f_2(x_n, y_n)$ are expected to be zero for large n .

3. Complex function

If we write f_1 and f_2 by a complex analytic function $\tilde{f}(z)$ as

$$f_1(x_n, y_n) = \operatorname{Re}[\tilde{f}(x_n + iy_n)] = \operatorname{Re}[\tilde{f}(z_n)], \quad (\text{A7})$$

$$f_2(x_n, y_n) = \operatorname{Im}[\tilde{f}(x_n + iy_n)] = \operatorname{Im}[\tilde{f}(z_n)], \quad (\text{A8})$$

we can obtain the zero point of $\tilde{f}(z)$ in the same way as the case of real functions.

APPENDIX B: POLE EXPANSION WITH TWO RESONANCES

In this appendix, we present pole expansion of scattering amplitude with two resonances. Assuming there are two resonances coupling with the meson-baryon system, the propagator of resonant particles becomes a matrix,

$$t_{res} = \sum_{\alpha, \beta} \Gamma_{f, \alpha} \left(\frac{1}{D} \right)_{\alpha, \beta} \Gamma_{i, \beta}, \quad (\text{B1})$$

where

$$D_{\alpha, \beta} = (W - m_\alpha) \delta_{\alpha, \beta} - \Sigma_{\alpha, \beta}. \quad (\text{B2})$$

The explicit expression of $1/D$ for 2×2 matrix is

$$\frac{1}{D} = \frac{N}{\Delta}, \quad (\text{B3})$$

$$\Delta = D_{11}D_{22} - D_{12}D_{21}, \quad (\text{B4})$$

$$N = \begin{pmatrix} D_{22} & -D_{12} \\ -D_{21} & D_{11} \end{pmatrix}. \quad (\text{B5})$$

The resonance energy is obtained by

$$\Delta = D_{11}D_{22} - D_{12}D_{21} = 0. \quad (\text{B6})$$

The expansion of the t-matrix around resonance pole is given as

$$T(W) = \frac{R}{W - M} + C_0 + \dots, \quad (\text{B7})$$

and

$$R = \Gamma_f^T(M)N(M)\Gamma_i(M)/\Delta'(M), \quad (\text{B8})$$

$$C_0 = t^{non-res}(M) + \frac{\Gamma_f'^T(M)N(M)\Gamma_i(M) + \Gamma_f^T(M)N(M)\Gamma_i'(M)}{\Delta'(M)} - \frac{\Delta''(M)}{2(\Delta'(M))^2}\Gamma_f^T(M)N(M)\Gamma_i(M) + \frac{\Gamma_f^T N'(M)\Gamma_i(M)}{\Delta'(M)}. \quad (\text{B9})$$

Residues for $\pi N \rightarrow \pi N$ scattering ($R_{\pi\pi}$) and pion electroproduction $\gamma^* N \rightarrow \pi N$ ($R_{\gamma^*\pi}$) are written using πN and γN form factors (F_π, F_γ)

$$R_{\pi\pi} = F_\pi F_\pi, \quad (\text{B10})$$

$$R_{\gamma^*,\pi} = F_\pi F_{\gamma^*}. \quad (\text{B11})$$

In our model $D_{12} = D_{21}$, therefore $\Delta(M) = 0$ means

$$D_{11}(M)D_{22}(M) = D_{12}^2(M) = D_{21}^2(M). \quad (\text{B12})$$

Using this one can define form factor as

$$F_x = a\Gamma_{x,1} + b\Gamma_{x,2}, \quad (\text{B13})$$

$$a = \sqrt{\frac{D_{22}(M)}{\Delta'(M)}}, \quad (\text{B14})$$

$$b = -\frac{D_{12}(M)}{\sqrt{D_{22}(M)\Delta'(M)}}. \quad (\text{B15})$$

APPENDIX C: LAGRANGIANS

In this appendix, we specify a set of Lagrangians for deriving the non-resonant interactions $v_{MB,M'B'}$ which is the input to the coupled-channel equations Eq.(135). In the convention of Bjorken and Drell[65], the Lagrangian with π , η , N , and Δ fields are

$$L_{\pi NN} = -\frac{f_{\pi NN}}{m_\pi}\bar{\psi}_N\gamma_\mu\gamma_5\vec{\tau}\psi_N \cdot \partial^\mu\vec{\phi}_\pi, \quad (\text{C1})$$

$$L_{\pi N\Delta} = -\frac{f_{\pi N\Delta}}{m_\pi}\bar{\psi}_\Delta^\mu\vec{T}\psi_N \cdot \partial_\mu\vec{\phi}_\pi, \quad (\text{C2})$$

$$L_{\pi\Delta\Delta} = \frac{f_{\pi\Delta\Delta}}{m_\pi} \bar{\psi}_{\Delta\mu} \gamma^\nu \gamma_5 \vec{T}_\Delta \psi_\Delta^\mu \cdot \partial_\nu \vec{\phi}_\pi, \quad (\text{C3})$$

$$L_{\eta NN} = -\frac{f_{\eta NN}}{m_\eta} \bar{\psi}_N \gamma_\mu \gamma_5 \psi_N \partial^\mu \phi_\eta, \quad (\text{C4})$$

$$L_{\rho NN} = g_{\rho NN} \bar{\psi}_N [\gamma_\mu - \frac{\kappa_\rho}{2m_N} \sigma_{\mu\nu} \partial^\nu] \vec{\rho}^\mu \cdot \frac{\vec{\tau}}{2} \psi_N, \quad (\text{C5})$$

$$L_{\rho N\Delta} = -i \frac{f_{\rho N\Delta}}{m_\rho} \bar{\psi}_\Delta^\mu \gamma^\nu \gamma_5 \vec{T} \cdot [\partial_\mu \vec{\rho}_\nu - \partial_\nu \vec{\rho}_\mu] \psi_N + [\text{h.c.}], \quad (\text{C6})$$

$$L_{\rho\Delta\Delta} = g_{\rho\Delta\Delta} \bar{\psi}_{\Delta\alpha} [\gamma^\mu - \frac{\kappa_{\rho\Delta\Delta}}{2m_\Delta} \sigma^{\mu\nu} \partial_\nu] \vec{\rho}_\mu \cdot \vec{T}_\Delta \psi_\Delta^\alpha, \quad (\text{C7})$$

$$L_{\rho\pi\pi} = g_{\rho\pi\pi} [\vec{\phi}_\pi \times \partial_\mu \vec{\phi}_\pi] \cdot \vec{\rho}^\mu, \quad (\text{C8})$$

$$L_{NN\rho\pi} = \frac{f_{\pi NN}}{m_\pi} g_{\rho NN} \bar{\psi}_N \gamma_\mu \gamma_5 \vec{\tau} \psi_N \cdot \vec{\rho}^\mu \times \vec{\phi}_\pi, \quad (\text{C9})$$

$$L_{NN\rho\rho} = -\frac{\kappa_\rho g_{\rho NN}^2}{8m_N} \bar{\psi}_N \sigma^{\mu\nu} \vec{\tau} \psi_N \cdot \vec{\rho}_\mu \times \vec{\rho}_\nu, \quad (\text{C10})$$

$$L_{\omega NN} = g_{\omega NN} \bar{\psi}_N [\gamma_\mu - \frac{\kappa_\omega}{2m_N} \sigma_{\mu\nu} \partial^\nu] \omega^\mu \psi_N, \quad (\text{C11})$$

$$L_{\omega\pi\rho} = -\frac{g_{\omega\pi\rho}}{m_\omega} \epsilon_{\mu\alpha\lambda\nu} \partial^\alpha \vec{\rho}^\mu \partial^\lambda \vec{\phi}_\pi \omega^\nu, \quad (\text{C12})$$

$$L_{\sigma NN} = g_{\sigma NN} \bar{\psi}_N \psi_N \phi_\sigma, \quad (\text{C13})$$

$$L_{\sigma\pi\pi} = -\frac{g_{\sigma\pi\pi}}{2m_\pi} \partial^\mu \vec{\phi}_\pi \partial_\mu \vec{\phi}_\pi \phi_\sigma. \quad (\text{C14})$$

APPENDIX D: PARAMETERS FROM THE FITS

In this appendix, we show the parameters for the dynamical coupled channel model in section IV. They have been obtained by the fitting with the partial wave amplitudes

Parameter		SL Model
$f_{\pi NN}^2/(4\pi)$	0.08	0.08
$f_{\pi N\Delta}$	2.2061	2.0490
$f_{\eta NN}$	3.8892	—
$g_{\rho NN}$	8.7214	6.1994
κ_ρ	2.654	1.8250
$g_{\omega NN}$	8.0997	10.5
κ_ω	1.0200	0.0
$g_{\sigma NN}$	6.8147	—
$g_{\rho\pi\pi}$	4.	6.1994
$f_{\pi\Delta\Delta}$	1.0000	—
$f_{\rho N\Delta}$	7.516	—
$g_{\sigma\pi\pi}$	2.353	—
$g_{\omega\pi\rho}$	6.955	—
$g_{\rho\Delta\Delta}$	3.3016	—
$\kappa_{\rho\Delta\Delta}$	2.0000	—

TABLE IX: The parameters associated with the Lagrangians Eqs. (C1)-(C14). The results are from fitting the empirical πN partial-wave amplitudes [20] of a given total isospin $T = 1/2$ or $3/2$. The parameters from the SL model of Ref. [34] are also listed.

from VPI analysis and πN cross section. The parameters associated with the Lagrangians are listed in Table IX. Table X shows cut-off momentums of the meson-baryon-baryon vertices. The masses of the bare resonances are listed in Table XI. Coupling constants and cut-off momentums of the bare $N^* \rightarrow MB$ vertex functions are shown in Tables XII and XIII.

Parameter	(MeV)	SL model (MeV)
$\Lambda_{\pi NN}$	809.05	642.18
$\Lambda_{\pi N\Delta}$	829.17	648.18
$\Lambda_{\rho NN}$	1086.7	1229.1
$\Lambda_{\rho\pi\pi}$	1093.2	1229.1
$\Lambda_{\omega NN}$	1523.18	—
$\Lambda_{\eta NN}$	623.56	—
$\Lambda_{\sigma NN}$	781.16	—
$\Lambda_{\rho N\Delta}$	1200.0	—
$\Lambda_{\pi\Delta\Delta}$	600.00	—
$\Lambda_{\sigma\pi\pi}$	1200.0	—
$\Lambda_{\omega\pi\rho}$	600.00	—
$\Lambda_{\rho\Delta\Delta}$	600.00	—

TABLE X: Cut-offs of the form factors, Eq. (167), of the non-resonant interaction $v_{MB,M'B'}$. The results are from fitting the empirical πN partial-wave amplitudes [20] of a given total isospin $T = 1/2$ or $3/2$. The parameters from the SL model of Ref. [34] are also listed.

L_{TJ}	PDG's Mass(MeV)	M_1 (MeV)	M_2 (MeV)
S_{11}	1535; 1655	1800	1880
S_{31}	1630	1850	
P_{11}	1440; 1710	1763	2037
P_{13}	1720	1711	
P_{31}	1910	1900.3	
P_{33}	1232; 1600	1391	1602
D_{13}	1520; 1700	1899.1	1988
D_{15}	1675	1898	
D_{33}	1700	1976	
D_{35}	1960	—	
F_{15}	1685	2187	
F_{35}	1890	2162	
F_{37}	1930	2137.8	

TABLE XI: The masses of the nucleon excited states included in the fits (second and third columns). The first column contains the masses of the nucleon resonances given by PDG [24].

	πN	ηN	$\pi\Delta$		σN	ρN		
S_{11} (1)	7.0488	9.1000	−1.8526		−2.7945	2.0280	.02736	
S_{11} (2)	9.8244	.60000	.04470		1.1394	−9.5179	−3.0144	
S_{31}	5.275002	−	−6.17463		−	−4.2989	5.63817	
P_{11} (1)	3.91172	2.62103	−9.90545		−7.1617	−5.1570	3.45590	
P_{11} (2)	9.9978	3.6611	−6.9517		8.62949	−2.9550	−0.9448	
P_{13}	3.2702	−.99924	−9.9888	−5.0384	1.0147	−.00343	1.9999	−.08142
P_{31}	6.80277	−	2.11764		−	9.91459	0.15340	
P_{33} (1)	1.31883	−	2.03713	9.53769	−	−.3175	1.0358	0.76619
P_{33} (2)	1.3125	−	1.0783	1.52438	−	2.0118	−1.2490	0.37930
D_{13} (1)	.44527	−.0174	−1.9505	.97755	−.481855	1.1325	−.31396	.17900
D_{13} (2)	.46477	.35700	9.9191	3.8752	−5.4994	.28916	9.6284	−.14089
D_{15}	.31191	−.09594	4.7920	.01988	−.45517	−.17888	1.248	−.10105
D_{33}	.9446	−	3.9993	3.9965	−	.16237	3.948	−.85580
F_{15}	.06223	0.0000	1.0395	.00454	1.5269	−1.0353	1.6065	−.0258
F_{35}	.173934	−	−2.96090	−1.09339	−	−.07581	8.0339	−.06114
F_{37}	0.25378	−	−0.3156	−0.0226	−	.100	.100	.100

TABLE XII: The coupling constants $C_{N^*,JTLS;MB}$ of Eq. (168) with $MB = \pi N, \eta N, \pi\Delta, \sigma N, \rho N$ for each of the resonances. When there are more than one value for $\pi\Delta$ and ρN channels, they correspond to the possible quantum numbers (LS) listed in Table I.

	πN	ηN	$\pi\Delta$		σN	ρN		
S_{11} (1)	1676.4	598.97	554.04		801.03	1999.8	1893.6	
S_{11} (2)	533.48	500.02	1999.1		1849.5	796.83	500.00	
S_{31}	2000.00	—	500.00		—	500.031	500.00	
P_{11} (1)	1203.62	1654.85	729.0		1793.0	621.998	1698.90	
P_{11} (2)	646.86	897.84	501.26		1161.20	500.06	922.280	
P_{13}	1374.0	500.23	500.00	500.770	640.50	500.00	500.10	1645.2
P_{31}	828.765	—	1999.9		—	1998.8	2000.6	
P_{33} (1)	880.715	—	507.29	501.73	—	606.78	1043.4	528.37
P_{33} (2)	746.205	—	846.37	780.96	—	584.98	500.240	1369.7
D_{13} (1)	1658.	1918.2	976.36	1034.5	1315.8	599.79	1615.1	1499.50
D_{13} (2)	1094.0	678.41	1960.0	660.02	1317.0	550.14	597.57	1408.7
D_{15}	1584.7	1554.0	500.77	820.17	507.07	735.40	749.41	937.53
D_{33}	806.005	—	1359.38	608.090	—	1514.98	1998.99	956.61
F_{15}	1641.6	655.87	1899.5	522.68	500.93	500.76	500.0	1060.9
F_{35}	1035.28	—	1227.999	586.79	—	1514.3	593.84	1506.0
F_{37}	1049.04	—	1180.2	1031.81	—	600.02	600.00	600.02

TABLE XIII: The range parameter $\Lambda_{N^*,JTLS;MB}$ (in unit of (MeV/c)) of Eq. (168) with $MB = \pi N, \eta N, \pi\Delta, \sigma N, \rho N$ for each of the resonances. When there are more than one value for $\pi\Delta$ and ρN channels, they correspond to the possible quantum numbers (LS) listed in Table I.

	πN	ηN	$\pi\Delta$	σN	ρN
S11(1540)	400 - 220i	300 - 300i	300 - 220i	400 - 220i	400 - 220 i
S11(1642)	350 - 110i	350 - 110i	350 - 110i	350 - 110i	350 - 110 i
P11(1357)	300 - 100i	300 - 100i	100 - 200i	330 - 150i	330 - 150i
P11(1364)	300 - 120i	300 - 120i	200 - 150i	330 - 150i	330 - 150i
D13	350 - 110i	350 - 200i	350 - 110i	350 - 110i	350 - 110i
D15	300 - 120i	300 - 120i	300 - 150i	300 - 150i	300 - 150i
F15	300 - 120i	300 - 120i	300 - 150i	300 - 150i	300 - 150i
S31	300 - 120i	260 - 180i	300 - 150i	300 - 150i	300 - 150i
P33	200 - 100i	200 - 100i	200 - 100i	200 - 100i	200 - 100 i
D33	300 - 120i	300 - 180i	300 - 150i	300 - 150i	300 - 150i
F35(1738)	300 - 120i	300 - 180i	300 - 150i	300 - 150i	300 - 150 i
F35(1928)	300 - 150i	300 - 180i	300 - 150i	300 - 150i	300 - 150 i
F37	300 - 120i	300 - 180i	300 - 150i	300 - 150i	300 - 150i

TABLE XIV: Integral path on complex momentum plane for calculating on-shell πN scattering amplitude at the resonance pole.

APPENDIX E: INTEGRAL PATH

Tables XIV and XV shows the integral path of each channel, $\pi N, \eta N, \pi\Delta, \sigma N$ and ρN , for calculating πN scattering and electromagnetic form factor at the energy of the resonance pole, respectively. The paths are determined to choose the considered Riemann sheet and avoid singularities from the non-resonant potential. For example, in the case of calculating electromagnetic form factor, the path of $\pi\Delta$ momentum at the pole position on P_{33} partial wave is chosen as the straight line of $0 \rightarrow 200 - 100i \rightarrow 800 - 50i \rightarrow \infty - 50i$ MeV.

	πN	ηN	$\pi \Delta$	σN	ρN
P33	200 - 100i	200 - 100i	200 - 100i ; 800 -50i	200 - 100i	200 - 100i
P11(1357)	300 - 100i	300 - 100i	100 - 200i ; 800 -50i	330 - 150i	330 - 150i
P11(1364)	300 - 120i	300 - 120i	200 - 150i ; 800 -50i	330 - 150i	330 - 150i
D13	350 - 110i	350 - 200i	400 - 110i	350 - 110i	350 - 110i

TABLE XV: Integral path on complex momentum plane for calculating the electromagnetic form factor at the resonance pole.

[1] R. A. Arndt, W. J. Briscoe, I. I. Strakovsky, and R. L. Workman, Phys. Rev. C**66**, 055213 (2002); R. A. Arndt, I. I. Strakovsky, and R. L. Workman, Phys. Rev. C**53**, 430 (1996).

[2] T. Feuster and U. Mosel, Phys. Rev. C **58**, 457 (1998); Phys. Rev. C **59**, 460 (1999); V. Shklyar, H. Lenske, U. Mosel and G. Penner, Phys. Rev. C **71**, 055206 (2005).

[3] R. E. Cutkosky, C. P. Forsyth, R. E. Hendrick and R. L. Kelly, Phys. Rev. D**20**, 2839 (1979).

[4] D. M. Manley and E. M. Saleski, Phys. Rev. D **45**, 4002 (1992).

[5] V. Burkert and T.-S. H. Lee, Int. J. of Mod. Phys. **E13**, 1035 (2004).

[6] M. Kato, Ann. Phys. (N.Y.) **31**, 130 (1965).

[7] R. G. Newton, J. Math. Phys. **1**, 319 (1960).

[8] R. G. Newton, J. Math. Phys. **2**, 188 (1961).

[9] R. E. Peierls, Proc. Roy. Soc. Lond. A **253**, 16 (1959).

[10] K. J. Le Couteur, Proc. Roy. Soc. Lond. A **256**, 115 (1960).

[11] M. Goldberger and K. Watson, *Collision Theory* (Wiley, New York, 1964)

[12] Herman Feshbach, **Theoretical Nuclear Physics : Nuclear Reactions**, John Wiley & Sons, Inc (1992).

[13] G. Höhler and A. Schulte, πN Newsletter **7**, 94 (1992).

[14] G. Höhler, πN Newsletter **9**, 1 (1993).

[15] L. Eisenbud, Dissertation, Princeton, June 1948, unpublished.

[16] E. P. Wigner, Phys. Rev. **98**, 145 (1955).

[17] F. A. Berends, A. Donnachie, and D. L. Weaver, Nucl. Phys. **B4**, 1 (1967); 54; 103; A. Donnachie, in *High Energy Physics*, ed. E. Burhop, Vol. 5, p. 1 (Academic Press, New York, 1972)

[18] I. G. Aznauryan, Phys. Rev. C **67**, 015209 (2003); I. G. Aznauryan, Phys. Rev. C **68**, 065204 (2003).

[19] R. L. Walker, Phys. Rev. **182**, 1729 (1969).

[20] R. A. Arndt, I. I. Strakovsky, R. L. Workman, and M. M. Pavan, Phys. Rev. C **52**, 2120 (1995); R. A. Arndt, I. I. Strakovsky, R. L. Workman, Phys. Rev. C **53**, 430 (1996); R. A.

Arndt, I. I. Strakovskiy, R. L. Workman, *Int. J. Mod. Phys. A* **18**, 449 (2003).

[21] D. Drechsel, O. Hanstein, S. S. Kamalov, and L. Tiator, *Nucl. Phys. A* **645**, 145 (1999); S. S. Kamalov, S. N. Yang, D. Drechsel, O. Hanstein, and L. Tiator, *Phys. Rev. C* **64**, 032201(R) (2001).

[22] D. M. Manley, *Int. J. of Mod. Phys.*, **A18**, 441 (2003).

[23] M. Batinic, I. Slavus, and A. Svarc, *Phys. Rev. C* **51**, 2310 (1995); T. P. Vrana, S. A. Dytman, and T.-S. H. Lee, *Phys. Rep.* **328**, 181 (2000).

[24] C. Amsler *et al.* (Particle Data Group), *Phys. Lett. B* **667**, 1 (2008); <http://pdg.lbl.gov> .

[25] G. Höhler, *Eur. Phys. J. C* **3**, 624 (1998).

[26] R.A. Arndt, J. M. Ford, L. D. Roper, *Phys. Rev. D* **32**, 1085 (1985).

[27] R.E. Cutkosky and S. Wang, *Phys. Rev. D* **42**, 235 (1990).

[28] A. Matsuyama, T. Sato and T. -S. H. Lee, *Phys. Rept.* **439**, 193 (2007).

[29] B. Julia-Diaz, T. -S. H. Lee, A. Matsuyama, and T. Sato, *Phys. Rev. C* **76**, 065201 (2007).

[30] B. Julia-Diaz, T. -S. H. Lee, A. Matsuyama, T. Sato and L. C. Smith, *Phys. Rev. C* **77**, 045205 (2008).

[31] B. Julia-Diaz, H. Kamano, T. -S. H. Lee, A. Matsuyama, T. Sato and N. Suzuki, *Phys. Rev. C* **80**, 025207 (2009).

[32] I. R. Afnan and B. F. Gibson, *Phys. Rev. C* **47**, 1000 (1993).

[33] B. C. Pearce and I. R. Afnan, *Phys. Rev. C* **34**, 991 (1986); *C* **40**, 220 (1989).

[34] T. Sato and T.-S. H. Lee, *Phys. Rev. C* **54**, 2660 (1996).

[35] M. Kobayashi, T. Sato, and H. Ohtsubo, *Prog. Theor. Phys.* **98**, 927 (1997).

[36] R. G. Newton, **Scattering Theory of Waves and Particles**, Springer-Verlag, New York (1982).

[37] Y. Fujii and M. Kato, *Phys. Rev.* **188**, 2319 (1969).

[38] Y. Fujii and M. Fukugita, *Nucl. Phys. B* **85**, 179 (1975).

[39] R. J. Eden and J. R. Taylor, *Phys. Rev.* **133**, B1575 (1964).

[40] A. M. Badalyan, L. P. Kok, M. I. Polikarpov and Yu. A. Simonov, *Phys. Rept.* **82**, 31 (1982).

[41] Yu. V. Orlov, V. V. Turovtsev, *Sov. Phys. JETP* **59**, 902 (1989).

[42] B. C. Pearce and I. R. Afnan, *Phys. Rev. C* **30**, 2022 (1984).

- [43] B. C. Pearce and B. F. Gibson, Phys. Rev. C **40**, 902 (1989).
- [44] T. Sato and T.-S. H. Lee, J. Phys. G **36**, 073001 (2009).
- [45] T. Sato and T.-S. H. Lee, Phys. Rev. C **63**, 055201 (2001).
- [46] T.-S. H. Lee and A. Matsuyama, Phys. Rev. C **32**, 516 (1985).
- [47] R. Aaron, R. D. Amado, and J. E. Young, Phys. Rev. **174**, 2022 (1968).
- [48] J. A. Johnstone and T.-S. H. Lee, Phys. Rev. C **34**, 243 (1986).
- [49] *Modern Three-Hadron Physics*, editted by A.W. Thomas, Topics in Curren Physics (Springer-Verlag, 1977)
- [50] A. Matsuyama, Phys. Lett. B **152**, 42 (1984).
- [51] A. Matsuyama and T.-S. H. lee, Phys. Rev. C **34**, 1900 (1986).
- [52] O. Krehl, C. Hanhart, S. Krewald, and J. Speth, Phys. Rev. C **60**, 055206 (1999); C **62**, 025207 (2000).
- [53] K. Nakayama, Y. Oh, J. Haidenbauer, and T.-S. H. Lee, Phys. Lett. B **648**, 351 (2007)
- [54] CNS Data Analysis Center, GWU, <http://gwdac.phys.gwu.edu>.
- [55] H. Kamano, B. Julia-Diaz, T. -S. H. Lee, A. Matsuyama, and T. Sato, Phys. Rev. C **79**, 025206 (2009); H. Kamano, B. Julia-Diaz, T. -S. H. Lee, A. Matsuyama, and T. Sato, arXiv:0909.1129 [nucl-th].
- [56] K. Joo *et al.* (CLAS Collaboration), Phys. Rev. Lett. **88**, 122001 (2002).
- [57] B. Julia-Diaz, T.-S. H. Lee, T. Sato, and L. C. Smith, Phys. Rev. C **75**, 015205 (2007).
- [58] I. G. Aznauryan, V. D. Burkert and T.-S. H. Lee, arXiv:0810.0997v2 [nucl-th].
- [59] K. Joo *et al.* (CLAS Collaboration), Phys. Rev. C **68**, 032201 (2003).
- [60] H. Egiyan *et al.* (CLAS Collaboration), Phys. Rev. C **73**, 025204 (2006).
- [61] K. Joo *et al.* (CLAS Collaboration), Phys. Rev. C **72**, 058202 (2005).
- [62] J. Kelly *et al.* (Jefferson Laboratory E91011 and Hall A Collaborations), Phys. Rev. Lett. **95**, 102001 (2005).
- [63] CLAS Physics Database, JLab (Hall B), <http://clasweb.jlab.org/cgi-bin/clasdb/db.cgi> .
- [64] T. P. Vrana, S. A. Dytman, and T.-S. H. Lee, Phys. Rep. **328**, 181 (2000).
- [65] J. D. Bjorken and S. D. Drell, *Relativistic Quantum Field Theory*, McGraw-Hill, New York, (1964)
- [66] L. A. Copley, G. Karl, and E. Obryk Nucl. Phys. **B13**, 303 (1969).

- [67] R. A. Arndt, W. J. Briscoe, I. I. Strakovsky, and R. L. Workman, Phys. Rev C**74**, 045205 (2006).
- [68] Döring M, Hanhardt C, Huang F, Krewald S and Meißner U -G, Phys. Lett. **B681**, 26 (2009). Döring M, Hanhardt C, Huang F, Krewald S and Meißner U -G, Nucl. Phys. **A829**, 170 (2009).
- [69] J. Ahrens et al., Eur. Phys. J. A**21**, 323 (2004); J. Ahrens et al., Phys. Rev. Lett, **88**, 232002 (2002).
- [70] M. Dugger et al., Phys. Rev. C**76**, 025211 (2007).
- [71] G. Blanpied et al., Phys. Rev. C**64**, 025203 (2001).
- [72] W. Bartel et al., Phys. Lett **28B**, 148 (1968); K. Bätzner et al., Phys. Lett. **39B**, 575 (1972); J. C. Alder et al., Nucl. Phys. **B46**, 573 (1972); S. Sterin et al., Phys. Rev. D **12**, 1884 (1975).
- [73] G. Aznauryan, V. D. Burkert, et al. (CLAS Collaboration), Phys. Rev. C **80**, 055203 (2009); V. I. Mokeev, V. D. Burkert et al., Chinese Physics C **33**, 1210 (2009).
- [74] S. Prakhov et al., Phys. Rev. C **72**, 015203 (2005).
- [75] Robert M. Brown et al., Nucl. Phys. **B153**, 89 (1979).